Influence of Proteins and Building Direction on the Corrosion and Tribocorrosion of CoCrMo Fabricated by Laser Powder Bed Fusion

Masoud Atapour[a,b], Thalia E. Standish[c], Jeffrey D. Henderson[c], Zheng Wei[b], Vahid Dehnavi[c,d], Yolanda S. Hedberg[b,c]**

[a]Department of Materials Engineering, Isfahan University of Technology, Isfahan 84156-83111, Iran
[b]Department of Chemistry, The University of Western Ontario, London, Ontario, Canada N6A 5B7, Canada
[c]Surface Science Western, The University of Western Ontario, London, Ontario, N6G 0J3, Canada
[d]Department of Chemical & Biochemical Engineering, The University of Western Ontario, London, ON, N6A 5B9, Canada

Corresponding authors
Masoud Atapour: m.atapour@iut.ac.ir. ORCID 0000-0001-6333-0179
Yolanda S. Hedberg: yhedberg@uwo.ca. ORCID 0000-0003-2145-3650
Other authors
Thalia E. Standish: ORCID 0000-0001-6102-4135
Jeffrey D. Henderson: ORCID 0000-0001-7415-756X
Zheng Wei: ORCID 0000-0002-6042-9752
Vahid Dehnavi: ORCID 0000-0002-8429-002X

ABSTRACT

Cobalt-chromium-molybdenum (CoCrMo) alloys are common wear-exposed biomedical alloys and are manufactured in multiple ways, increasingly using additive manufacturing processes such as laser powder bed fusion (LPBF). Here, we investigate the effect of proteins and the manufacturing process (wrought vs. LPBF) and building orientation (LPBF-XY and XZ) on the corrosion, metal release, tribocorrosion, and surface oxide composition by means of electrochemical, mechanical, microscopic, diffractive, and spectroscopic methods. The study was conducted at pH 7.3 in 5 g/L NaCl and 5 mM 2-(N-morpholino) ethanesulfonic acid (MES) buffer, which was found necessary to avoid metal phosphate and metal-protein aggregate precipitation. The effect of 10 g/L bovine serum albumin (BSA) and 2.5 g/L fibrinogen (Fbn) was studied. BSA and Fbn strongly enhanced the release of Co, Cr, and Mo and slightly enhanced the corrosion (still in the passive domain) for all CoCrMo alloys, and most for LPBF-XZ, followed by LPBF-XY and the wrought CoCrMo. BSA and Fbn, most pronounced when combined, significantly decreased the coefficient of friction, due to lubrication, the wear track width and severity of the wear mechanism, and the tribocorrosion for all alloys, with no clear effect of the manufacturing type. The wear track area was significantly more oxidized than the area outside of the wear track. In the reference solution without proteins, a strong Mo oxidation in the wear track surface oxide was indicative of a pH decrease and cell separation of anodic and cathodic areas. This effect was absent in the presence of proteins.

Keywords: albumin, fibrinogen, friction, surface, microstructure, metal release

1. Introduction

The number of hip and knee replacements is estimated to continue increasing worldwide.[1-2] Cobalt chromium molybdenum (CoCrMo) alloys are widely used for orthopedic and dental implant materials due to an appropriate balance between mechanical strength, wear and corrosion resistance, and biocompatibility.[3]

Traditional processes for manufacturing CoCrMo implants include casting, hot forging, and subtractive processes, which are associated with various drawbacks, such as solidification defects, high cost, and limited flexibility in the personalization of the implants. Additive manufacturing (AM) has grown noticeably in importance for producing highly customizable implants.[4] Over the past few decades, laser powder bed fusion (LPBF), also referred to as selective laser melting (SLM), has been one of the dominant AM methods for implant materials.[4] It is well known that the manufacturing method can be a decisive factor affecting the corrosion and tribocorrosion of CoCrMo alloys because it affects the microstructure, defects, and surface properties important for the corrosion and wear mechanisms.[5-6] In recent years, electron beam melting (EBM) has also gained prominence in producing orthopedic implants. EBM generates parts with no residual stress, thanks to the hot process and a controlled vacuum environment.[7] Its cost-effectiveness and ability to process reactive materials make it ideal for biomedical applications, including orthopedics and maxillofacial surgery.[7] However, this paper will focus on the more common LPBF process.

In sliding parts, such as the components of artificial joints and dental implants, corrosion and wear processes are the main concerns and are associated with the release of metal ions, species, and particles (short: metal release).[8-9] Metal release into tissues that surround implants can be associated with adverse effects such as osteolysis, reduced bone mineralization, metallosis, inflammation involving macrophages, aseptic lymphocytic vasculitis-associated lesions (ALVAL), granuloma, pseudotumours, and aseptic loosening.[6, 10-13] Also, as low as 0.4 µg/L of Co in the blood of patients can cause measurable neurologic toxicity[14] and the metal release from CoCrMo can cause metal allergic reactions,[15] increased periprosthetic infection risks,[16-18] and even trigger or deteriorate autoimmune conditions[19] such as fibromyalgia, inflammatory arthritis, systemic lupus erythematosus (SLE), and Sjögren's syndrome.

There is no consensus on whether the corrosion and tribocorrosion resistance of CoCrMo alloys produced by LPBF and EBM, or AM in general, is greater or smaller than that of traditionally manufactured CoCrMo in relevant physiological conditions or in-vivo. This depends on the specific system and manufacturing methods/parameters. Two studies in various simulated physiological conditions found no corrosion differences between LPBF CoCrMo and wrought or cast counterparts (low carbon and unknown carbon content).[20-21] Our previous study comparing LPBF CoCrMo with a high carbon cast CoCrMo showed improved corrosion resistance of the LPBF CoCrMo, due to fewer Cr-rich carbide precipitates at grain boundaries.[22]

Recent biocorrosion assessments of CrCrMo samples fabricated by laser-directed energy deposition in simulated body fluid revealed a spatially non-uniform and differential corrosion mechanism.[23] The corrosion evaluations of lattice-type (controlled porosity) CoCrMo (0.35 wt.% C) specimens for bone ingrowth fabricated with LPBF showed a relatively high corrosion resistance in simulated body fluid.[24] In a recent study,[25] the influence of scan speed on the corrosion and tribocorrosion properties of LPBF CoCrMoW samples was examined, showing that the laser scan speed could directly affect the microstructure and subsequently impact the corrosion and tribocorrosion behavior of the samples. The surface of as-printed LPBF CoCrMo is very different from abraded/polished surfaces of either LPBF or traditionally manufactured CoCrMo and has been shown to influence corrosion and biocompatibility.[26-27] LPBF CoCrMo fabricated in different building orientations (perpendicular and parallel to building direction) may or may not exhibit different corrosion behaviors, depending on the carbon content, heat treatment, and environmental conditions.[26-27] Our previous study suggested that a suitable biomedical manufacturing protocol, including low-carbon CoCrMo feed powder and a suitable heat treatment protocol, can eliminate any differences in building orientations.[26]

The manufacturing process and microstructure are, hence, critical to the corrosion resistance of CoCrMo in simulated physiological conditions. In addition, they also play a major role in tribological processes and are therefore essential to the tribocorrosion (the combined effect of corrosion and wear) of CoCrMo alloys,[28-29] which are used in wear-exposed components. The tribocorrosion of CoCrMo also strongly depends on the physiological environment; for example, it has been reported that its corrosion rate strongly varies in different patients' synovial fluids.[30] Some of the chemical components of interest are salt (NaCl), complexing agents and proteins, pH, and oxidative potential (related to inflammation).[27, 31-39] Proteins have been widely reported to act as lubricants in a tribocorrosion situation and to hence reduce the rate of wear. Still, they can also increase the chemical degradation rates affecting corrosion and tribocorrosion.[28, 38-40] They also seem to play an important role in the formation of so-called tribolayers, which can reduce the coefficient of friction.[41-42] Proteins are very variable and may influence the tribocorrosion behavior of CoCrMo alloys in multiple ways and as a function of microstructure. Recent review papers on additively manufactured biomaterials have underscored the necessity for comprehensive research efforts to address critical questions in this field.[43-45] To the best of our knowledge, there have not been any systematic studies on the tribocorrosion behavior of CoCrMo as a function of manufacturing and protein type.

This study investigates the tribocorrosion behavior of LPBF fabricated in two different building orientations and a traditionally manufactured (wrought) CoCrMo in simulated physiological conditions in the presence of serum albumin or fibrinogen. By using a multi-analytical and thorough experimental approach, we aim to give an answer on the individual chemical and mechanical impact of serum albumin and fibrinogen on the degradation behavior of these three CoCrMo alloys.

2. Materials and methods

2.1. CoCrMo

LPBF CoCrMo fabricated perpendicular (XY) and parallel (XZ) to the building direction, Fig. 1a, were described previously.[26] In short, inert gas-atomized, spherical (15–45 µm) CoCrMo powder was used as feed powder (chemical composition in Table 1) for the fully dense specimens fabricated by a Renishaw AM400 Selective Laser Melting System with a discontinuous laser (40–50 µs exposure time, 60–70 µm point distance). The processing parameters are depicted in Table 2, and the heat treatment process involved gradually heating the coupons to 450 °C over a period of 60 minutes, holding them at this temperature for 45 minutes, reheating to 750 °C over 45 minutes, holding them at this temperature for 60 minutes, and then cooling them to room temperature in a furnace.

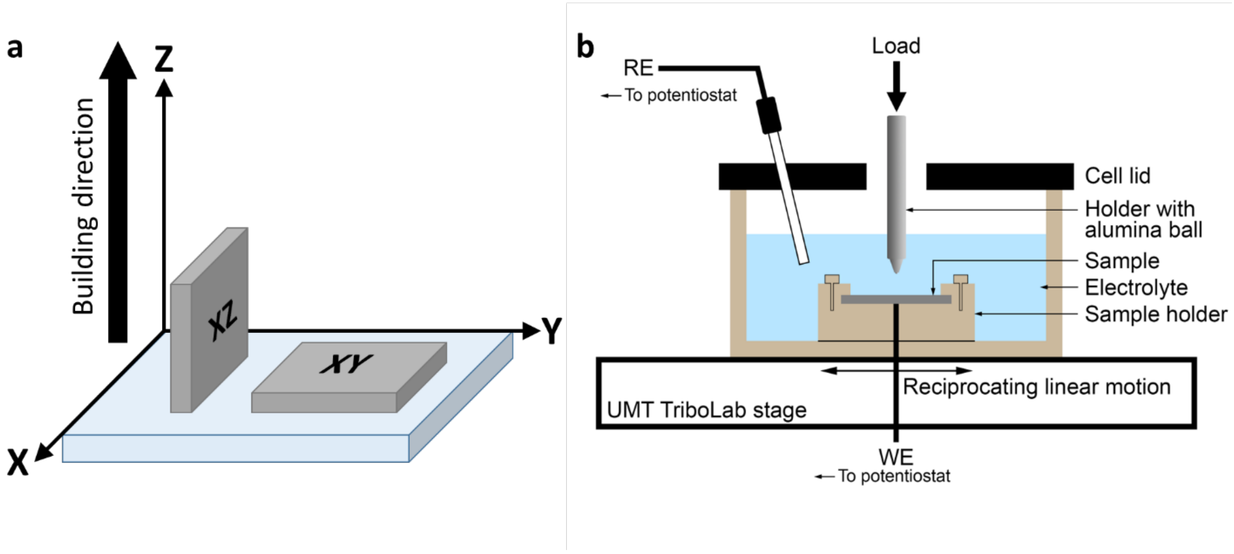

Figure 1. a) Schematic illustration of the building direction and orientation of LPBF CoCrMo alloy coupons (LPBF-XZ and LPBF-XY) sized 15×15×2 mm. b) Schematic illustration of tribocorrosion set-up. RE – Reference electrode; WE – Working electrode; UMT – Universal Micro Tribometer.

Table 1. Chemical composition of the biomedical Co28Cr6Mo low carbon alloy powder, as per supplier information. Bal. – balance (remainder to 100%).

Element	Cr	Mo	Mn	Si	N	Fe	Ni	C	W	Co
wt%	28.0	6.10	0.77	0.57	0.22	0.20	0.05	0.02	0.02	Bal.

Table 2. LPBF parameters.

Power	Spot size	Scan speed	Layer thickness	Scan spacing	Layer rotation angle
200 W	70 µm	2 m/s	40 µm	70 µm	67°

For comparison, a traditionally manufactured CoCrMo alloy was also investigated, consisting of biomedical grade cobalt-chromium (28 wt%)-molybdenum (6 wt%) (CoCrMo) alloy disks, conforming to ASTM F1537 Alloy 1, of 22 mm in diameter and 2 mm in thickness (a total surface area of 9.0 cm^2), supplied by Ionbond, Switzerland, and certified by Aubert & Duval, France. They were produced by vacuum induction melting followed by electroslag remelting and warm working, and were investigated previously.[46] These specimens are referred to as 'wrought' in the following.

2.2. Microstructure characterization

Optical microscopy (OM, Keyence VHX-6000 Digital Microscope) and scanning electron microscopy (SEM, Philips XL 30) techniques were utilized for surface and microstructure characterization. X-ray diffraction (XRD) analysis was performed to identify the phases using a Rigaku SmartLab X-ray diffraction system with CuKα radiation in Bragg-Brentano geometry mode. Diffraction data were acquired over a 2θ range from 35° to 100° with a step width of 0.02° and a scan speed of 3°/min. The ICDD PDF-4+ 2023 inorganic database was used to search for phase identification. For microstructure characterization, the specimens were polished with 0.25 µm diamond paste and then electropolished for 20 s at 4 V using a 1:9 (by volume) solution of HCl and H_2O.

2.3 Choice of solution components

This study investigates the effect of two relevant proteins for implant surfaces; serum albumin and fibrinogen. Bovine serum albumin (BSA) is a globular protein, which is net negatively charged at pH 7.3, with an approximate molecular weight of 66,000 g/mol. The concentration of serum albumin in the blood plasma is in the range of 40-60 g/L,[47] while it is about 12 g/L in synovial fluid.[48] This study used 10 g/L BSA due to experimental challenges with protein aggregation at higher concentrations[46] and because it is a relevant concentration that is still far higher than what would be required for a complete adsorption of BSA on metal surfaces. [49] Fibrinogen (Fbn) was chosen because of its larger size, 340,000 g/mol. Its typical human blood plasma concentration is 2-4 g/L.[50] It is also net negatively charged at pH 7.3,[51] and it is important for implant biocompatibility.[52] Its concentration in this study is 2.5 g/L. Since the adsorption of proteins is strongly dependent on ionic strength and pH,[53] it was necessary to use a relevant (0.15 M, pH 7.2-7.4) buffer. However, previous research showed that Co and Cr strongly bind to phosphates, jeopardizing the interpretation of experimental results in phosphate-buffered saline solutions.[46, 54] Therefore, this study employed a sodium chloride (NaCl) and 2-(N-morpholino)ethanesulfonic acid (MES) buffer. MES buffer was found to be least likely among various buffers to bind to copper ions in a previous study.[55]

2.4. Corrosion studies without friction

Prior to the corrosion experiments, the surfaces were polished from P180 up to P1200 SiC, then sonicated in acetone and ethanol, each for 5 min, rinsed with ultrapure water (18.2 MΩ·cm resistivity), and dried with nitrogen gas (room temperature). They were then stored for 24 h in a desiccator (relative humidity <10%) prior to the experiment, to allow a reproducible oxide growth among the specimens for the various testing conditions.

The corrosion behavior of the wrought and LPBF specimens was assessed using open circuit potential (OCP), cyclic potentiodynamic polarization (CPP), and electrochemical impedance spectroscopy (EIS) measurements in 5 g/L NaCl, 5 mM MES, 10 g/L BSA (Sigma Aldrich A7906), and 2.5 g/L Fbn (fibrinogen from bovine plasma, Sigma Aldrich F8630). The solution pH was adjusted to 7.3 ± 0.1 with NaOH. This solution is denoted NaCl+MES+BSA+Fbn. For comparison, all the corrosion assessments were also conducted in a NaCl+MES solution (5 g/L NaCl, 5 mM MES, pH 7.3).

The experiments were conducted using a ModuLab XM ECS Solartron potentiostat/galvanostat, an Ag/AgCl in saturated KCl reference electrode, a counter electrode consisting of a platinum sheet, and the specimen as the working electrode. Before each test, the specimens were immersed for 60 min while measuring the OCP to reach a steady state condition. CPP was carried out with a scan rate of 1 mV/s scanning from −0.25 V vs. OCP to 1 V vs. Ag/AgCl sat. KCl or when the current reached 0.1 mA/cm^2, followed by a reverse scan back to the measured corrosion potential. EIS was conducted at OCP with an alternating current amplitude of 10 mV$_{rms}$ and a frequency range from 10,000 Hz to 0.01 Hz. The EIS results were fitted using Zview software.

2.5. Tribocorrosion studies

For tribocorrosion evaluations, all the tested surfaces (LPBF-XY, LPBF-XZ, wrought CoCrMo) were ground to P1200 SiC (with water) followed by ultrasonic cleaning in acetone and ethanol, each for 5 min, and drying with nitrogen gas at room temperature. They were then stored for 24 h in a desiccator (relative humidity <10%) prior to the experiment. A ball-on-plate reciprocating (linear) sliding configuration was used based on the ASTM G133 standard. Inert 5 mm diameter Al_2O_3 balls were used as the counter-body. The tribocorrosion tests were carried out in a two-electrode tribocorrosion cell on a Universal Micro Tribometer (UMT) TriboLab (Bruker) integrated with a ModuLab XM ECS Solartron Analytical potentiostat. The setup is illustrated in

Figure 1b. The reference electrode was Ag/AgCl sat. KCl, and the CoCrMo coupons/disks (LPBF-XY, LPBF-XZ, wrought) were acting as the working electrode. An applied normal load of 3 N was selected. The reciprocating stroke length was 1.5 mm, and the sliding speed was 1 mm/s. CoCrMo specimens were mounted into the tribocorrosion cell and slid against the Al_2O_3 ball in three different solutions: 5 g/L NaCl and 5 mM MES (denoted NaCl+MES), 5 g/L NaCl, 5 mM MES, and 10 g/L BSA (denoted NaCl+MES+BSA), and 5 g/L NaCl, 5 mM MES, 10 g/L BSA, and 2.5 g/L Fbn (denoted NaCl+MES+BSA+Fbn). All the experiments were conducted at 37 °C. The solution-exposed surface area of the specimens was 1.5 cm^2 in all cases.

These tests were conducted in three steps. The first step was in static conditions (no friction) for 60 min to ensure steady-state conditions and measure the OCP. Next, there was the sliding process with a normal load of 3 N for 60 min. Finally, the load was removed and the OCP value of the specimen was continuously recorded for 30 min after the sliding process. The coefficient of friction (COF) and OCP values were automatically recorded throughout the test, and each group of samples was tested at least three times to investigate the reproducibility of the tests.

All presented potentials are against the Ag/AgCl sat. KCl reference electrode. COF data was compressed, and the COF data was processed by an oscillating function using 50% in the middle of each motion by the Viewer software (UMT, Bruker).

2.6. Post-tribocorrosion surface analysis

After tribocorrosion experiments, all the tested surfaces were investigated using scanning electron microscopy coupled with energy-dispersive X-ray spectroscopy (SEM/EDS, Hitachi SU3900 Large Chamber Variable Pressure SEM).

Further, X-ray photoelectron spectroscopy (XPS), which can probe the chemical composition of the outermost surface (7–10 nm) with detection limits of 0.1-0.5 atomic percent, was employed as follows. One coupon/disk for each condition was analyzed within and outside the wear track. A tribocorrosion specimen exposed to air (no solution), was also run for comparison. The XPS analyses were carried out with a Kratos AXIS Supra X-ray photoelectron spectrometer using a monochromatic Al K_α source (15 mA, 15 kV). The instrument work function was calibrated to give a binding energy (BE) of 83.96 eV for the Au $4f_{7/2}$ line for metallic gold and the spectrometer dispersion was adjusted to give a BE of 932.62 eV for the Cu $2p_{3/2}$ line of metallic copper. The Kratos charge neutralizer system was used on all specimens. All specimens were electrically isolated from the instrument sample holder for these analyses. For measurements outside the wear track, survey scans were carried out with an analysis area of 300 × 700 μm and a pass energy of 160 eV and high-resolution analyses were carried out with an analysis area of 300 × 700 μm and a pass energy of 20 eV. For measurements inside the wear track (in the middle of it), a smaller spot size of 110 μm was used. High-resolution spectra for C 1s, O 1s, N 1s, Co 2p, Cr 2p, and Mo 3d were collected. High-resolution spectra were charge-corrected according to the main line of adventitious carbon (284.8 eV).[56] The C 1s high-resolution peak was fitted by four peaks, denoted C1–C4: 284.8 eV attributed to the C-C and C-H bonds (C1), a peak at 286.3 eV (denoted C2) assigned to peptidic residues, C-O, and C-N bonds, a peak at 287.8 eV (denoted C3) assigned to N-C=O and C=O bonds, and a peak at 288.8 eV (denoted C4) assigned to O-C=O bonds. Since C2–C4 are more likely to originate from adsorbed proteins than from adventitious carbon, they were used for the evaluation. The N 1s peak at 400 eV was attributed to organic nitrogen and was used for the evaluation. For the three metal peaks, they were deconvoluted into their metallic and oxide components according to reference data.[57-59] All spectra with their fitted components, including any information on peak overlaps, are presented in the supplementary information.

2.7. Metal release measurements under static conditions

All containers/materials in contact with solutions were acid-cleaned in 10% HNO_3 for at least 24 h, followed by four rinses with ultrapure water (18.2 MΩ cm resistivity).

The aqueous concentrations of Co, Cr, and Mo were measured from LPBF-XY, LPBF-XZ, and wrought coupons ground with P1200 SiC paper (as prepared for the corrosion and tribocorrosion tests) and exposed to two different solutions: 5 g/L NaCl and 5 mM MES (denoted NaCl+MES) and 5 g/L NaCl, 5 mM MES, 10 g/L BSA, and 2.5 g/L Fbn (denoted NaCl+MES+BSA+Fbn) after 24 h immersion at 37 °C in an acid-cleaned double-layer water bath electrochemical cell. One blank sample, without test coupons, and triplicate samples were exposed for each solution and specimen type. After the exposure, the CoCrMo specimen and solution were separated. The specimens were rinsed with 1 mL of ultrapure water, and this solution was added to the solution sample. Solution samples were stored in the freezer (−20 °C) prior to digestion and trace metal solution analysis.

For solution sample digestion, 3 mL of solution samples and 0.333 mL 67% ultrapure nitric acid were pipetted into an acid-cleaned PTFE decomposition vessel. The vessels were capped and digested following EPA method 3052 (microwave-assisted acid digestion of siliceous and organically based matrices) by using an ETHOS UP Microwave Digestion System. After microwave digestion, solution samples were transferred into a 15 mL acid-cleaned flask and refilled to 12 mL.

Inductively coupled plasma mass spectrometry, ICP-MS (ICAP Q, Thermo Scientific, Canada) was used to measure the released amounts of metals into the solution. The levels of ^{59}Co, ^{52}Cr and ^{95}Mo (µg/L) were quantified as the average of triplicate readings in each sample in KED mode (kinetic energy discrimination) using argon as vector gas and helium as collision gas. For the calibration, a multi-element standard solution was made in the digested solution (blank) as a matrix; 0, 10, 30, 60 and 100 µg/L for Co, Cr, and Mo. The limits of detection (in both solutions) were: Co: 0.37 µg/L, Cr: 0.25 µg/L, Mo: 0.02 µg/L. The corresponding blank concentrations (c_{blank}), if detectable, were subtracted from the triplicate average of sample concentrations (c_i). Released amounts of metals (µg/cm^2) were calculated by multiplying the blank and dilution factor (DF)-corrected concentration (µg/L) by the exposure volume, V (0.02 L), divided by the exposed coupon area, A (0.5—3.5 cm^2, depending on specimen), as shown in Eq. (1). The number of replicates (n) was 3. The DF is a unitless factor determined from the final volume after digestion divided by the initial sample volume; for example, it is 5 if 1 mL of solution sample is diluted with 4 mL of acid or water.

$$\text{Released amount} = \frac{(c_{\mathrm{i}} - c_{\mathrm{blank}}) \times \mathrm{DF} \times V}{A} \quad (1)$$

2.8. Microhardness measurements

The samples (LPBF-XY, LPBF-XZ, and wrought CoCrMo) were polished with a 1 µm diamond slurry. Microhardness measurements were performed on the polished samples using a LECO LM-100 microhardness tester with a Vicker's indenter using an applied load of 500 gf and a dwell time of 15 seconds. Seven areas were measured for each sample.

2.9 Statistical analyses

A student's t-test with unpaired data and unequal variance (KaleidaGraph v. 4.0) was used to determine any statistically significant differences between two sets of data of independent specimens. When the probability P that the data sets are equal was less than 0.05, the difference was considered statistically significant.

3. Results and Discussion

3.1. Microstructural evaluations

Figure 2 shows optical micrographs (OM) of the as-built LPBF CoCrMo specimens with the plane perpendicular (XY) (a) and parallel (XZ) (b and c) to the building direction. Similar to previous work,[60-61] columnar grain morphology with an average grain size of 40 µm can be seen for LPBF-XY. As expected, a network of overlapping melt pools was formed on the LPBF-XZ surface of as-built samples, Figure 2 (b, c). Columnar grains and cellular structures were observed, as in our previous study[26] and other studies[62-63]. The wrought CoCrMo, in Figure 2d, consisted of a cobalt-rich matrix (alpha phase) and large grains. No blocky carbides were visible for any of the specimens, as they were dissolved after the heat treatment.[26]

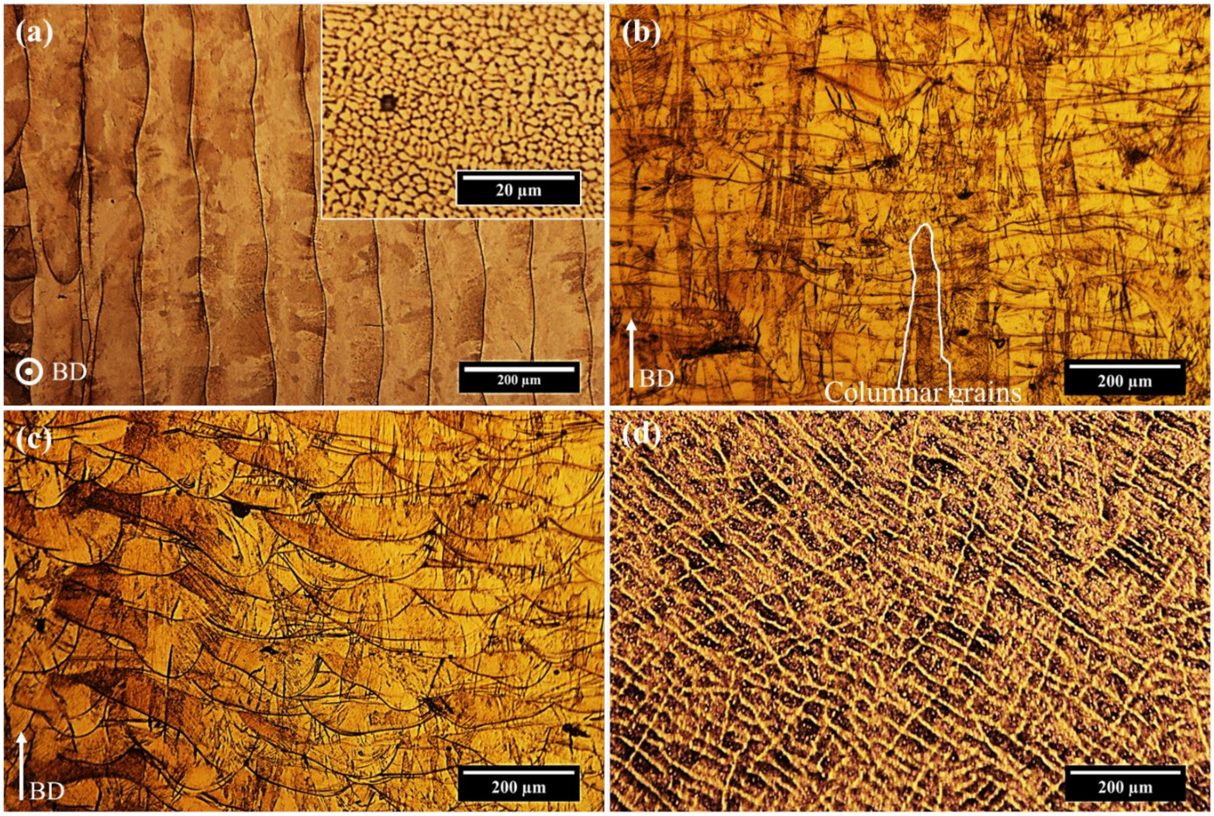

Figure 2. Optical images of the metallographic structure of the polished and etched CoCrMo alloys: (a) SLM-XY, (b and c) SLM-XZ, and (d) wrought.

In this study, microhardness values were obtained for all the samples to investigate the impact of hardness on tribocorrosion aspects. Average microhardness values of 447 ± 7.7, 444 ± 18 and 475 ± 10 $HV_{0.5}$ were recorded for LPBF-XY, LPBF-XZ and wrought CoCrMo samples, respectively. The wrought CoCrMo (microstructure in Figure 2d), was the hardest (statistically significant, $P<0.01$, compared with both LPBF-XY and LPBF-XZ). This might be related to its thermomechanical treatment.[64] The variability in microhardness among different areas was largest for the LPBF-XZ CoCrMo, as it had a rather heterogeneous microstructure (Figures 2b and c, strongly oriented columnar grain growth).[65-66]

X-ray diffraction patterns for LPBF-XY, LPBF-XZ, and wrought CoCrMo are presented in Figure 3. The XRD patterns show the samples mainly consisted of γ-phase with a face-centered cubic (FCC) structure and ε-phase with a hexagonal close-packed (HCP) structure. These results are consistent with previous XRD analyses of LPBF-XY and LPBF-XZ CoCrMo.[26, 65] Based on the reference XRD pattern, ICDD 01-087-9231, the main three peaks for the γ-phase are γ(111), γ(200), and γ(220) located at 2θ values of 43.78°, 51.00°, and 75.02° with intensities of 1000, 436, and 192, respectively. Inspection of the XRD patterns reveals a difference in the texture in the γ-phase for the three samples. The relative intensities of the γ-phase's three main peaks for wrought and LPBF-XZ are more consistent with the reference pattern than those of LPBF-XY, for which the γ (220) is more intense than γ (111), suggesting a stronger (220) texture in LBPF-XY. This is in agreement with previous work.[22] While the LPBF-XY sample seems to show less ε-phase than the LPBF-XZ and wrought samples, no conclusion can be drawn about this because of different textures. It has been demonstrated that the γ-phase is not thermodynamically stable and can be transformed into the ε-phase during cooling.[67] During the LPBF additive manufacturing process, the XZ plane is (re-)heated more than the XY plane.[68] The XY plane, being more rapidly cooled, therefore, may show less ε-phase, while the XZ plane is more similar to the wrought CoCrMo. This behaviour is more pronounced on the surface; a previous study on polished and unpolished LPBF-XY samples showed no ε-phase for the unpolished (and more rapidly cooled) surface than the polished surface underneath.[22]

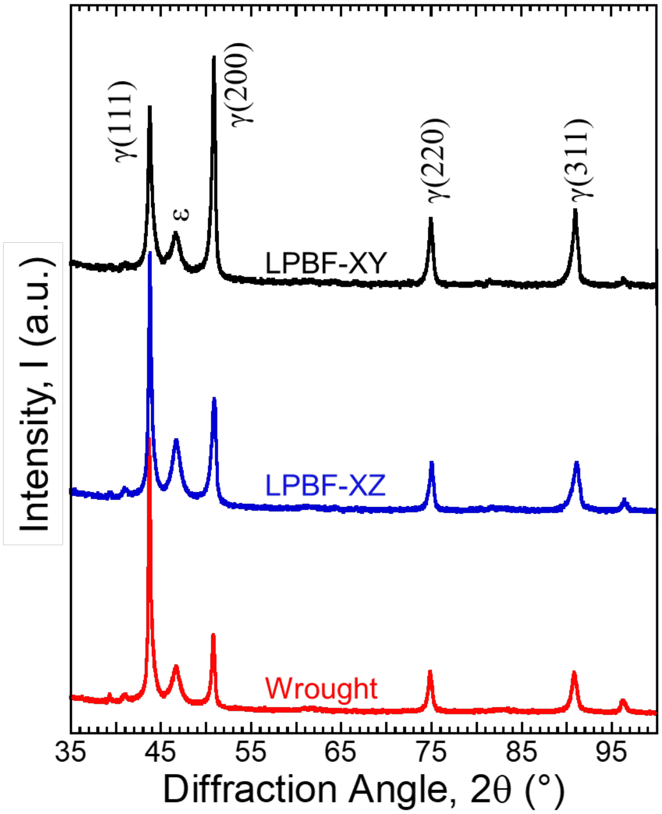

Figure 3. X-ray diffraction patterns for LPBF-XY, LPBF-XZ, and wrought CoCrMo.

3.2. Corrosion without friction

Before changing the potential, the OCP was recorded for 1 h, Figure S1 (supplementary information). The OCP was smoothly increasing with time for all specimens, suggesting an adjustment of the surface oxide (passivation) and no localized corrosion. The final OCP values were similar among the specimens and solutions, with no statistically significant differences; -0.27 ± 0.02 V in NaCl+MES, -0.28 ± 0.006 V in NaCl+MES+BSA, and -0.32 ± 0.022 V in NaCl+MES+BSA+Fbn. Based on the corrosion data extracted from CPP results (Table 3), it can be deduced that there is a slightly lower corrosion potential of the CPP, E_{corr}, in the protein-containing than protein-free solution, and no significant difference for other corrosion parameters (slopes of cathodic and anodic branches, β_a and β_c, corrosion and passive current densities, i_{corr} and i_{pass}), Figure 4 and Table 3.

Among the specimens, the corrosion and passive current densities of LPBF-XZ were consistently higher than those for the wrought and LPBF-XY specimens. It also showed a more positive E_{corr}, a less steep anodic branch as seen by a lower β_a value, and a steeper cathodic branch, with a higher β_c value. This indicates quicker oxide buildup compared with the other specimens, which is also confirmed by a steeper OCP increase with time, Fig. S1.

The shape of the CPP curves further indicates no localized corrosion, as indicated by a negative hysteresis during the reverse scan. Also, there was no considerable difference between the sample surface before and after the CPP as imaged by OM (data not shown). The passive region transfers to a transpassive region at about +0.3 $V_{Ag/AgCl}$ related to the dissolution of oxide and water oxidation. [69] These results are similar to other studies in similar electrolytes.[26, 70]

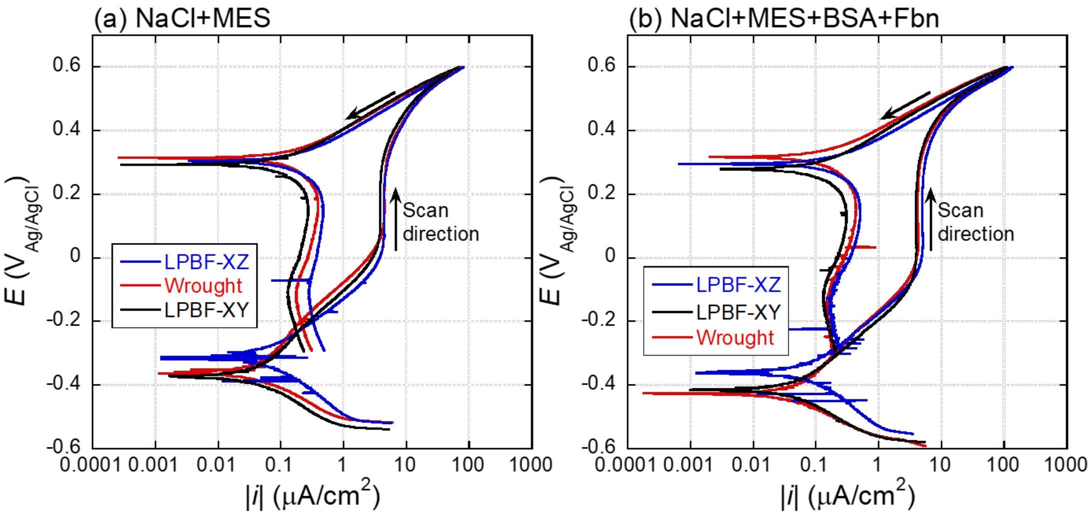

Figure 4. Representative cyclic potentiodynamic polarization curves, with the absolute current density (logarithmic scale) *versus* the potential vs. Ag/AgCl sat. KCl, of the wrought and LPBF (XY and XZ orientations) CoCrMo alloy in (a) NaCl+MES and (b) NaCl+MES+BSA+Fbn at 37 °C.

Table. 3. Passive current densities (i_{pass}) and corrosion potentials (E_{corr}) based on potentiodynamic polarization of the LPBF and wrought specimens after 1 h immersion in NaCl+MES and NaCl+MES+ BSA+Fbn solutions 37 °C. Each parameter is based on measurements for at least three replicate measurements showing the mean and standard deviations.

Solution	**Material**	β_a **(mV/decade)**	β_c **(mV/decade)**	i_{corr} **(µA/cm²)**	i_{pass} **(µA/cm²)**	E_{corr} **(mV$_{Ag/AgCl}$)**

NaCl+MES	LPBF-XY	181 ± 5	98 ± 15	0.035 ± 0.021	3.6 ± 0.8	−325 ± 7
	LPBF-XZ	159 ± 14	119 ± 9	0.043 ± 0.012	4.4 ± 0.1	−318 ± 1
	Wrought	189 ± 10	111 ± 13	0.037 ± 0.020	3.8 ± 1	−317 ± 5
NaCl+MES +BSA+Fbn	LPBF-XY	175 ± 12	91 ± 10	0.035 ± 0.008	3.6 ± 0.5	−430 ± 19
	LPBF-XZ	164 ± 3	117 ± 22	0.050 ± 0.013	4.5 ± 0.2	−390 ± 38
	Wrought	188 ± 3	85 ± 15	0.040 ± 0.014	4.0 ± 0.7	−429 ± 50

EIS measurements after 1 h immersion revealed, in agreement with the CPP measurements, that the corrosion resistance difference among the specimens was small. Again, consistently, the corrosion resistance of LPBF-XZ was the lowest, Figure 5 and Table 4, but this was not a statistically significant difference ($P \geq 0.05$). Also, the addition of proteins slightly weakened (not statistically significant, $P \geq 0.05$) the corrosion resistance of all CoCrMo specimens. A lower corrosion resistance in the presence of proteins is expected from literature data for CoCrMo[40] and for stainless steel 316L[70-71] in similar artificial physiological electrolytes. More EIS details are given in the supplementary information.

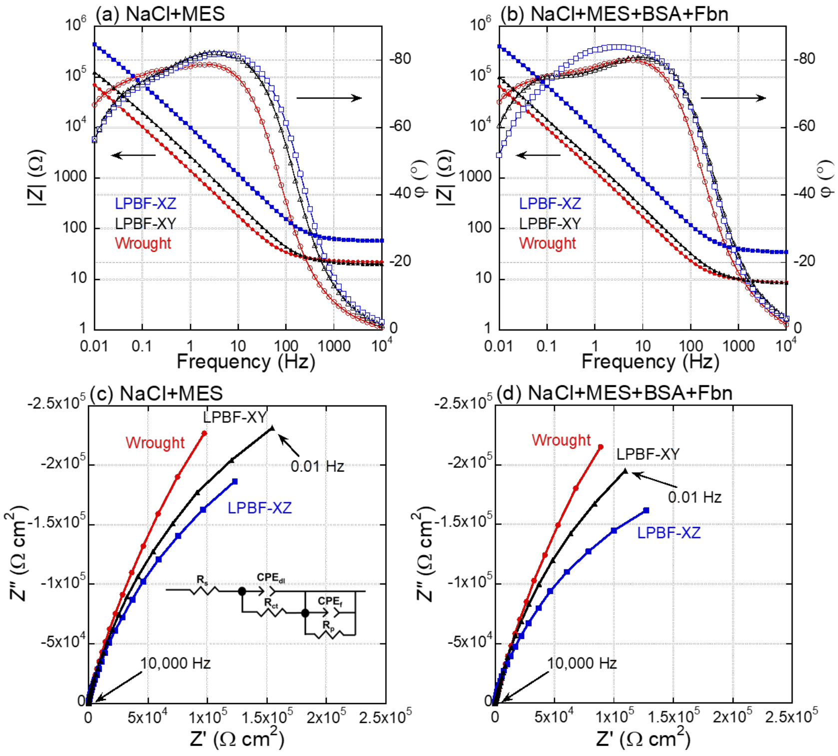

Figure 5. Representative EIS curves in (a,b) Bode format and (c,d) Nyquist format for wrought, LPBF-XY and LPBF-XZ in (a,c) NaCl+MES and (b,d) NaCl+MES+BSA+Fbn after 1 h OCP at 37 °C. Symbols represent the data points. In a and b, solid symbols correspond to the $|Z|$ axis and open symbols correspond to the φ axis. Inset in c: Equivalent circuit (EC) used for modeling the EIS data. R_s: solution resistance, CPE_{dl}: capacitance of the double layer, R_{ct}: charge transfer resistance, CPE_f: capacitance of the oxide film and R_p: polarization resistance.

Table 4. Fitting parameters acquired from the measured EIS data in NaCl+MES and NaCl+MES+BSA+Fbn (R_s: solution resistance, CPE_{dl}: capacitance of the double layer, R_{ct}: charge transfer resistance, CPE_f: capacitance of the oxide film, and R_p: polarization resistance). Mean and standard deviation of three measurements.

Electrolyte	**Sample**	**Electrochemical parameters**							
		R_s (Ω cm^2)	CPE_{dl} (Y_0, $\mu F cm^{-2} s^{-n}$)	n_1	R_{ct} (kΩ cm^2)	CPE_f (Y_0, $\mu F cm^{-2} s^{-n}$)	n_2	R_p (kΩ cm^2)	χ^2 (10^{-3})
NaCl+MES	LPBF-XY	46.4 ± 0.04	30.4 ± 1.2	0.93 ± 0.01	127.8 ± 2.5	10.5 ± 2.9	0.84 ± 0.01	651.4 ± 140.7	1.25 ± 0.07
	LPBF-XZ	55.2 ± 6.7	36.0 ± 2.1	0.93 ± 0.01	80.8 ± 22.0	14.2 ± 1.5	0.80 ± 0.09	437.6 ± 164.8	0.70 ± 0.5
	Wrought	64.0 ± 23.2	35.7 ± 3.9	0.91 ± 0.01	123.4 ± 49.2	11.8 ± 5.6	0.80 ± 0.07	973.5 ± 153	1.09 ± 0.5
NaCl+MES +BSA+Fbn	LPBF-XY	24 ± 9	55 ± 3	0.94 ± 0.01	100.7 ± 31	29 ± 8	0.80 ± 0.06	328.5 ± 50	0.1 ± 0.02
	LPBF-XZ	18 ± 4	41 ± 2	0.92 ± 0.02	151.7 ± 11	37 ± 5	0.93 ± 0.05	211.8 ± 133	0.1 ± 0.07
	Wrought	20 ± 2	61 ± 2	0.91 ± 0.01	42.7 ± 7.3	16 ± 3	0.73 ± 0.05	650.5 ± 133	0.1 ± 0.07

3.3. Metal release without friction

The released and non-precipitated amounts of Co, Cr and Mo in solution after contact with the wrought and LPBF specimens for 24 h in NaCl+MES and NaCl+MES+BSA+Fbn (both pH 7.3) are shown in Figure 6. The released amounts of Co, Cr, and Mo were significantly higher in the presence of proteins for most conditions, especially Cr release, and also depended on the microstructure. LPBF CoCrMo yielded more Cr and Mo release than the wrought CoCrMo. Furthermore, the release of all three metals (Co, Cr, and Mo) increased in the protein-rich solution as compared to the protein-free solution. In agreement with their highest corrosion current density and lowest polarization resistance presented in the previous sections, LPBF-XZ samples exhibited the highest metal release, Figure 6.

It is notable that the buffer choice (MES) seemed to have been a good choice to avoid metal-induced protein aggregation and metal phosphates that cause losses of released metals from solution by precipitation. The release of metals from the wrought CoCrMo was lower in NaCl+MES than in PBS in a comparable study[46] on the same material, but higher (especially for chromium) in NaCl+MES+BSA+Fbn than in PBS+BSA+Fbn under otherwise similar conditions. This indicates that especially Cr release is strongly underestimated in phosphate-containing and protein-containing solutions, and fits with observations of a strong effect of Cr ions on bone mineralization due to phosphate depletion.[6]

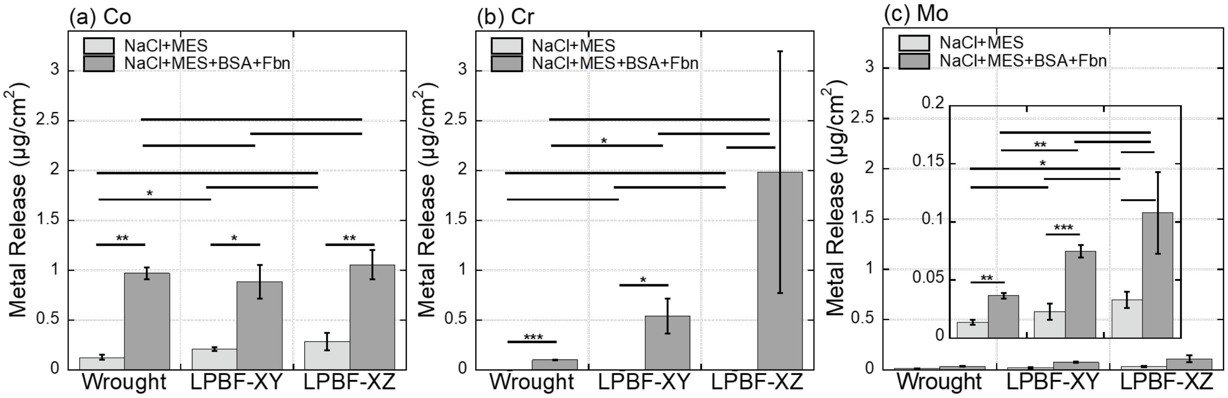

Figure 6. Released and non-precipitated amounts of Co, Cr and Mo per specimen surface area (μg/cm²) from CoCrMo specimens exposed to NaCl+MES or NaCl+MES+BSA+Fbn for 24 h at 37 °C, pH 7.3 ± 0.1. The error bars show the standard deviation between independent triplicate experiments. The inset in (c) is plotted with a smaller y-axis range to better show the range of Mo released. Asterisks indicate statistically significant differences; $P<0.05$ - *; $P<0.01$ - **, $P<0.001$ - ***.

3.4. Tribocorrosion examinations

In the absence of proteins, Fig. 7a, the COF was 0.30 ± 0.075 and largely fluctuating, indicative of particles or mechanical failures. The COF was lower in the presence of proteins, with 0.25 ± 0.036 in NaCl+MES+BSA and 0.20 ± 0.013 in NaCl+MES+BSA+Fbn. The only statistically significant ($P<0.05$) difference was for LPBF-XY between NaCl+MES and NaCl+MES+BSA+Fbn. A lower COF in the presence of proteins is expected due to the lubricating nature of proteins.[39, 72]

The OCP curves before, during, and after the friction period (Fig. 8) indicate that the greater COF for NaCl+MES compared with the presence of proteins, is caused by a greater activation of the surface. This is visible by *i*) a greater potential drop on the onset of friction after 60 min (Figs. 8a and d), and *ii*) larger fluctuations of the OCP during the friction period (Fig. 8a) in NaCl+MES compared with the other solutions. OCP fluctuations are caused by the passivation-activation transitions of the wear track in a tribocorrosion system.[73] The activation of the wear track is due to the mechanical removal or dissolution of the passive layer during the rubbing step (depassivation).[74-76] After stopping the friction (at 120 min), the potential increased for all specimens back to initial values, which is attributed to complete repassivation, Fig. 8.

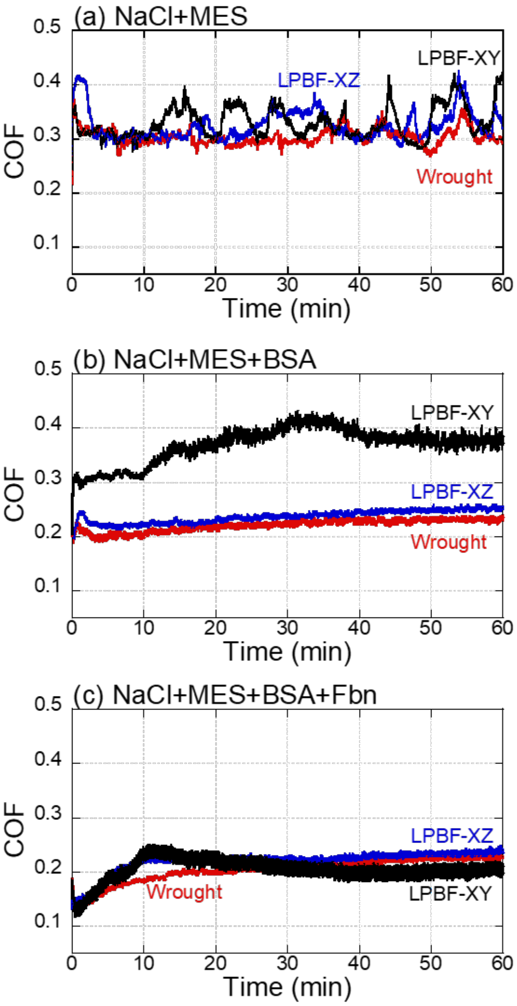

Figure 7. Representative coefficient of friction (COF) curves (during the 60 min sliding period only) *versus* time for the three CoCrMo specimens in three different solutions, all pH 7.3 at 37 °C: (a) NaCl+MES (no proteins), (b) NaCl+MES+BSA, and (c) NaCl+MES+BSA+Fbn.

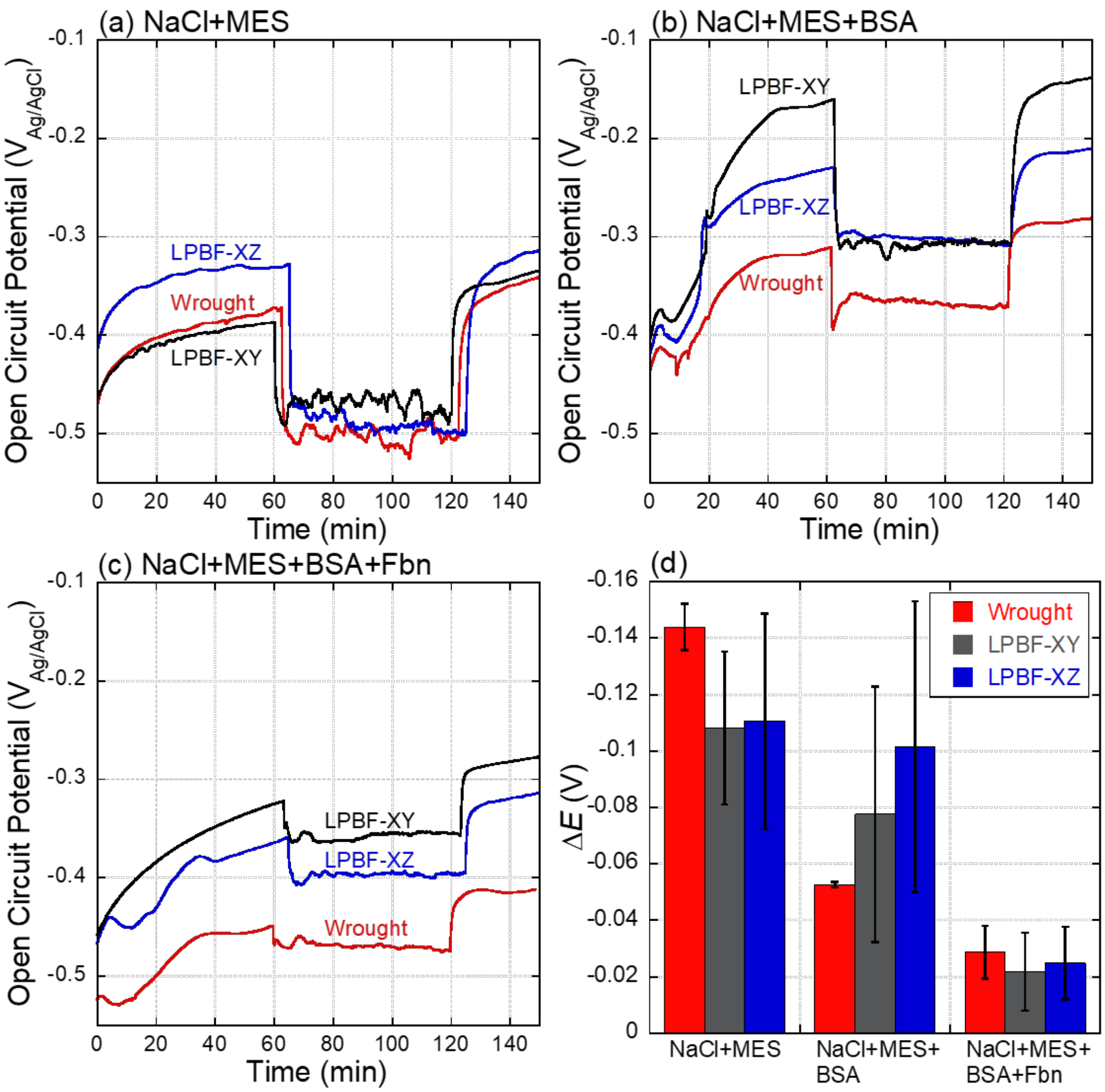

Figure 8. (a-c) Representative OCP measurements (vs. Ag/AgCl sat. KCl) during tribocorrosion examinations in NaCl+MES, NaCl+MES+BSA, and NaCl+MES+BSA+Fbn at pH 7.3 and 37 °C, and (d) the potential drop after 60 min (measured from 60 to 67 minutes for three measurements, with error bars being the standard deviations between the three measurements).

As visible in Figure 8d, the potential drops were not significantly different among the three specimen types, however, there was a significantly (P<0.05 for wrought and LPBF-XY) smaller drop for the NaCl+MES+BSA+Fbn solution than for NaCl+MES. Also, for the wrought CoCrMo, there was a significantly (P<0.05) smaller potential drop in NaCl+MES+BSA than NaCl+MES.

The post-examination of the wear tracks (Fig. 9) revealed grooves parallel to the sliding direction and oxidized patches, which is typical for CoCrMo.[77-78] Adhesive wear is a common wear mechanism during the sliding of metals against ceramic couples.[79] Plastic deformation and ploughing phenomena occurred on the surface of all the tested samples but the wear tracks of the protein-containing solutions appeared smoother and narrower. There was no clear difference between the three specimens in terms of wear track width, Fig. 9. The widest wear track was consistently found after tribocorrosion in NaCl+MES, while the presence of the proteins decreased the width of the wear track. Also, no solution at all (mechanical wear only) exhibited a narrower wear track because of the absence of corrosion, Fig. 9. EDS mapping and spot analysis in and outside of the wear tracks revealed the presence of carbon (C) and silicon (Si) along with the main metal elements (Co, Cr, and Mo). Oxygen (O) was also detected, with higher levels present within the wear track than outside of it (Figure S2, supplementary information). The higher levels of O within the wear track could originate from oxide and/or oxide particles formed during the repassivation of the surface.[78]

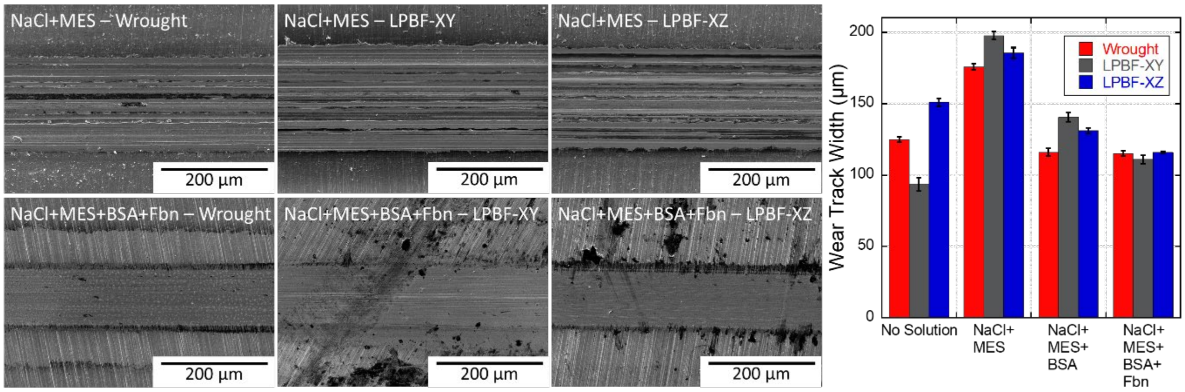

Figure 7. Left: Typical SEM images of the worn surfaces observed after tribocorrosion tests in NaCl+MES and NaCl+MES+BSA+Fbn at pH 7.3 and 37 °C. Right: Average wear track widths measured in five locations on one representative sample from each condition. The error bars show the standard deviation of the five measurements on a single specimen.

3.5. Surface compositional analysis by XPS

Figure 10 shows the normalized surface composition considering only Co, Cr, and Mo in the surface oxide and alloy beneath the surface oxide inside and outside of the wear track. In all cases, the observation of metallic species suggests the oxide film thickness was on the order of only a few nanometers. Oxide film thicknesses reported for a variety of Cr-containing alloys have been on the order of 1–3 nm.[80-82] When there was no solution, Figure 10a, there was a significantly higher fraction of Co dihydroxide and oxyhydroxide in the surface oxide. The oxidized Co species were even more abundant after friction (within the wear track). When exposed to the aqueous solution, Figure 10b–d, there was a substantial decrease in oxidized cobalt species, suggesting selective dissolution during immersion, leaving behind a Cr-rich oxide film. It is known that $Co(OH)_2$ and CoOOH are relatively soluble, in comparison to Cr, in aqueous solutions at pH 7.3.[83]

There was a significant increase in the surface oxide fraction, especially the trivalent chromium trihydroxide, within the wear track as compared to outside of the wear track, for all specimens and solutions. This increase in the surface oxide fraction suggests a relative increase in oxide film thickness within the wear track. The presence of $Cr(OH)_3$ is expected due to the interaction of the oxide with water and related hydrolysis reactions (through dissolution).[84]

There was also a relatively higher oxidized molybdenum fraction in the wear track for the NaCl+MES solution (for all three specimens), Figure 10b, as compared to outside of the wear track. This indicates a decrease in pH in the wear track (since molybdenum oxides have low solubility at low pH)[85] that is clearly influencing the corrosion. A 'cell separation' of both cathodic and anodic reactions, accompanied by local pH differences, is assumed to contribute strongly to tribocorrosion processes.[86-87] This effect is strongly suppressed in the presence of proteins, Figure 10c-d, as indicated by no significant increase in oxidized molybdenum in the wear track.

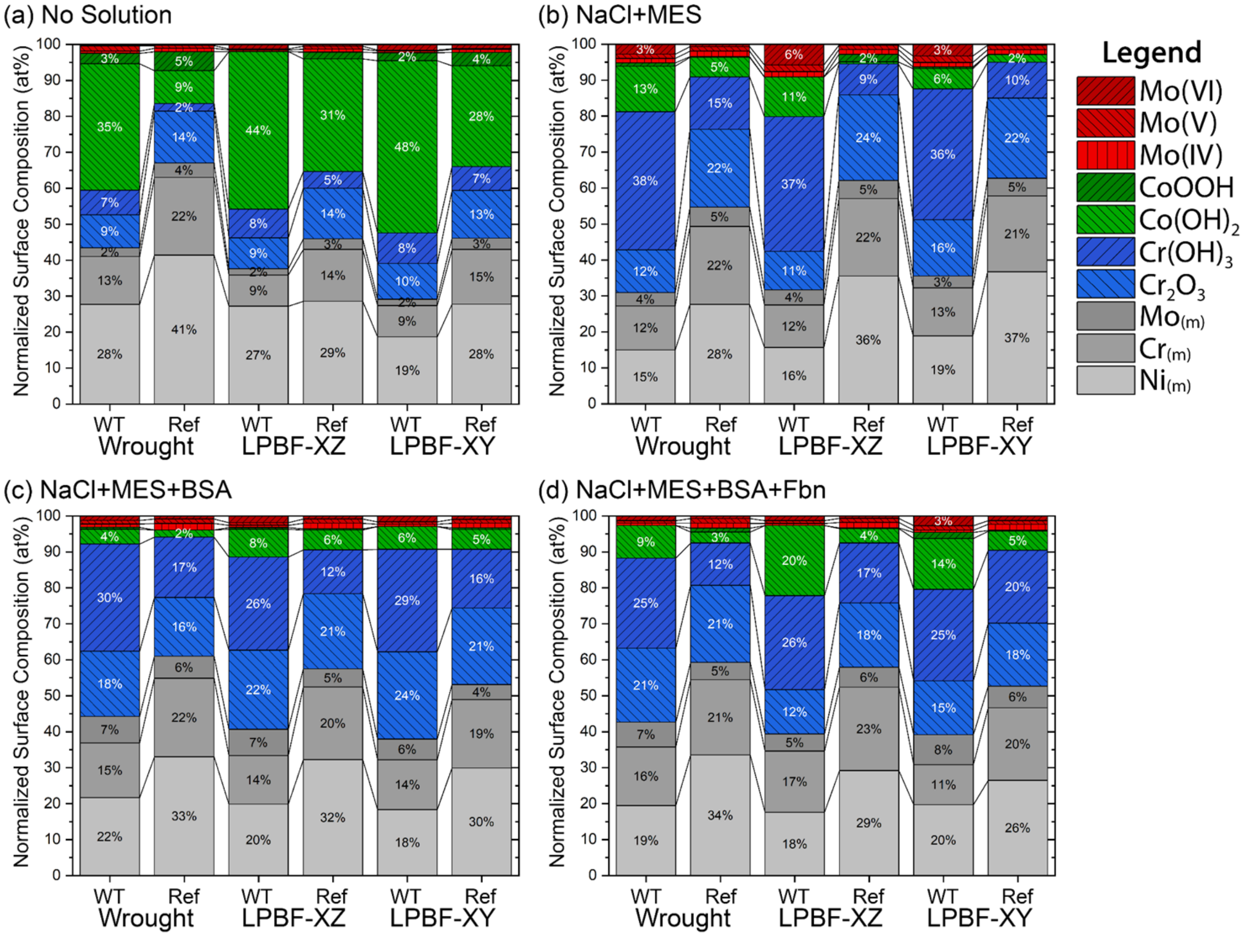

Figure 10. Relative atomic percentage and speciation of cobalt, chromium, and molybdenum for wrought, LPBF-XZ, and LPBF-XY CoCrMo. Outside ("Ref") and within wear track ("WT"): 1 h no sliding, followed by 1 h reciprocal linear sliding at 3 N load, followed by 0.5 h no sliding, at 37 °C at pH 7.3, either in (a) NaCl+MES, (b) NaCl+MES+BSA, (c) NaCl+MES+BSA+Fbn, or (d) no solution. m – metallic state. Corresponding raw data of fitted spectra is presented in the supplementary information.

Further, XPS revealed that the organic species, including the MES buffer and the proteins, adsorbed on the surface, with more details in the supplementary material.

3.6. Further discussion

In the absence of mechanical disruption of the surface oxide (absence of friction), the presence of proteins strongly increased metal release at OCP (no applied potential), and slightly increased corrosion, at pH 7.3 in this study. The effect was strongest for released Cr after 24 h immersion. The Cr release into protein-containing solution is higher than in comparable literature data,[46] for two reasons: i) a rinse of the surface of the CoCrMo coupons after the immersion test, with the rinsing water added to the solution sample,[46, 70] and ii) no phosphates in the buffer, which would have caused Co and Cr precipitation.[6, 46, 54] This work agrees with literature data on the increased dissolution of Co and Cr powders in saline solutions in the presence of BSA and Fbn.[88]

Tribocorrosion involves both mechanical action and chemical corrosion. In this study, it was clear from the wear track width that tribocorrosion was greater than pure mechanical wear. In the presence of the proteins, especially with the larger protein Fbn present, the COF and wear track width decreased significantly. The lubricating action of the proteins dominated the tribocorrosion process during the 60-minute period tested, which is similar to other studies.[89-91] Also, as visible from no significant Mo oxide buildup in the wear track (XPS), the protein layer might have had a local pH buffer effect and hindered or reduced the anodic/cathodic cell separation during tribocorrosion.[92] This is a very interesting finding, and the presented method to combine tribocorrosion and spot size XPS analysis might be an interesting path for future studies of tribocorrosion mechanisms in other systems, which should include other proteins and more complex solutions. In fact, another study on CoCrMo in various physiological solutions used a similar approach,[78] however, with no clear trends on Mo enrichment in wear tracks even in the absence of proteins.

In this study, the corrosion and metal release were slightly higher for the LPBF-XZ CoCrMo than for the LPBF-XY and wrought CoCrMo specimens (in the absence of friction). This cannot be explained by the phase, since LPBF-XY CoCrMo was the one deviating in terms of phase and grain orientation based on XRD. The density of both grain boundaries and metal carbides has been reported to be higher in the XY than the XZ plane,[26, 93] which has been used as an explanation for higher XY than XZ corrosion in H_2O_2-containing solutions[27] and 1% lactic acid[67] (the opposite of this study, in which XZ showed more corrosion than XY). Because of the low carbon content and heat treatment in this study, it is unlikely that secondary precipitations (carbides) would be a main factor. Our recent study[26] in PBS, citric acid, and PBS + citric acid concluded there was no significant difference in corrosion resistance between abraded LPBF-XY and LPBF-XZ CoCrMo, the same material as used in this study. Also, there was no significant difference in the surface oxide composition or thickness between LPBF-XY and LPBF-XZ, as determined by XPS in this study and for unexposed (just abraded) specimens in a previous study.[26] Hence, the increased metal release and corrosion of LPBF-XZ seen in this study are specific to the proteins (BSA and Fbn). LPBF-XZ has a higher density of melt pool boundaries and a slightly higher density of lack of fusion defects than LPBF-XY,[26] but it is unclear whether that would influence protein-induced corrosion processes.

In the presence of friction (in tribocorrosion investigations), no significant difference was found between the three different materials despite significantly different microstructure and microhardness. A previous study found superior tribocorrosion resistance for LPBF CoCrMo (0.04 wt.% C) compared with wrought CoCrMo (0.20 wt.% C) in a simulated body fluid without proteins.[94] This trend is similar to this study in NaCl+MES, but it was not statistically significant in this study, and there was no tribocorrosion difference among the materials in the presence of proteins.

In this study, LPBF CoCrMo (both XY and XZ) showed significantly higher Cr and Mo release than wrought CoCrMo into the protein-containing solution. This might be related to a quicker passivation (surface oxide formation with Cr enrichment) due to a higher grain boundary density of the LPBF CoCrMo.[67] This is also supported by XPS results (Fig. 10a), showing that the LBPF CoCrMo surface area without contact with the solution and outside of the wear track had a much thicker oxide enriched in Cr compared with the wrought specimen.

While tribocorrosion was decreased by proteins during the 60 min friction period in this study, it is unclear whether their ability to chemically increase corrosion and metal release would have an impact on tribocorrosion in longer tests. This should be investigated in future studies.

Conclusions

This study investigated the tribocorrosion behavior of LPBF fabricated in two different building orientations (XY and XZ) and a wrought CoCrMo in NaCl+MES+BSA+Fbn (pH 7.3) and reference solutions by electrochemical, tribocorrosion, surface and solution analytical methods. The following main conclusions can be drawn:

1. BSA and Fbn strongly enhanced the metal release (Co, Cr, and Mo) and slightly enhanced the corrosion (still in the passive domain) in static conditions (no friction) but decreased the extent of tribocorrosion due to lubrication during the 60 min sliding test.
2. There was no influence of the manufacturing process or building orientation on the tribocorrosion behavior, but LPBF-XZ, followed by LPBF-XY, exhibited the highest corrosion and metal release in the absence of friction.
3. The combination of BSA and Fbn provided the strongest lubrication effect and smallest OCP drop (smallest tribocorrosion) compared to BSA alone.
4. The wear track area was significantly more oxidized than the area outside of the wear track. In the reference solution NaCl+MES (without proteins), a strong Mo oxidation in the wear track surface oxide was indicative of a pH decrease and cell separation of anodic and cathodic areas. This effect was absent in the presence of proteins.

Notes

The authors declare no competing financial interest.

Acknowledgements

The authors thank Dr. Jonas Hedberg for assistance with the ICPMS measurement evaluation and Engineering Technician David Pacifico and Production Manager Tom Chmiel at Additive Design In Surgical Solutions, Inc, for the manufacturing and description of the LPBF specimens. The authors further thank the Taiho Kogyo Tribology Research Foundation (Grant No. 20B04), the Wolfe-Western fellowship, Canada [Grant No.: 2020]; Canada Research Chairs Program [Grant No.: CRC-2019-00425], the Ontario Research Fund [ER22-17-268], and the Natural Sciences and

Engineering Research Council of Canada [DGDND-2021-03997, RGPIN-2021-03997, RGPIN-2020-06856]. One of the authors (Masoud Atapour) wishes to express gratitude to the Invited Collaborative Research Program (ICRP), Center for International Scientific Studies and Collaboration, Ministry of Science, Research and Technology of Iran, for their support. Also, we wish to acknowledge the support from the Avicenna Center of Excellence.

References

1. Kremers, H. M.; Larson, D. R.; Crowson, C. S.; Kremers, W. K.; Washington, R. E.; Steiner, C. A.; Jiranek, W. A.; Berry, D. J., Prevalence of total hip and knee replacement in the United States. *J. Bone Joint Surg. Am.* **2015,** *97* (17), 1386, 10.2106/JBJS.N.01141.
2. Cross, M.; Smith, E.; Hoy, D.; Nolte, S.; Ackerman, I.; Fransen, M.; Bridgett, L.; Williams, S.; Guillemin, F.; Hill, C. L., The global burden of hip and knee osteoarthritis: estimates from the global burden of disease 2010 study. *Ann. Rheum. Dis.* **2014,** *73* (7), 1323-1330, 10.1136/annrheumdis-2013-204763.
3. Cornacchia, G.; Cecchel, S.; Battini, D.; Petrogalli, C.; Avanzini, A., Microstructural, mechanical, and tribological characterization of selective laser melted CoCrMo alloy under different heat treatment conditions and hot isostatic pressing. *Adv. Eng. Mater.* **2022,** *24* (4), 2100928, 10.1002/adem.202100928.
4. Chaudhary, S.; Avinashi, S. K.; Rao, J.; Gautam, C., Recent Advances in Additive Manufacturing, Applications and Challenges for Dentistry: A Review. *ACS Biomater. Sci. Eng.* **2023**, 10.1021/acsbiomaterials.2c01561.
5. Toh, W. Q.; Tan, X.; Bhowmik, A.; Liu, E.; Tor, S. B., Tribochemical characterization and tribocorrosive behavior of CoCrMo alloys: A review. *Materials* **2017,** *11* (1), 30, 10.3390/ma11010030.
6. Herbster, M.; Müller, E.; Jahn, J.; Buchholz, A.; Tootsi, K.; Lohmann, C. H.; Halle, T.; Bertrand, J., In vivo corrosion on retrieved hip endoprostheses and in vitro effects of corrosion products on bone mineralization. *Bone* **2023**, 116852, 10.1016/j.bone.2023.116852.
7. Tamayo, J. A.; Riascos, M.; Vargas, C. A.; Baena, L. M., Additive manufacturing of Ti6Al4V alloy via electron beam melting for the development of implants for the biomedical industry. *Heliyon* **2021,** *7* (5), e06892, https://doi.org/10.1016/j.heliyon.2021.e06892.
8. Villanueva, J.; Trino, L.; Thomas, J.; Bijukumar, D.; Royhman, D.; Stack, M.; Mathew, M., Corrosion, tribology, and tribocorrosion research in biomedical implants: progressive trend in the published literature. *Journal of Bio-and Tribo-Corrosion* **2017,** *3*, 1-8, 10.1007/s40735-016-0060-1.
9. Dini, C.; Costa, R. C.; Sukotjo, C.; Takoudis, C. G.; Mathew, M. T.; Barão, V. A., Progression of bio-tribocorrosion in implant dentistry. *Frontiers in Mechanical Engineering* **2020,** *6*, 1, 10.3389/fmech.2020.00001.
10. Liow, M. H. L.; Kwon, Y.-M., Metal-on-metal total hip arthroplasty: risk factors for pseudotumours and clinical systematic evaluation. *Int. Orthop.* **2017,** *41* (5), 885-892, 10.1007/s00264-016-3305-1.
11. Campbell, P.; Ebramzadeh, E.; Nelson, S.; Takamura, K.; De Smet, K.; Amstutz, H. C., Histological Features of Pseudotumor-like Tissues From Metal-on-Metal Hips. *Clinical Orthopaedics and Related Research®* **2010,** *468* (9), 2321-2327, 10.1007/s11999-010-1372-y.
12. Mahendra, G.; Pandit, H.; Kliskey, K.; Murray, D.; Gill, H. S.; Athanasou, N., Necrotic and inflammatory changes in metal-on-metal resurfacing hip arthroplasties. *Acta Orthop.* **2009,** *80* (6), 653-659, 10.3109/17453670903473016.
13. Xia, Z.; Kwon, Y.-M.; Mehmood, S.; Downing, C.; Jurkschat, K.; Murray, D. W., Characterization of metal-wear nanoparticles in pseudotumor following metal-on-metal hip resurfacing. *Nanomedicine: Nanotechnology, Biology and Medicine* **2011,** *7* (6), 674-681, https://doi.org/10.1016/j.nano.2011.08.002.

14. Bridges, R. L.; Cho, C. S.; Beck, M. R.; Gessner, B. D.; Tower, S. S., F-18 FDG PET brain imaging in symptomatic arthroprosthetic cobaltism. *European Journal of Nuclear Medicine and Molecular Imaging* **2020,** *47*, 1961–1970,
15. Chen, J. K.; Thyssen, J. P., *Metal allergy - from dermatitis to implant and device failure*. 1 ed.; Springer International Publishing: Cham, Switzerland, 2018.
16. Siverino, C.; Freitag, L.; Arens, D.; Styger, U.; Richards, R. G.; Moriarty, T. F.; Stadelmann, V. A.; Thompson, K., Titanium Wear Particles Exacerbate S. epidermidis-Induced Implant-Related Osteolysis and Decrease Efficacy of Antibiotic Therapy. *Microorganisms* **2021,** *9* (9), 1945,
17. Petrie, R. S.; Hanssen, A. D.; Osmon, D. R.; Ilstrup, D., Metal-backed patellar component failure in total knee arthroplasty: a possible risk for late infection. *Am J Orthop (Belle Mead NJ)* **1998,** *27* (3), 172-6,
18. Chisari, E.; Magnuson, J. A.; Ong, C. B.; Parvizi, J.; Krueger, C. A., Ceramic-on-polyethylene hip arthroplasty reduces the risk of postoperative periprosthetic joint infection. *Journal of Orthopaedic Research®* **2021**,
19. Bjørklund, G.; Dadar, M.; Aaseth, J., Delayed-type hypersensitivity to metals in connective tissue diseases and fibromyalgia. *Environ. Res.* **2018,** *161*, 573-579, https://doi.org/10.1016/j.envres.2017.12.004.
20. Mace, A.; Khullar, P.; Bouknight, C.; Gilbert, J. L., Corrosion properties of low carbon CoCrMo and additively manufactured CoCr alloys for dental applications. *Dent. Mater.* **2022,** *38* (7), 1184-1193, 10.1016/j.dental.2022.06.021.
21. Al Jabbari, Y. S.; Karavoltsos, S.; Kokkinos, C.; Polychronis, G.; Economou, A.; Zinelis, S., Electrochemical characterization of three types of Co-Cr based alloys manufactured by casting and selective laser melting according to ISO 10271. *Dent. Mater.* **2022,** *38* (7), 1162-1172, 10.1016/j.dental.2022.06.005.
22. Hedberg, Y.; Qian, B.; Zhijian, S.; Virtanen, S.; Odnevall Wallinder, I., In-vitro biocompatibility of CoCrMo dental alloys fabricated by selective laser melting. *Dent. Mater.* **2014,** *30* (5), 525-534, 10.1016/j.dental.2014.02.008.
23. Mazumder, S.; Man, K.; Radhakrishnan, M.; Pantawane, M. V.; Palaniappan, S.; Patil, S. M.; Yang, Y.; Dahotre, N. B., Microstructure enhanced biocompatibility in laser additively manufactured CoCrMo biomedical alloy. *Biomaterials Advances* **2023,** *150*, 213415, https://doi.org/10.1016/j.bioadv.2023.213415.
24. Munyensanga, P.; Bricha, M.; El Mabrouk, K., Functional characterization of biomechanical loading and biocorrosion resistance properties of novel additively manufactured porous CoCrMo implant: Comparative analysis with gyroid and rhombic dodecahedron. *Mater. Chem. Phys.* **2024,** *316*, 129139, https://doi.org/10.1016/j.matchemphys.2024.129139.
25. Alaloosi, R. A.; Çomakli, O.; Yazici, M.; Taha, Z. A., Effect of scan speed on corrosion and tribocorrosion properties of cobalt-chromium alloy produced by selective laser melting. *Rapid Prototyping Journal* **2024,** *30* (3), 405-414, 10.1108/RPJ-02-2023-0068.
26. Atapour, M.; Sanaei, S.; Wei, Z.; Sheikholeslam, M.; Henderson, J. D.; Eduok, U.; Hosein, Y. K.; Holdsworth, D. W.; Hedberg, Y. S.; Ghorbani, H. R., In vitro corrosion and biocompatibility behavior of CoCrMo alloy manufactured by laser powder bed fusion parallel and perpendicular to the build direction. *Electrochim. Acta* **2023,** *445*, 142059, https://doi.org/10.1016/j.electacta.2023.142059.

27. Hu, Y.; Dong, C.; Kong, D.; Ao, M.; Ding, J.; Ni, X.; Zhang, L.; Yi, P.; Li, X., Degradation behaviour of selective laser melted CoCrMo alloys in H2O2-containing chloride solutions. *Corros. Sci.* **2022,** *195*, 109981,

28. Yan, Y.; Neville, A.; Dowson, D.; Williams, S., Tribocorrosion in implants—assessing high carbon and low carbon Co–Cr–Mo alloys by in situ electrochemical measurements. *Tribol. Int.* **2006,** *39* (12), 1509-1517, 10.1016/j.triboint.2006.01.016.

29. Gan, Y.; Zhou, M.; Ji, C.; Huang, G.; Chen, Y.; Li, L.; Huang, T.; Lu, Y.; Lin, J., Tailoring the tribology property and corrosion resistance of selective laser melted CoCrMo alloys by varying copper content. *Mater. Des.* **2023,** *228*, 111869, 10.1016/j.matdes.2023.111869.

30. Igual Munoz, A.; Schwiesau, J.; Jolles, B. M.; Mischler, S., In vivo electrochemical corrosion study of a CoCrMo biomedical alloy in human synovial fluids. *Acta Biomater.* **2015,** *21*, 228-236, 10.1016/j.actbio.2015.03.008.

31. Hedberg, Y. S., Role of proteins in the degradation of relatively inert alloys in the human body. *npj Materials Degradation* **2018,** *2*, 26, 10.1038/s41529-018-0049-y.

32. Lewis, A. C.; Kilburn, M. R.; Papageorgiou, I.; Allen, G. C.; Case, C. P., Effect of synovial fluid, phosphate-buffered saline solution, and water on the dissolution and corrosion properties of CoCrMo alloys as used in orthopedic implants. *J. Biomed. Mater. Res. A* **2005,** *73A* (4), 456-467, 10.1002/jbm.a.30368.

33. Okazaki, Y.; Gotoh, E., Comparison of metal release from various metallic biomaterials in vitro. *Biomaterials* **2005,** *26* (1), 11-21,

34. Muñoz, A. I.; Mischler, S., Electrochemical Quartz Crystal Microbalance and X-Ray Photoelectron Spectroscopy study of cathodic reactions in Bovine Serum Albumin containing solutions on a Physical Vapour Deposition-CoCrMo biomedical alloy. *Electrochim. Acta* **2015,** *180*, 96-103, https://doi.org/10.1016/j.electacta.2015.08.017.

35. Milošev, I., The effect of biomolecules on the behaviour of CoCrMo alloy in various simulated physiological solutions. *Electrochim. Acta* **2012,** *78*, 259-273, 10.1016/j.electacta.2012.05.146.

36. Liu, Y.; Gilbert, J. L., The effect of simulated inflammatory conditions and Fenton chemistry on the electrochemistry of CoCrMo alloy. *J. Biomed. Mater. Res. B* **2018,** *106* (1), 209-220, 10.1002/jbm.b.33830.

37. Radice, S.; Yao, J.; Babauta, J.; Laurent, M.; Wimmer, M., The effect of hyaluronic acid on the corrosion of an orthopedic CoCrMo-alloy in simulated inflammatory conditions. *Materialia* **2019,** *6*, 100348, 10.1016/j.mtla.2019.100348.

38. Igual Muñoz, A.; Julián, L. C., Influence of electrochemical potential on the tribocorrosion behaviour of high carbon CoCrMo biomedical alloy in simulated body fluids by electrochemical impedance spectroscopy. *Electrochim. Acta* **2010,** *55* (19), 5428-5439, 10.1016/j.electacta.2010.04.093.

39. Mathew, M. T.; Jacobs, J. J.; Wimmer, M. A., Wear-Corrosion Synergism in a CoCrMo Hip Bearing Alloy Is Influenced by Proteins. *Clinical Orthopaedics and Related Research®* **2012,** *470* (11), 3109-3117, 10.1007/s11999-012-2563-5.

40. de Castro Girão, D.; Béreš, M.; Jardini, A. L.; Filho, R. M.; Silva, C. C.; de Siervo, A.; Gomes de Abreu, H. F.; Araújo, W. S., An assessment of biomedical CoCrMo alloy fabricated by direct metal laser sintering technique for implant applications. *Mater. Sci. Eng. C* **2020,** *107*, 110305, 10.1016/j.msec.2019.110305.

41. Liao, Y.; Pourzal, R.; Wimmer, M. A.; Jacobs, J. J.; Fischer, A.; Marks, L. D., Graphitic Tribological Layers in Metal-on-Metal Hip Replacements. *Science* **2011,** *334* (6063), 1687-1690, 10.1126/science.1213902.

42. Espallargas, N.; Fischer, A.; Igual Muñoz, A.; Mischler, S.; Wimmer, M. A., In-situ generated tribomaterial in metal/metal contacts: Current understanding and future implications for implants. *Biotribology* **2017,** *10*, 42-50, 10.1016/j.biotri.2017.03.006.

43. Singh, J.; Mahajan, A.; Agnihotri, A.; Handa, R., A Concise Study on Tribological Properties of Additive Manufactured Biomaterials. In *Additive Manufacturing of Bio-implants: Design and Synthesis*, Mahajan, A.; Devgan, S.; Zitoune, R., Eds. Springer Nature Singapore: Singapore, 2024; pp 107-114.

44. Joshua, R. J.; Raj, S. A.; Hameed Sultan, M. T.; Łukaszewicz, A.; Józwik, J.; Oksiuta, Z.; Dziedzic, K.; Tofil, A.; Shahar, F. S. Powder Bed Fusion 3D Printing in Precision Manufacturing for Biomedical Applications: A Comprehensive Review *Materials* [Online], 2024.

45. Pothala, S.; Jagannadha Raju, M. V., Recent advances of metallic bio-materials in additive manufacturing in biomedical implants–A review. *Materials Today: Proceedings* **2023**, https://doi.org/10.1016/j.matpr.2023.07.109.

46. Wei, Z.; Romanovski, V.; Filho, L.; Persson, C.; Hedberg, Y. S., Metal Release from a Biomedical CoCrMo Alloy in Mixed Protein Solutions Under Static and Sliding Conditions: Effects of Protein Aggregation and Metal Precipitation. *Journal of Bio- and Tribo-Corrosion* **2022,** *8* (1), 19, 10.1007/s40735-021-00617-1.

47. Peters, T. J., Serum Albumin. *Advances in protein chemistry* **1985,** *37*, 161-245,

48. Bennike, T.; Ayturk, U.; Haslauer, C. M.; Froehlich, J. W.; Proffen, B. L.; Barnaby, O.; Birkelund, S.; Murray, M. M.; Warman, M. L.; Stensballe, A.; Steen, H., A normative study of the synovial fluid proteome from healthy porcine knee joints. *J Proteome Res* **2014,** *13* (10), 4377-87, 10.1021/pr500587x.

49. Lundin, M.; Hedberg, Y.; Jiang, T.; Herting, G.; Wang, X.; Thormann, E.; Blomberg, E.; Odnevall Wallinder, I., Adsorption and protein-induced metal release from chromium metal and stainless steel. *J. Colloid Interf. Sci.* **2012,** *366*, 155-164, 10.1016/j.jcis.2011.09.068.

50. Qiu, J.; Yu, Y.; Fu, Y.; Ye, F.; Xie, X.; Lu, W., Preoperative plasma fibrinogen, platelet count and prognosis in epithelial ovarian cancer. *Journal of Obstetrics and Gynaecology Research* **2012,** *38* (4), 651-657, 10.1111/j.1447-0756.2011.01780.x.

51. Wasilewska, M.; Adamczyk, Z.; Jachimska, B., Structure of fibrinogen in electrolyte solutions derived from dynamic light scattering (DLS) and viscosity measurements. *Langmuir* **2009,** *25* (6), 3698-3704, 10.1021/la803662a.

52. Herrick, S.; Blanc-Brude, O.; Gray, A.; Laurent, G., Fibrinogen. *The international journal of biochemistry & cell biology* **1999,** *31* (7), 741-746, 10.1016/S1357-2725(99)00032-1.

53. Fukuzaki, S.; Urano, H.; Nagata, K., Adsorption of protein onto stainless-steel surfaces. *J. Ferment. Bioeng.* **1995,** *80* (1), 6-11, 10.1016/0922-338X(95)98168-K.

54. Hedberg, Y. S.; Dobryden, I.; Chaudhary, H.; Wei, Z.; Claesson, P.; Lendel, C., Synergistic effects of metal-induced aggregation of human serum albumin. *Colloid Surface B* **2019,** *173*, 751-758, 10.1016/j.colsurfb.2018.10.061.

55. Mash, H. E.; Chin, Y.-P.; Sigg, L.; Hari, R.; Xue, H., Complexation of copper by zwitterionic aminosulfonic (good) buffers. *Anal. Chem.* **2003,** *75* (3), 671-677,

56. Biesinger, M. C., Accessing the Robustness of Adventitious Carbon for Charge Referencing (Correction) Purposes in XPS Analysis: Insights from a Multi-User Facility Data Review. *Appl. Surf. Sci.* **2022**, 153681, 10.1016/j.apsusc.2022.153681.

57. Biesinger, M.; Brown, C.; Mycroft, J.; Davidson, R.; McIntyre, N., X-ray photoelectron spectroscopy studies of chromium compounds. *Surf. Interface Anal.* **2004,** *36* (12), 1550-1563, 10.1002/sia.1983.

58. Biesinger, M. C.; Payne, B. P.; Grosvenor, A. P.; Lau, L. W. M.; Gerson, A. R.; Smart, R. S. C., Resolving surface chemical states in XPS analysis of first row transition metals, oxides and hydroxides: Cr, Mn, Fe, Co and Ni. *Appl. Surf. Sci.* **2011,** *257* (7), 2717-2730, 10.1016/j.apsusc.2010.10.051.

59. Spevack, P.; McIntyre, N., Thermal reduction of MoO_3. *J. Phys. Chem.-US* **1992,** *96* (22), 10.1021/j100201a062.

60. Zhang, Y.; Lin, W.; Zhai, Z.; Wu, Y.; Yang, R.; Zhang, Z., Enhancing the mechanical property of laser powder bed fusion CoCrMo alloy by tailoring the microstructure and phase constituent. *Mater. Sci. Eng. A* **2023,** *862*, 144449, 10.1016/j.msea.2022.144449.

61. Lanzutti, A.; Andreatta, F.; Vaglio, E.; Sortino, M.; Totis, G.; Fedrizzi, L., Effects of post-printing heat treatment on microstructure, corrosion and wet wear behavior of CoCrW alloy produced by L-PBF process. *Progress in Additive Manufacturing* **2023**, 10.1007/s40964-023-00414-x.

62. Xiang, D. D.; Wang, P.; Tan, X. P.; Chandra, S.; Wang, C.; Nai, M. L. S.; Tor, S. B.; Liu, W. Q.; Liu, E., Anisotropic microstructure and mechanical properties of additively manufactured Co–Cr–Mo alloy using selective electron beam melting for orthopedic implants. *Mater. Sci. Eng. A* **2019,** *765*, 138270, https://doi.org/10.1016/j.msea.2019.138270.

63. Tan, X. P.; Wang, P.; Kok, Y.; Toh, W. Q.; Sun, Z.; Nai, S. M. L.; Descoins, M.; Mangelinck, D.; Liu, E.; Tor, S. B., Carbide precipitation characteristics in additive manufacturing of Co-Cr-Mo alloy via selective electron beam melting. *Scripta Materialia* **2018,** *143*, 117-121, https://doi.org/10.1016/j.scriptamat.2017.09.022.

64. Milošev, I., CoCrMo alloy for biomedical applications. In *Biomedical Applications*, Springer: 2012; pp 1-72.

65. Li, H.; Wang, M.; Lou, D.; Xia, W.; Fang, X., Microstructural features of biomedical cobalt–chromium–molybdenum (CoCrMo) alloy from powder bed fusion to aging heat treatment. *Journal of Materials Science & Technology* **2020,** *45*, 146-156, 10.1007/s40964-023-00414-x.

66. Tonelli, L.; Fortunato, A.; Ceschini, L., CoCr alloy processed by Selective Laser Melting (SLM): Effect of Laser Energy Density on microstructure, surface morphology, and hardness. *Journal of Manufacturing Processes* **2020,** *52*, 106-119,

67. Gong, X.; Li, Y.; Nie, Y.; Huang, Z.; Liu, F.; Huang, L.; Jiang, L.; Mei, H., Corrosion behaviour of CoCrMo alloy fabricated by electron beam melting. *Corros. Sci.* **2018,** *139*, 68-75, 10.1016/j.corsci.2018.04.033.

68. Li, J.; Ren, H.; Liu, C.; Shang, S., The effect of specific energy density on microstructure and corrosion resistance of CoCrMo alloy fabricated by laser metal deposition. *Materials* **2019,** *12* (8), 1321, 10.3390/ma12081321.

69. Li, H.; Guo, H.; Shen, F.; Lou, D.; Xia, W.; Fang, X., Tribological and corrosion performance of the plasma-sprayed conformal ceramic coating on selective laser melted CoCrMo alloy. *J. Mech. Behav. Biomed. Mater.* **2021,** *119*, 104520, 10.1016/j.jmbbm.2021.104520.

70. Atapour, M.; Wang, X.; Färnlund, K.; Odnevall Wallinder, I.; Hedberg, Y., Corrosion and metal release investigations of selective laser melted 316L stainless steel in a synthetic

physiological fluid containing proteins and in diluted hydrochloric acid. *Electrochim. Acta* **2020,** *354*, 136748, https://doi.org/10.1016/j.electacta.2020.136748.
71. Atapour, M.; Odnevall Wallinder, I.; Hedberg, Y., Stainless steel in simulated milk and whey protein solutions – Influence of grade on corrosion and metal release. *Electrochim. Acta* **2020,** *331*, 135428, https://doi.org/10.1016/j.electacta.2019.135428.
72. Wang, Z.; Yan, Y.; Su, Y.; Qiao, L., Effect of proteins on the surface microstructure evolution of a CoCrMo alloy in bio-tribocorrosion processes. *Colloid Surface B* **2016,** *145*, 176-184, 10.1016/j.colsurfb.2016.05.002.
73. Ben Saada, F.; Ben Saada, M.; Elleuch, K.; Ponthiaux, P. Nanocrystallized Surface Effect on the Tribocorrosion Behavior of AISI 420 *Lubricants* [Online], 2022.
74. Purandare, Y.; Shukla, K.; Sugumaran, A.; Ehiasarian, A.; Khan, I.; Hovsepian, P., Improving tribocorrosion resistance of a medical grade CoCrMo alloy by the novel HIPIMS nitriding technique. *Journal of Science: Advanced Materials and Devices* **2023,** *8* (3), 100570, 10.1016/j.jsamd.2023.100570.
75. Yilmazer, H.; Caha, I.; Dikici, B.; Toptan, F.; Isik, M.; Niinomi, M.; Nakai, M.; Alves, A. C., Investigation of the Influence of High-Pressure Torsion and Solution Treatment on Corrosion and Tribocorrosion Behavior of CoCrMo Alloys for Biomedical Applications. *Crystals* **2023,** *13* (4), 590, 10.3390/cryst13040590.
76. Buciumeanu, M.; Bagheri, A.; Souza, J.; Silva, F.; Henriques, B., Tribocorrosion behavior of hot pressed CoCrMo alloys in artificial saliva. *Tribol. Int.* **2016,** *97*, 423-430, 10.1016/j.triboint.2016.02.007.
77. Cassar, J.; Mallia, B.; Mazzonello, A.; Karl, A.; Buhagiar, J., Improved tribocorrosion resistance of a CoCrMo implant material by carburising. *Lubricants* **2018,** *6* (3), 76, 10.3390/lubricants6030076.
78. Taufiqurrakhman, M.; Bryant, M. G.; Neville, A., Tribofilms on CoCrMo alloys: Understanding the role of the lubricant. *Biotribology* **2019,** *19*, 100104, 10.1016/j.biotri.2019.100104.
79. Toptan, F.; Alves, A. C.; Carvalho, Ó.; Bartolomeu, F.; Pinto, A. M.; Silva, F.; Miranda, G., Corrosion and tribocorrosion behaviour of Ti6Al4V produced by selective laser melting and hot pressing in comparison with the commercial alloy. *J. Mater. Process. Tech.* **2019,** *266*, 239-245, 10.1016/j.jmatprotec.2018.11.008.
80. Lutton, K.; Gusieva, K.; Ott, N.; Birbilis, N.; Scully, J. R., Understanding multi-element alloy passivation in acidic solutions using operando methods. *Electrochemistry Communications* **2017,** *80*, 44-47, 10.1016/j.elecom.2017.05.015.
81. Gardin, E.; Zanna, S.; Seyeux, A.; Allion-Maurer, A.; Marcus, P., XPS and ToF-SIMS characterization of the surface oxides on lean duplex stainless steel–Global and local approaches. *Corros. Sci.* **2019,** *155*, 121-133, 10.1016/j.corsci.2019.04.039.
82. Hanawa, T.; Hiromoto, S.; Asami, K., Characterization of the surface oxide film of a Co–Cr–Mo alloy after being located in quasi-biological environments using XPS. *Appl. Surf. Sci.* **2001,** *183* (1), 68-75, 10.1016/S0169-4332(01)00551-7.
83. Chivot, J.; Mendoza, L.; Mansour, C.; Pauporté, T.; Cassir, M., New insight in the behaviour of Co–H2O system at 25–150 °C, based on revised Pourbaix diagrams. *Corros. Sci.* **2008,** *50* (1), 62-69, 10.1016/j.corsci.2007.07.002.
84. Zhang, X.; Zagidulin, D.; Shoesmith, D. W., Characterization of film properties on the NiCrMo Alloy C-2000. *Electrochim. Acta* **2013,** *89*, 814-822, 10.1016/j.electacta.2012.11.029.

85. Peña-Bahamonde, J.; Wu, C.; Fanourakis, S. K.; Louie, S. M.; Bao, J.; Rodrigues, D. F., Oxidation state of Mo affects dissolution and visible-light photocatalytic activity of MoO3 nanostructures. *J. Catal.* **2020,** *381*, 508-519, 10.1016/j.jcat.2019.11.035.
86. Vieira, A.; Ribeiro, A.; Rocha, L.; Celis, J.-P., Influence of pH and corrosion inhibitors on the tribocorrosion of titanium in artificial saliva. *Wear* **2006,** *261* (9), 994-1001, 10.1016/j.wear.2006.03.031.
87. Zhang, Y.; Yin, X.; Yan, Y.; Wang, J.; Yan, F., Tribocorrosion behaviors of 304SS: effect of solution pH. *Rsc Advances* **2015,** *5* (23), 17676-17682, 10.1039/C4RA13728K.
88. Clark, G. C. F.; Williams, D. F., The effects of proteins on metallic corrosion. *J. Biomed. Mater. Res.* **1982,** *16* (2), 125-134, 10.1002/jbm.820160205.
89. Taufiqurrakhman, M.; Neville, A.; Bryant, M. G., The effect of protein structure and concentration on tribocorrosion and film formation on CoCrMo alloys. *Journal of Bio-and Tribo-Corrosion* **2021,** *7*, 1-18, 10.1007/s40735-021-00585-6.
90. Talha, M.; Ma, Y.; Kumar, P.; Lin, Y.; Singh, A., Role of protein adsorption in the bio corrosion of metallic implants–a review. *Colloid Surface B* **2019,** *176*, 494-506, 10.1016/j.colsurfb.2019.01.038.
91. Yang, S.; Pu, J.; Zhang, X.; Zhang, Y.; Cui, W.; Xie, F.; Lu, W.; Tan, Q.; Jin, Z., A preliminary experimental investigation on the biotribocorrosion of a metal-on-polyethylene hip prosthesis in a hip simulator. *Friction* **2023,** *11* (6), 1094-1106, 10.1007/s40544-022-0655-0.
92. Wood, R. J., Tribocorrosion. *Developments in Electrochemistry* **2014**, 281-294, 10.1002/9781118694404.ch15.
93. Chen, Z.; Lu, C.; Zhuo, Y.; Xia, Z.; Zhu, X.; Wang, C.; Jia, Q., Ductility enhancement of additively manufactured CoCrMo alloy via residual stress tailored high stacking fault probability. *Scripta Materialia* **2023,** *235*, 115626, 10.1016/j.scriptamat.2023.115626.
94. Efremenko, V. G.; Lekatou, A. G.; Chabak, Y. G.; Efremenko, B. V.; Petryshynets, I.; Zurnadzhy, V. I.; Emmanouilidou, S.; Vojtko, M., Micromechanical, corrosion and wet sliding wear behaviours of Co-28Cr-6Mo alloy: Wrought vs. LPBF. *Materials Today Communications* **2023,** *35*, 105936, https://doi.org/10.1016/j.mtcomm.2023.105936.

Supplementary information

Influence of Proteins and Building Direction on the Corrosion and Tribocorrosion of CoCrMo Fabricated by Laser Powder Bed Fusion

Masoud Atapour, Thalia E. Standish, Jeffrey D. Henderson, Zheng Wei, Vahid Dehnavi, Yolanda S. Hedberg

OCP

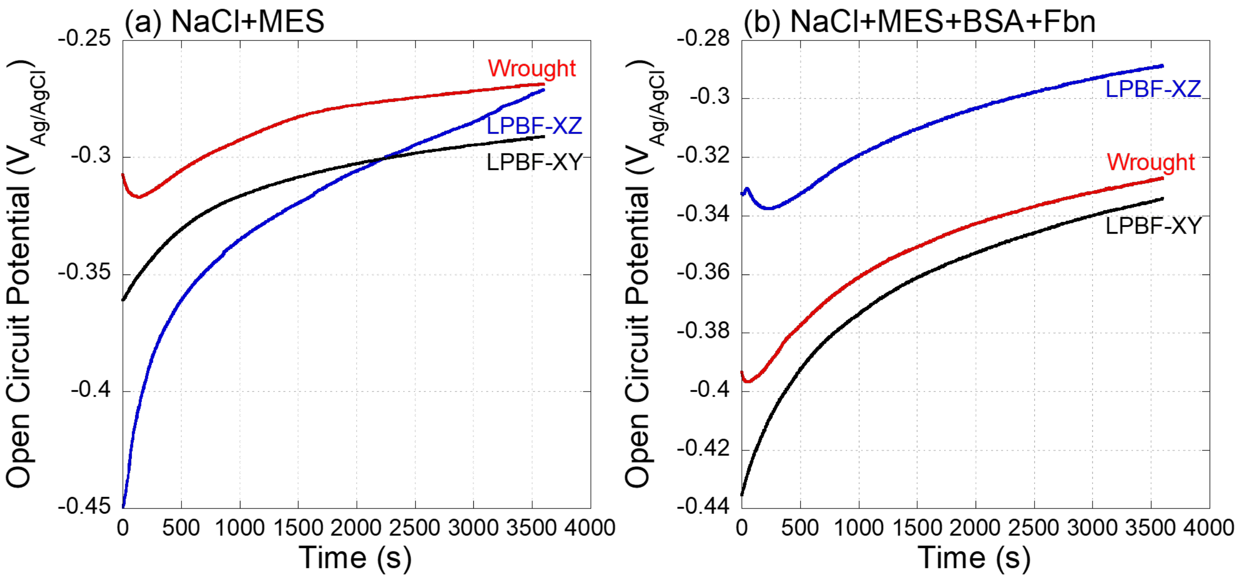

Figure S1. Representative curves of OCP vs. time recorded on LPBF and wrought CoCrMo samples for 1 h at 37 °C in (a) NaCl+MES and (b) NaCl+MES+BSA+Fbn.

Details on EIS

In this research, EIS data were fitted using a two-time constant circuit (inset in Fig. 5c in main manuscript), as reported by previous studies investigating the corrosion resistance of the CoCrMo alloy in simulated physiological solutions.[1-3] In this circuit, R_s is the solution resistance, CPE_{dl} represents the capacitance of the double layer, R_{ct} is the charge transfer resistance, CPE_f shows the capacitance of the oxide film and R_p is the polarization resistance of the system.[1] A constant phase element (CPE) was used to replace the capacitor because of non-ideal behavior of the capacitive elements due to the presence of surface roughness, impurities, dislocations, and grain boundaries. CPE is defined in impedance representation as:

$$Z(\omega) = Z_0(i\omega)^{-n}$$

where Z_0 is the *CPE* constant, ω is the angular frequency (in rad/s), $i^2 = -1$ is the imaginary number and n is the *CPE* exponent. Depending on n, *CPE* can represent resistance ($n = 0$, $Z_0 = R$), capacitance ($n = 1$, $Z_0 = C$), or Warburg impedance ($n = 0.5$, $Z_0 = W$).

Very close values of R_s were recorded in NaCl+MES and NaCl+MES+BSA+Fbn (Table 4, main manuscript) solutions for the LPBF and wrought samples. However, the addition of proteins decreased the R_s, in accordance with previous work.[1]

EDS analysis

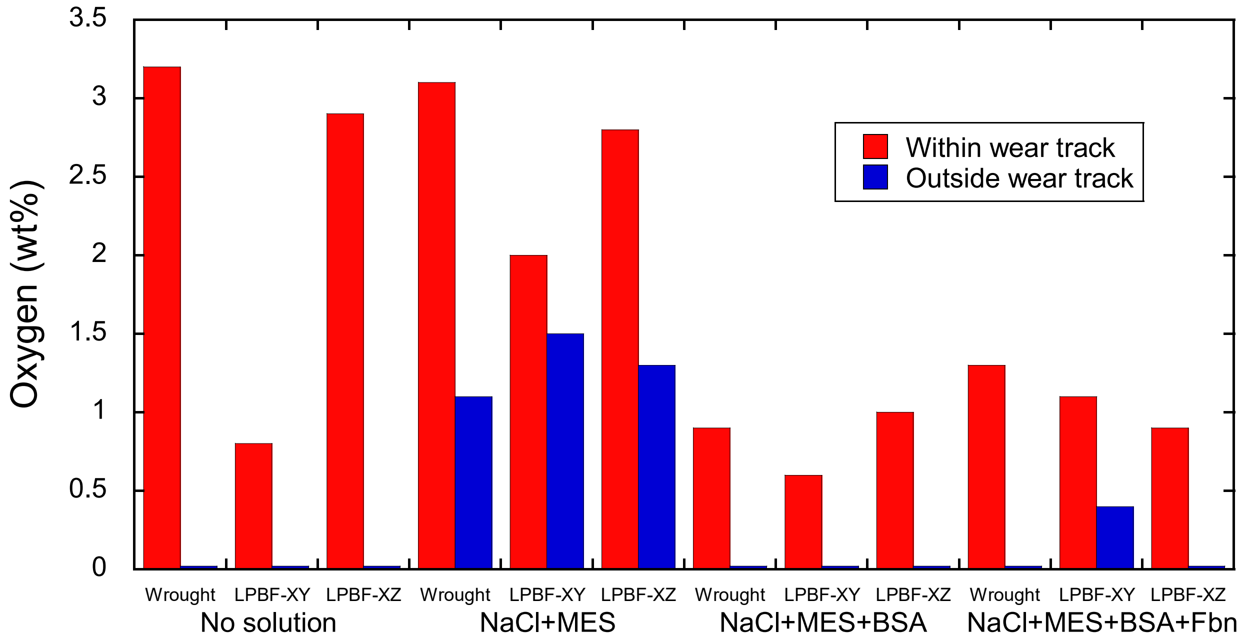

Figure S2. The amount of oxygen detected within and outside of the wear track by means of EDS spot analysis on wrought, LPBF-XY, and LPBF-XZ CoCrMo after tribocorrosion in no solution, NaCl+MES, MaCl+MES+BSA, and NaCl+MES+BSA+Fbn, at 37 °C and pH 7.3.

XPS

Figure S3 shows the ratio of protein-related peaks to the total carbon of the C 1s XPS spectrum. Both the MES and the proteins adsorb on the surface and contribute to high ratio values. It is not clear whether there is any difference for adsorbed species inside and outside of the wear track.

Figure S4 shows the atomic ratio of organic nitrogen to protein-related carbon peaks. It should be 0.48 theoretically for BSA and higher for Fbn.[4] Here, it is lower in both cases, indicative of the presence of adventitious carbon. There is no clear difference for the solutions containing MES or proteins.

Figure S5 shows the speciation (different components) of the O 1s peak. It can be seen that the presence of proteins increases the signal of oxygen related to organic compounds, both within and outside of the wear track.

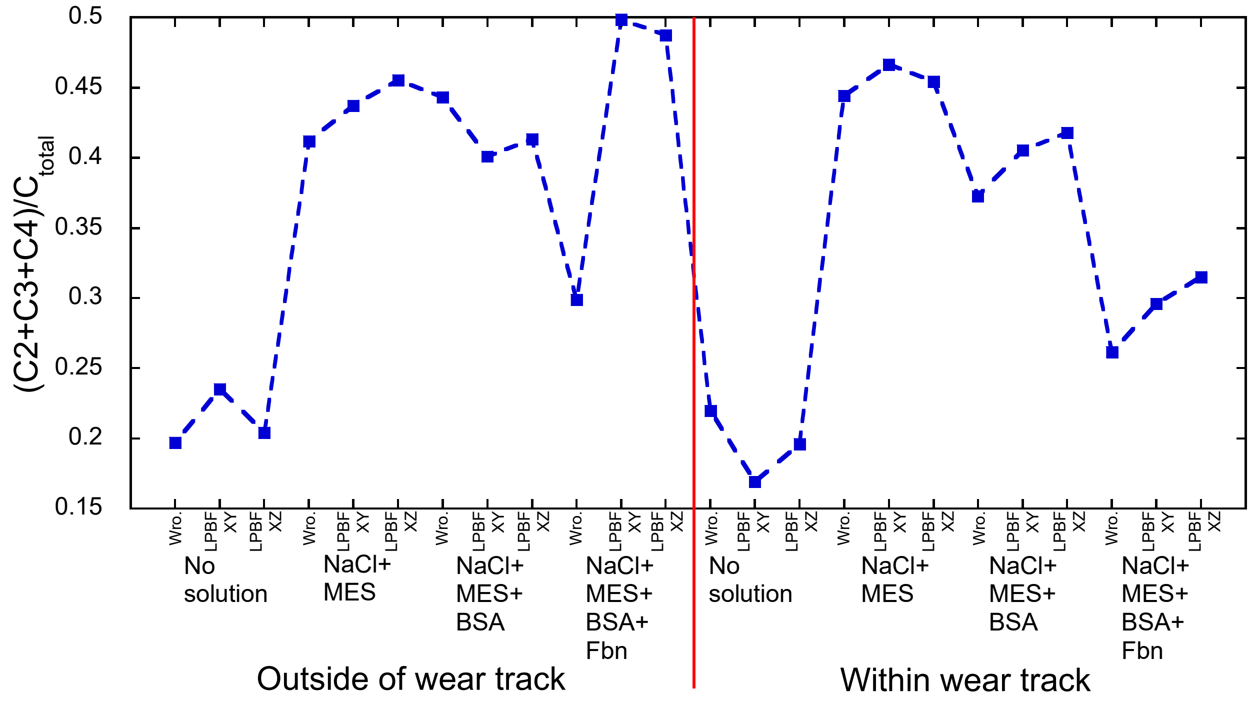

Figure S3. Atomic ratio of peaks at 286–289 eV (denoted C2+C3+C4) over total C 1s peak for wrought, LPBF-XY, and LPBF-XZ CoCrMo. Outside and within wear track: 1 h no sliding, followed by 1 h reciprocal linear sliding at 3 N load, followed by 0.5 h no sliding, at 37 °C at pH 7.3, either in no solution, NaCl+MES, NaCl+MES+BSA, or NaCl+MES+BSA+Fbn.

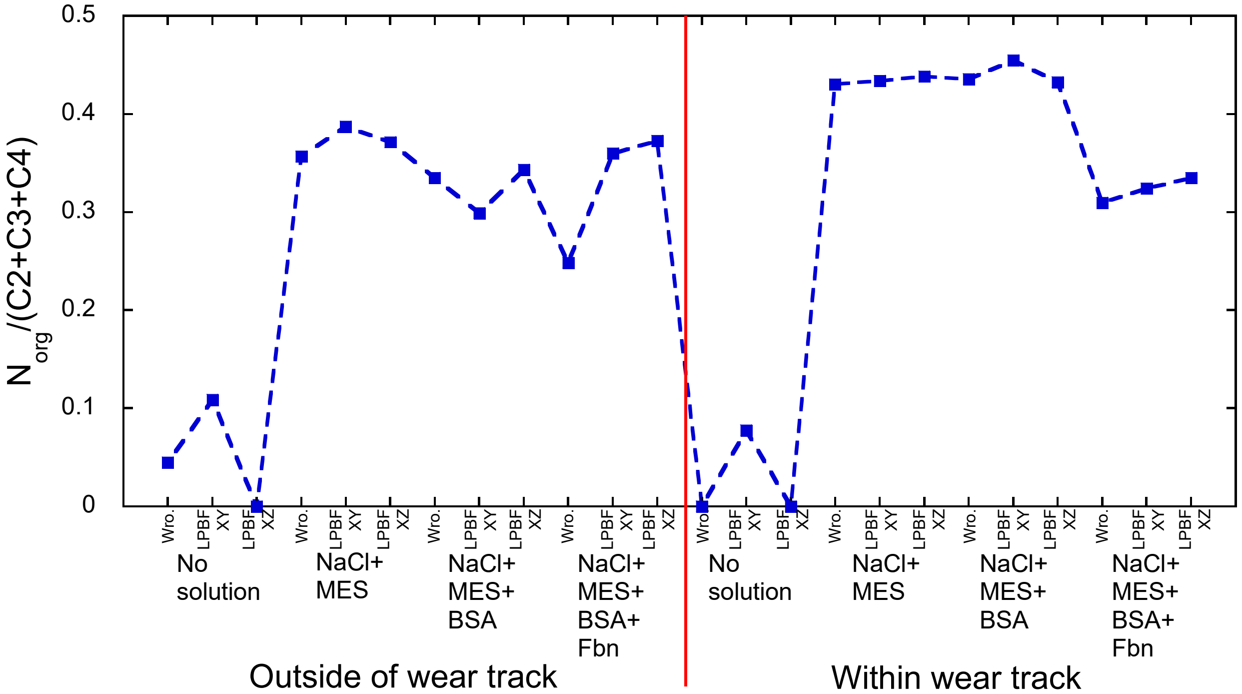

Figure S4. Atomic ratio of organic nitrogen (N 1s at 400 eV) to C2+C3+C4 for wrought, LPBF-XY, and LPBF-XZ CoCrMo. Outside and within wear track: 1 h no sliding, followed by 1 h reciprocal linear sliding at 3 N load, followed by 0.5 h no sliding, at 37 °C at pH 7.3, either in no solution, NaCl+MES, NaCl+MES+BSA, or NaCl+MES+BSA+Fbn.

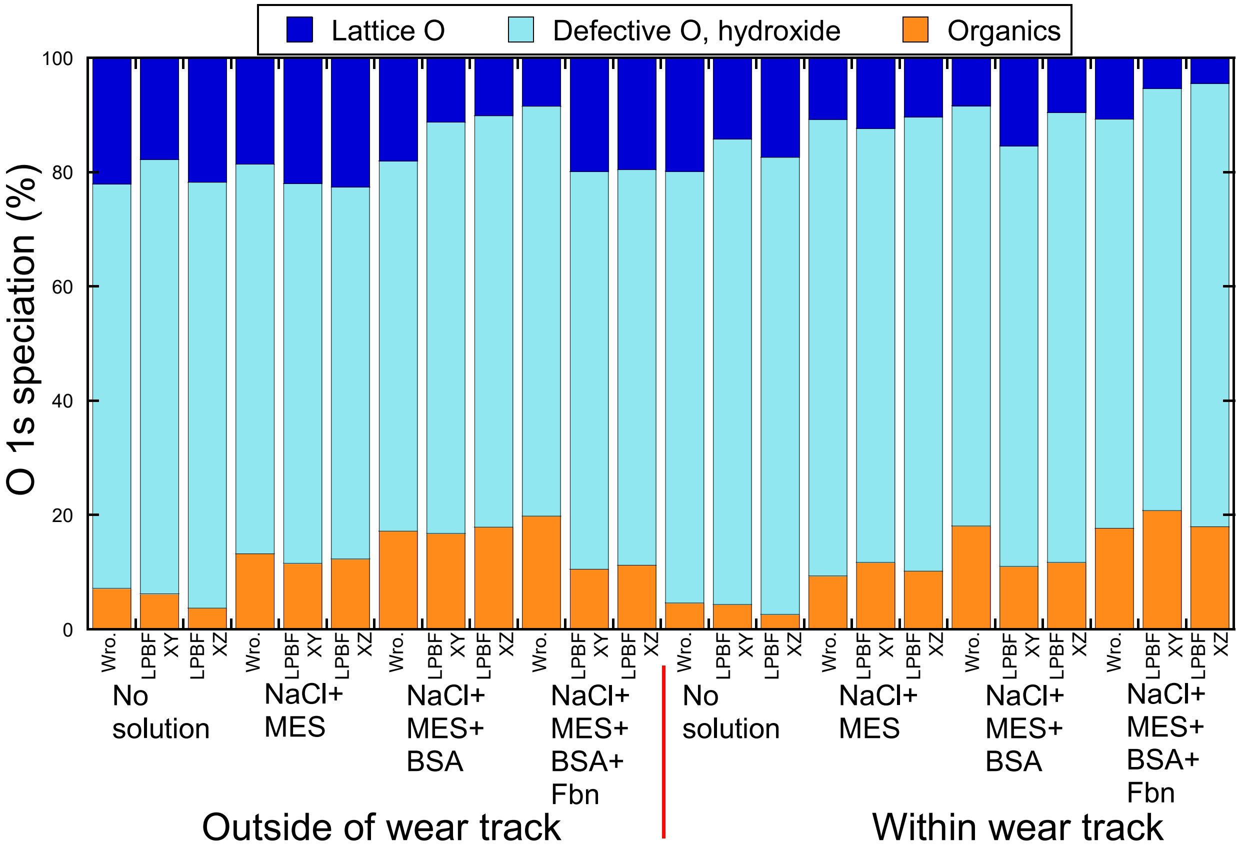

Figure S5. Speciation of O 1s peak (lattice oxygen, defective oxygen and hydroxide, and organics) for wrought, LPBF-XY, and LPBF-XZ CoCrMo. Outside and within wear track: 1 h no sliding, followed by 1 h reciprocal linear sliding at 3 N load, followed by 0.5 h no sliding, at 37 °C at pH 7.3, either in no solution, NaCl+MES, NaCl+MES+BSA, or NaCl+MES+BSA+Fbn.

Raw data of XPS

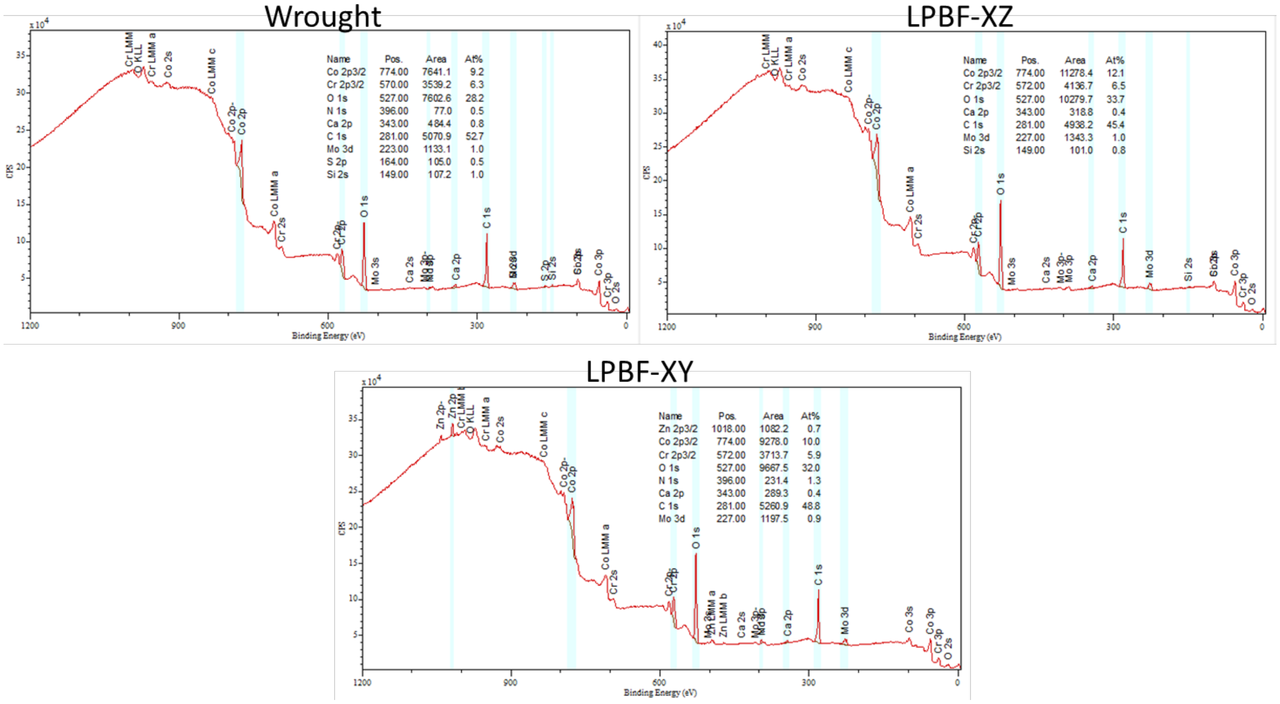
Wrought

Name	Pos.	Area	At%
Co 2p3/2	774.00	7641.1	9.2
Cr 2p3/2	570.00	3539.2	6.3
O 1s	527.00	7602.6	28.2
N 1s	396.00	77.0	0.5
Ca 2p	343.00	484.4	0.8
C 1s	281.00	5070.9	52.7
Mo 3d	223.00	1133.1	1.0
S 2p	164.00	105.0	0.5
Si 2s	149.00	107.2	1.0

LPBF-XZ

Name	Pos.	Area	At%
Co 2p3/2	774.00	11278.4	12.1
Cr 2p3/2	572.00	4136.7	6.5
O 1s	527.00	10279.7	33.7
Ca 2p	343.00	318.8	0.4
C 1s	281.00	4938.2	45.4
Mo 3d	227.00	1343.3	1.0
Si 2s	149.00	101.0	0.8

LPBF-XY

Name	Pos.	Area	At%
Zn 2p3/2	1018.00	1082.2	0.7
Co 2p3/2	774.00	9278.0	10.0
Cr 2p3/2	572.00	3713.7	5.9
O 1s	527.00	9667.5	32.0
N 1s	396.00	231.4	1.3
Ca 2p	343.00	289.3	0.4
C 1s	281.00	5260.9	48.8
Mo 3d	227.00	1197.5	0.9

Figure S6. Wide spectra of wrought, LPBF-XZ, and LPF-XY CoCrMo outside of the wear track, after tribocorrosion exposure 1 h no sliding, followed by 1 h reciprocal linear sliding at 3 N load, followed by 0.5 h no sliding, at 37 °C, in no solution (as a reference).

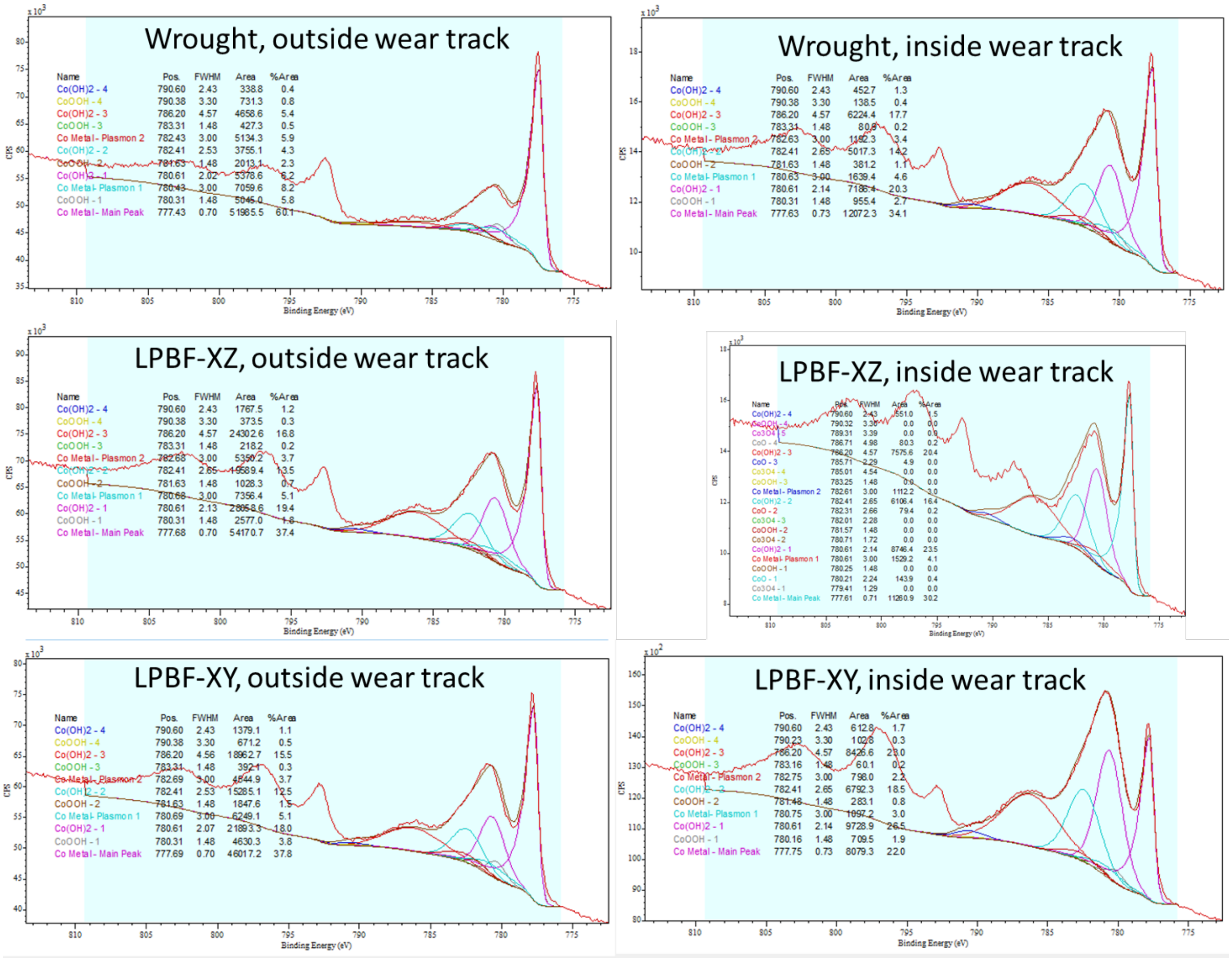

Wrought, outside wear track

Name	Pos.	FWHM	Area	%Area
Co(OH)2 - 4	790.60	2.43	338.8	0.4
CoOOH - 4	790.38	3.30	731.3	0.8
Co(OH)2 - 3	786.20	4.57	4658.6	5.4
CoOOH - 3	783.31	1.48	427.3	0.5
Co Metal - Plasmon 2	782.43	3.00	5134.3	5.9
Co(OH)2 - 2	782.41	2.53	3755.1	4.3
CoOOH - 2	781.63	1.48	2013.1	2.3
Co(OH)2 - 1	780.61	2.02	5378.6	6.2
Co Metal- Plasmon 1	780.43	3.00	7059.6	8.2
CoOOH - 1	780.31	1.48	5045.0	5.8
Co Metal - Main Peak	777.43	0.70	51985.5	60.1

Wrought, inside wear track

Name	Pos.	FWHM	Area	%Area
Co(OH)2 - 4	790.60	2.43	452.7	1.3
CoOOH - 4	790.38	3.30	138.5	0.4
Co(OH)2 - 3	786.20	4.57	6224.4	17.7
CoOOH - 3	783.31	1.48	80.8	0.2
Co Metal - Plasmon 2	782.63	3.00	1192.3	3.4
Co(OH)2 - 2	782.41	2.65	5017.3	14.2
CoOOH - 2	781.63	1.48	381.2	1.1
Co Metal- Plasmon 1	780.63	3.00	1639.4	4.6
Co(OH)2 - 1	780.61	2.14	7186.4	20.3
CoOOH - 1	780.31	1.48	955.4	2.7
Co Metal - Main Peak	777.63	0.73	12072.3	34.1

LPBF-XZ, outside wear track

Name	Pos.	FWHM	Area	%Area
Co(OH)2 - 4	790.60	2.43	1767.5	1.2
CoOOH - 4	790.38	3.30	373.5	0.3
Co(OH)2 - 3	786.20	4.57	24302.6	16.8
CoOOH - 3	783.31	1.48	218.2	0.2
Co Metal - Plasmon 2	782.68	3.00	5350.2	3.7
Co(OH)2 - 2	782.41	2.65	19589.4	13.5
CoOOH - 2	781.63	1.48	1028.3	0.7
Co Metal- Plasmon 1	780.68	3.00	7356.4	5.1
Co(OH)2 - 1	780.61	2.13	28058.6	19.4
CoOOH - 1	780.31	1.48	2577.0	1.8
Co Metal - Main Peak	777.68	0.70	54170.7	37.4

LPBF-XZ, inside wear track

Name	Pos.	FWHM	Area	%Area
Co(OH)2 - 4	790.60	2.43	551.0	1.5
CoOOH - 4	790.32	3.30	0.0	0.0
Co3O4 - 5	789.31	3.39	0.0	0.0
CoO - 4	786.71	4.98	80.3	0.2
Co(OH)2 - 3	786.20	4.57	7575.6	20.4
CoO - 3	785.71	2.29	4.9	0.0
Co3O4 - 4	785.01	4.54	0.0	0.0
CoOOH - 3	783.25	1.48	0.0	0.0
Co Metal - Plasmon 2	782.61	3.00	1112.2	3.0
Co(OH)2 - 2	782.41	2.65	6106.4	16.4
CoO - 2	782.31	2.66	79.4	0.2
Co3O4 - 3	782.01	2.28	0.0	0.0
CoOOH - 2	781.57	1.48	0.0	0.0
Co3O4 - 2	780.71	1.72	0.0	0.0
Co(OH)2 - 1	780.61	2.14	8746.4	23.5
Co Metal- Plasmon 1	780.61	3.00	1529.2	4.1
CoOOH - 1	780.25	1.48	0.0	0.0
CoO - 1	780.21	2.24	143.9	0.4
Co3O4 - 1	779.41	1.29	0.0	0.0
Co Metal - Main Peak	777.61	0.71	11260.9	30.2

LPBF-XY, outside wear track

Name	Pos.	FWHM	Area	%Area
Co(OH)2 - 4	790.60	2.43	1379.1	1.1
CoOOH - 4	790.38	3.30	671.2	0.5
Co(OH)2 - 3	786.20	4.56	18962.7	15.5
CoOOH - 3	783.31	1.48	392.1	0.3
Co Metal - Plasmon 2	782.69	3.00	4544.9	3.7
Co(OH)2 - 2	782.41	2.53	15285.1	12.5
CoOOH - 2	781.63	1.48	1847.6	1.5
Co Metal- Plasmon 1	780.69	3.00	6249.1	5.1
Co(OH)2 - 1	780.61	2.07	21893.3	18.0
CoOOH - 1	780.31	1.48	4630.3	3.8
Co Metal - Main Peak	777.69	0.70	46017.2	37.8

LPBF-XY, inside wear track

Name	Pos.	FWHM	Area	%Area
Co(OH)2 - 4	790.60	2.43	612.8	1.7
CoOOH - 4	790.23	3.30	102.8	0.3
Co(OH)2 - 3	786.20	4.57	8426.6	23.0
CoOOH - 3	783.16	1.48	60.1	0.2
Co Metal - Plasmon 2	782.75	3.00	798.0	2.2
Co(OH)2 - 2	782.41	2.65	6792.3	18.5
CoOOH - 2	781.48	1.48	283.1	0.8
Co Metal- Plasmon 1	780.75	3.00	1097.2	3.0
Co(OH)2 - 1	780.61	2.14	9728.9	26.5
CoOOH - 1	780.16	1.48	709.5	1.9
Co Metal - Main Peak	777.75	0.73	8079.3	22.0

Figure S7. Co 2p high-resolution spectra of wrought, LPBF-XZ, and LPF-XY CoCrMo outside (left) and inside (right) of the wear track, after tribocorrosion exposure 1 h no sliding, followed by 1 h reciprocal linear sliding at 3 N load, followed by 0.5 h no sliding, at 37 °C, in no solution (as a reference).

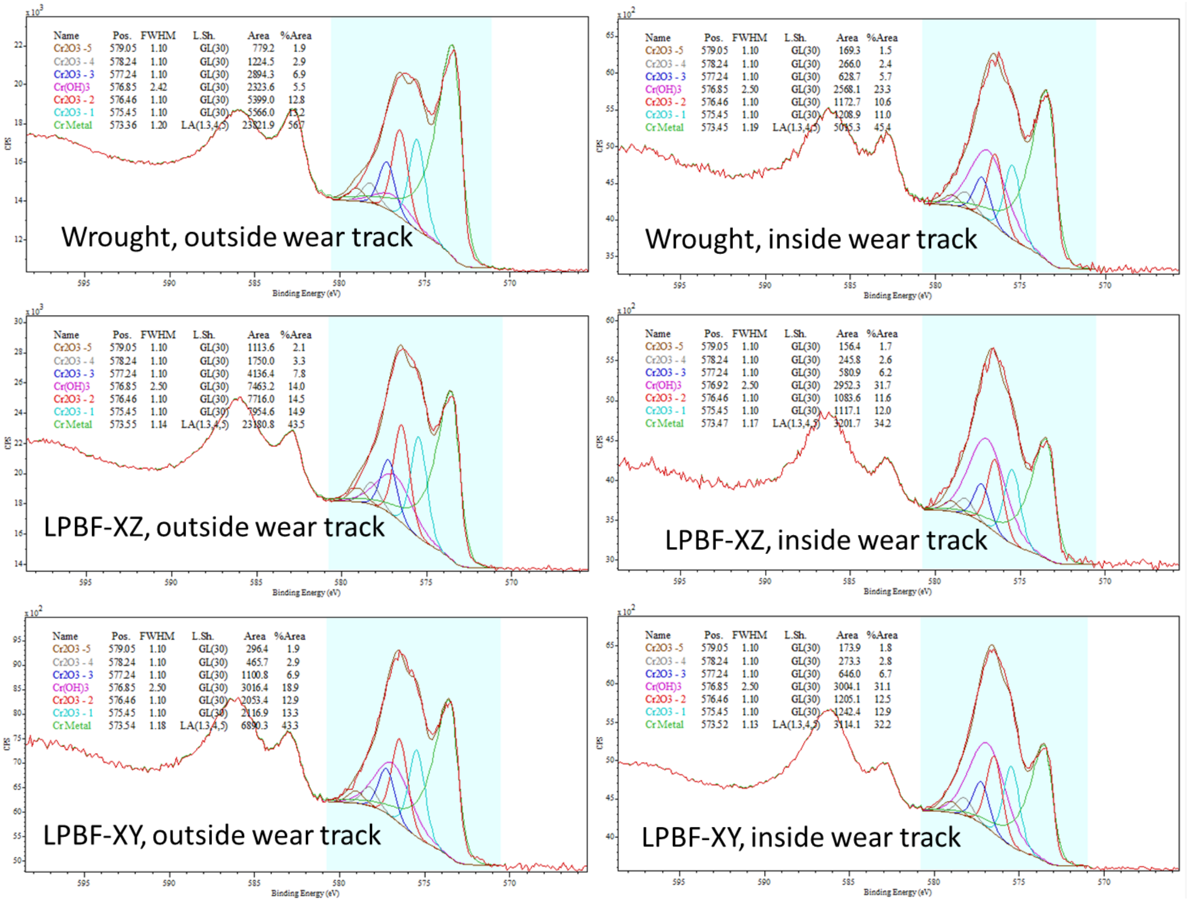

Wrought, outside wear track

Name	Pos.	FWHM	L.Sh.	Area	%Area
Cr2O3 -5	579.05	1.10	GL(30)	779.2	1.9
Cr2O3 - 4	578.24	1.10	GL(30)	1224.5	2.9
Cr2O3 - 3	577.24	1.10	GL(30)	2894.3	6.9
Cr(OH)3	576.85	2.42	GL(30)	2323.6	5.5
Cr2O3 - 2	576.46	1.10	GL(30)	5399.0	12.8
Cr2O3 - 1	575.45	1.10	GL(30)	5566.0	13.2
Cr Metal	573.36	1.20	LA(1.3,4,5)	23821.9	56.7

Wrought, inside wear track

Name	Pos.	FWHM	L.Sh.	Area	%Area
Cr2O3 -5	579.05	1.10	GL(30)	169.3	1.5
Cr2O3 - 4	578.24	1.10	GL(30)	266.0	2.4
Cr2O3 - 3	577.24	1.10	GL(30)	628.7	5.7
Cr(OH)3	576.85	2.50	GL(30)	2568.1	23.3
Cr2O3 - 2	576.46	1.10	GL(30)	1172.7	10.6
Cr2O3 - 1	575.45	1.10	GL(30)	1208.9	11.0
Cr Metal	573.45	1.19	LA(1.3,4,5)	5015.3	45.4

LPBF-XZ, outside wear track

Name	Pos.	FWHM	L.Sh.	Area	%Area
Cr2O3 -5	579.05	1.10	GL(30)	1113.6	2.1
Cr2O3 - 4	578.24	1.10	GL(30)	1750.0	3.3
Cr2O3 - 3	577.24	1.10	GL(30)	4136.4	7.8
Cr(OH)3	576.85	2.50	GL(30)	7463.2	14.0
Cr2O3 - 2	576.46	1.10	GL(30)	7716.0	14.5
Cr2O3 - 1	575.45	1.10	GL(30)	7954.6	14.9
Cr Metal	573.55	1.14	LA(1.3,4,5)	23180.8	43.5

LPBF-XZ, inside wear track

Name	Pos.	FWHM	L.Sh.	Area	%Area
Cr2O3 -5	579.05	1.10	GL(30)	156.4	1.7
Cr2O3 - 4	578.24	1.10	GL(30)	245.8	2.6
Cr2O3 - 3	577.24	1.10	GL(30)	580.9	6.2
Cr(OH)3	576.92	2.50	GL(30)	2952.3	31.7
Cr2O3 - 2	576.46	1.10	GL(30)	1083.6	11.6
Cr2O3 - 1	575.45	1.10	GL(30)	1117.1	12.0
Cr Metal	573.47	1.17	LA(1.3,4,5)	3201.7	34.2

LPBF-XY, outside wear track

Name	Pos.	FWHM	L.Sh.	Area	%Area
Cr2O3 -5	579.05	1.10	GL(30)	296.4	1.9
Cr2O3 - 4	578.24	1.10	GL(30)	465.7	2.9
Cr2O3 - 3	577.24	1.10	GL(30)	1100.8	6.9
Cr(OH)3	576.85	2.50	GL(30)	3016.4	18.9
Cr2O3 - 2	576.46	1.10	GL(30)	2053.4	12.9
Cr2O3 - 1	575.45	1.10	GL(30)	2116.9	13.3
Cr Metal	573.54	1.18	LA(1.3,4,5)	6890.3	43.3

LPBF-XY, inside wear track

Name	Pos.	FWHM	L.Sh.	Area	%Area
Cr2O3 -5	579.05	1.10	GL(30)	173.9	1.8
Cr2O3 - 4	578.24	1.10	GL(30)	273.3	2.8
Cr2O3 - 3	577.24	1.10	GL(30)	646.0	6.7
Cr(OH)3	576.85	2.50	GL(30)	3004.1	31.1
Cr2O3 - 2	576.46	1.10	GL(30)	1205.1	12.5
Cr2O3 - 1	575.45	1.10	GL(30)	1242.4	12.9
Cr Metal	573.52	1.13	LA(1.3,4,5)	3114.1	32.2

Figure S8. Cr 2p high-resolution spectra of wrought, LPBF-XZ, and LPF-XY CoCrMo outside (left) and inside (right) of the wear track, after tribocorrosion exposure 1 h no sliding, followed by 1 h reciprocal linear sliding at 3 N load, followed by 0.5 h no sliding, at 37 °C, in no solution (as a reference).

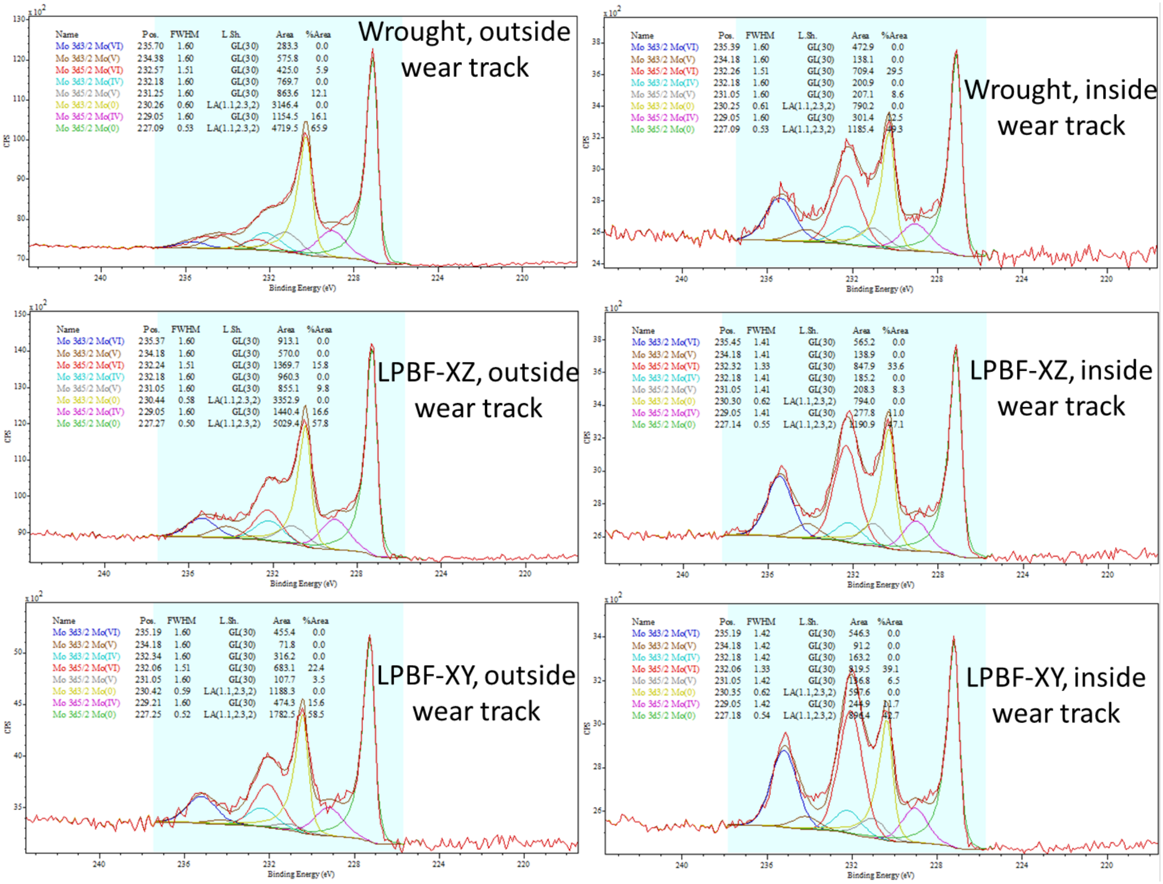

Name	Pos.	FWHM	L.Sh.	Area	%Area
Mo 3d3/2 Mo(VI)	235.70	1.60	GL(30)	283.3	0.0
Mo 3d3/2 Mo(V)	234.38	1.60	GL(30)	575.8	0.0
Mo 3d5/2 Mo(VI)	232.57	1.51	GL(30)	425.0	5.9
Mo 3d3/2 Mo(IV)	232.18	1.60	GL(30)	769.7	0.0
Mo 3d5/2 Mo(V)	231.25	1.60	GL(30)	863.6	12.1
Mo 3d3/2 Mo(0)	230.26	0.60	LA(1.1,2.3,2)	3146.4	0.0
Mo 3d5/2 Mo(IV)	229.05	1.60	GL(30)	1154.5	16.1
Mo 3d5/2 Mo(0)	227.09	0.53	LA(1.1,2.3,2)	4719.5	65.9

Name	Pos.	FWHM	L.Sh.	Area	%Area
Mo 3d3/2 Mo(VI)	235.39	1.60	GL(30)	472.9	0.0
Mo 3d3/2 Mo(V)	234.18	1.60	GL(30)	138.1	0.0
Mo 3d5/2 Mo(VI)	232.26	1.51	GL(30)	709.4	29.5
Mo 3d3/2 Mo(IV)	232.18	1.60	GL(30)	200.9	0.0
Mo 3d5/2 Mo(V)	231.05	1.60	GL(30)	207.1	8.6
Mo 3d3/2 Mo(0)	230.25	0.61	LA(1.1,2.3,2)	790.2	0.0
Mo 3d5/2 Mo(IV)	229.05	1.60	GL(30)	301.4	12.5
Mo 3d5/2 Mo(0)	227.09	0.53	LA(1.1,2.3,2)	1185.4	49.3

Name	Pos.	FWHM	L.Sh.	Area	%Area
Mo 3d3/2 Mo(VI)	235.37	1.60	GL(30)	913.1	0.0
Mo 3d3/2 Mo(V)	234.18	1.60	GL(30)	570.0	0.0
Mo 3d5/2 Mo(VI)	232.24	1.51	GL(30)	1369.7	15.8
Mo 3d3/2 Mo(IV)	232.18	1.60	GL(30)	960.3	0.0
Mo 3d5/2 Mo(V)	231.05	1.60	GL(30)	855.1	9.8
Mo 3d3/2 Mo(0)	230.44	0.58	LA(1.1,2.3,2)	3352.9	0.0
Mo 3d5/2 Mo(IV)	229.05	1.60	GL(30)	1440.4	16.6
Mo 3d5/2 Mo(0)	227.27	0.50	LA(1.1,2.3,2)	5029.4	57.8

Name	Pos.	FWHM	L.Sh.	Area	%Area
Mo 3d3/2 Mo(VI)	235.45	1.41	GL(30)	565.2	0.0
Mo 3d3/2 Mo(V)	234.18	1.41	GL(30)	138.9	0.0
Mo 3d5/2 Mo(VI)	232.32	1.33	GL(30)	847.9	33.6
Mo 3d3/2 Mo(IV)	232.18	1.41	GL(30)	185.2	0.0
Mo 3d5/2 Mo(V)	231.05	1.41	GL(30)	208.3	8.3
Mo 3d3/2 Mo(0)	230.30	0.62	LA(1.1,2.3,2)	794.0	0.0
Mo 3d5/2 Mo(IV)	229.05	1.41	GL(30)	277.8	11.0
Mo 3d5/2 Mo(0)	227.14	0.55	LA(1.1,2.3,2)	1190.9	47.1

Name	Pos.	FWHM	L.Sh.	Area	%Area
Mo 3d3/2 Mo(VI)	235.19	1.60	GL(30)	455.4	0.0
Mo 3d3/2 Mo(V)	234.18	1.60	GL(30)	71.8	0.0
Mo 3d3/2 Mo(IV)	232.34	1.60	GL(30)	316.2	0.0
Mo 3d5/2 Mo(VI)	232.06	1.51	GL(30)	683.1	22.4
Mo 3d5/2 Mo(V)	231.05	1.60	GL(30)	107.7	3.5
Mo 3d3/2 Mo(0)	230.42	0.59	LA(1.1,2.3,2)	1188.3	0.0
Mo 3d5/2 Mo(IV)	229.21	1.60	GL(30)	474.3	15.6
Mo 3d5/2 Mo(0)	227.25	0.52	LA(1.1,2.3,2)	1782.5	58.5

Name	Pos.	FWHM	L.Sh.	Area	%Area
Mo 3d3/2 Mo(VI)	235.19	1.42	GL(30)	546.3	0.0
Mo 3d3/2 Mo(V)	234.18	1.42	GL(30)	91.2	0.0
Mo 3d3/2 Mo(IV)	232.18	1.42	GL(30)	163.2	0.0
Mo 3d5/2 Mo(VI)	232.06	1.33	GL(30)	819.5	39.1
Mo 3d5/2 Mo(V)	231.05	1.42	GL(30)	136.8	6.5
Mo 3d3/2 Mo(0)	230.35	0.62	LA(1.1,2.3,2)	597.6	0.0
Mo 3d5/2 Mo(IV)	229.05	1.42	GL(30)	244.9	11.7
Mo 3d5/2 Mo(0)	227.18	0.54	LA(1.1,2.3,2)	896.4	42.7

Figure S9. Mo 3d high-resolution spectra of wrought, LPBF-XZ, and LPF-XY CoCrMo outside (left) and inside (right) of the wear track, after tribocorrosion exposure 1 h no sliding, followed by 1 h reciprocal linear sliding at 3 N load, followed by 0.5 h no sliding, at 37 °C, in no solution (as a reference).

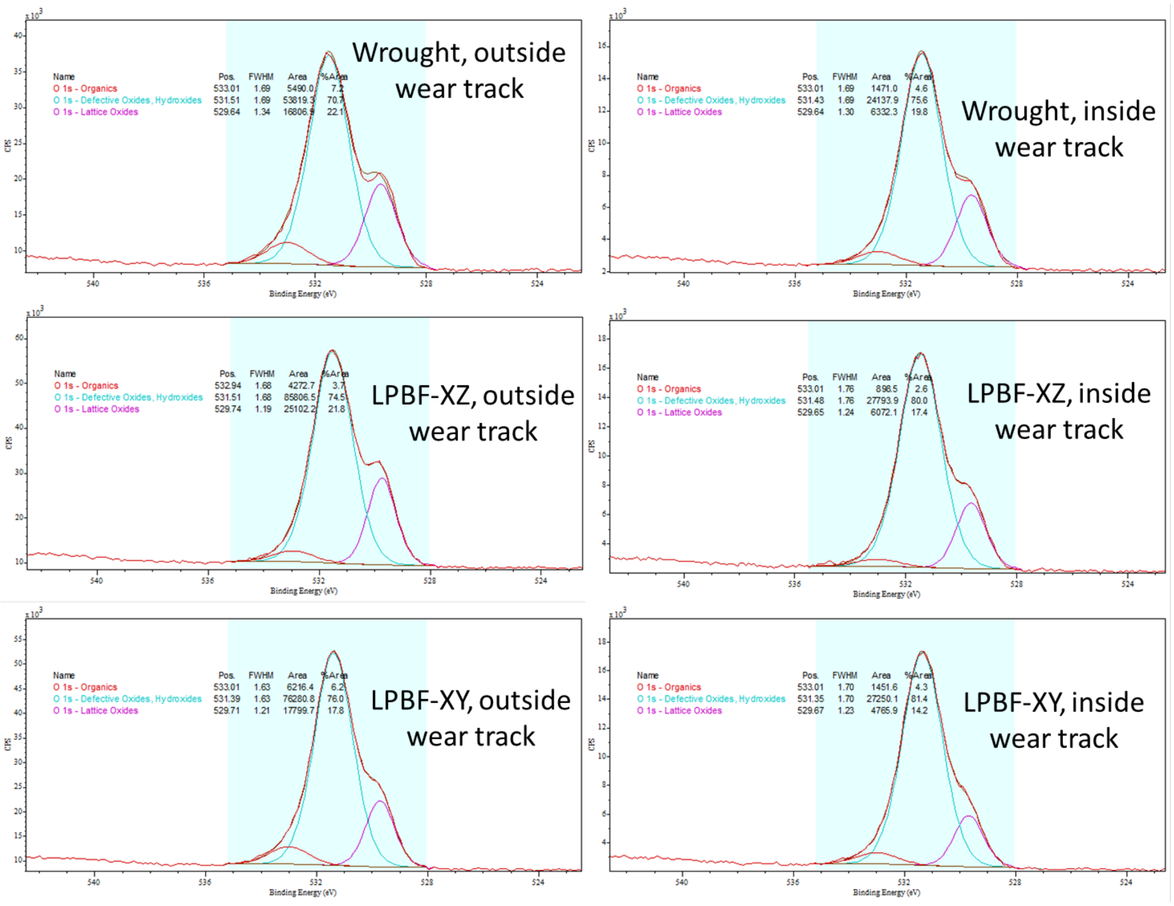

Figure S10. O 1s high-resolution spectra of wrought, LPBF-XZ, and LPF-XY CoCrMo outside (left) and inside (right) of the wear track, after tribocorrosion exposure 1 h no sliding, followed by 1 h reciprocal linear sliding at 3 N load, followed by 0.5 h no sliding, at 37 °C, in no solution (as a reference).

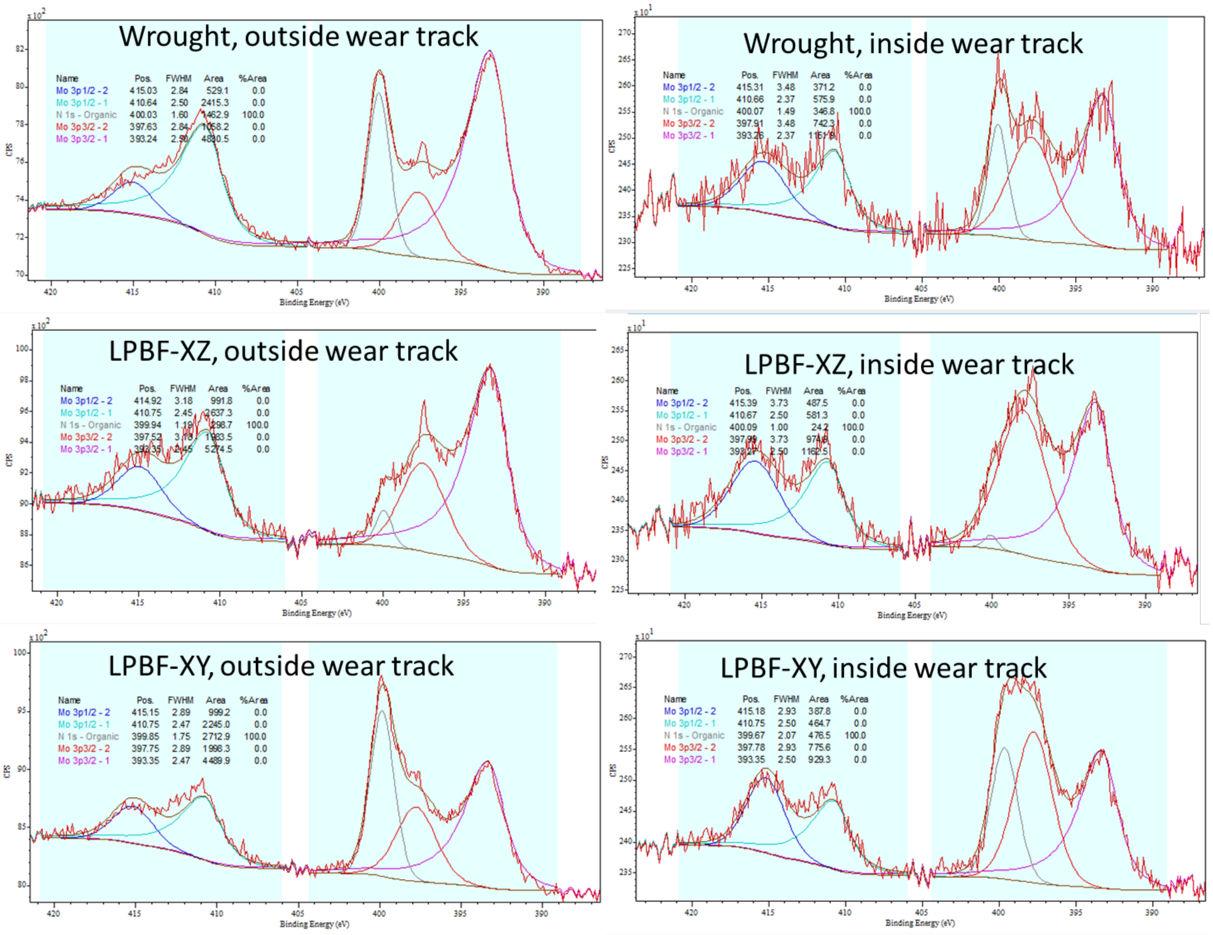

Wrought, outside wear track

Name	Pos.	FWHM	Area	%Area
Mo 3p1/2 - 2	415.03	2.84	529.1	0.0
Mo 3p1/2 - 1	410.64	2.50	2415.3	0.0
N 1s - Organic	400.03	1.60	1462.9	100.0
Mo 3p3/2 - 2	397.63	2.84	1058.2	0.0
Mo 3p3/2 - 1	393.24	2.50	4830.5	0.0

Wrought, inside wear track

Name	Pos.	FWHM	Area	%Area
Mo 3p1/2 - 2	415.31	3.48	371.2	0.0
Mo 3p1/2 - 1	410.66	2.37	575.9	0.0
N 1s - Organic	400.07	1.49	346.8	100.0
Mo 3p3/2 - 2	397.91	3.48	742.3	0.0
Mo 3p3/2 - 1	393.26	2.37	1151.9	0.0

LPBF-XZ, outside wear track

Name	Pos.	FWHM	Area	%Area
Mo 3p1/2 - 2	414.92	3.18	991.8	0.0
Mo 3p1/2 - 1	410.75	2.45	2637.3	0.0
N 1s - Organic	399.94	1.19	298.7	100.0
Mo 3p3/2 - 2	397.52	3.18	1983.5	0.0
Mo 3p3/2 - 1	393.35	2.45	5274.5	0.0

LPBF-XZ, inside wear track

Name	Pos.	FWHM	Area	%Area
Mo 3p1/2 - 2	415.39	3.73	487.5	0.0
Mo 3p1/2 - 1	410.67	2.50	581.3	0.0
N 1s - Organic	400.09	1.00	24.2	100.0
Mo 3p3/2 - 2	397.99	3.73	974.9	0.0
Mo 3p3/2 - 1	393.27	2.50	1162.5	0.0

LPBF-XY, outside wear track

Name	Pos.	FWHM	Area	%Area
Mo 3p1/2 - 2	415.15	2.89	999.2	0.0
Mo 3p1/2 - 1	410.75	2.47	2245.0	0.0
N 1s - Organic	399.85	1.75	2712.9	100.0
Mo 3p3/2 - 2	397.75	2.89	1998.3	0.0
Mo 3p3/2 - 1	393.35	2.47	4489.9	0.0

LPBF-XY, inside wear track

Name	Pos.	FWHM	Area	%Area
Mo 3p1/2 - 2	415.18	2.93	387.8	0.0
Mo 3p1/2 - 1	410.75	2.50	464.7	0.0
N 1s - Organic	399.67	2.07	476.5	100.0
Mo 3p3/2 - 2	397.78	2.93	775.6	0.0
Mo 3p3/2 - 1	393.35	2.50	929.3	0.0

Figure S11. N 1s high-resolution spectra of wrought, LPBF-XZ, and LPF-XY CoCrMo outside (left) and inside (right) of the wear track, after tribocorrosion exposure 1 h no sliding, followed by 1 h reciprocal linear sliding at 3 N load, followed by 0.5 h no sliding, at 37 °C, in no solution (as a reference). The overlap with the Mo 3p peak is accounted for.

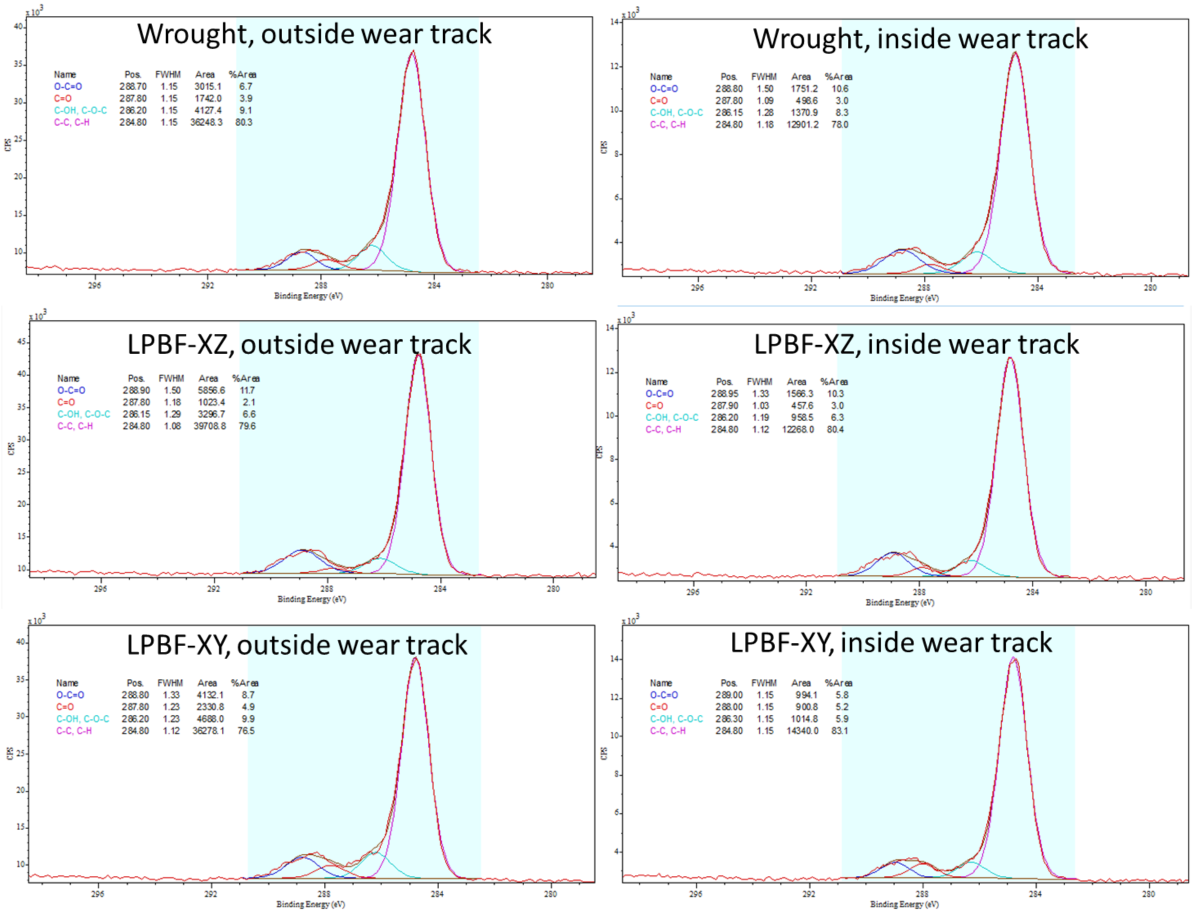

Wrought, outside wear track

Name	Pos.	FWHM	Area	%Area
O-C=O	288.70	1.15	3015.1	6.7
C=O	287.80	1.15	1742.0	3.9
C-OH, C-O-C	286.20	1.15	4127.4	9.1
C-C, C-H	284.80	1.15	36248.3	80.3

Wrought, inside wear track

Name	Pos.	FWHM	Area	%Area
O-C=O	288.80	1.50	1751.2	10.6
C=O	287.80	1.09	498.6	3.0
C-OH, C-O-C	286.15	1.28	1370.9	8.3
C-C, C-H	284.80	1.18	12901.2	78.0

LPBF-XZ, outside wear track

Name	Pos.	FWHM	Area	%Area
O-C=O	288.90	1.50	5856.6	11.7
C=O	287.80	1.18	1023.4	2.1
C-OH, C-O-C	286.15	1.29	3296.7	6.6
C-C, C-H	284.80	1.08	39708.8	79.6

LPBF-XZ, inside wear track

Name	Pos.	FWHM	Area	%Area
O-C=O	288.95	1.33	1566.3	10.3
C=O	287.90	1.03	457.6	3.0
C-OH, C-O-C	286.20	1.19	958.5	6.3
C-C, C-H	284.80	1.12	12268.0	80.4

LPBF-XY, outside wear track

Name	Pos.	FWHM	Area	%Area
O-C=O	288.80	1.33	4132.1	8.7
C=O	287.80	1.23	2330.8	4.9
C-OH, C-O-C	286.20	1.23	4688.0	9.9
C-C, C-H	284.80	1.12	36278.1	76.5

LPBF-XY, inside wear track

Name	Pos.	FWHM	Area	%Area
O-C=O	289.00	1.15	994.1	5.8
C=O	288.00	1.15	900.8	5.2
C-OH, C-O-C	286.30	1.15	1014.8	5.9
C-C, C-H	284.80	1.15	14340.0	83.1

Figure S12. C 1s high-resolution spectra of wrought, LPBF-XZ, and LPF-XY CoCrMo outside (left) and inside (right) of the wear track, after tribocorrosion exposure 1 h no sliding, followed by 1 h reciprocal linear sliding at 3 N load, followed by 0.5 h no sliding, at 37 °C, in no solution (as a reference).

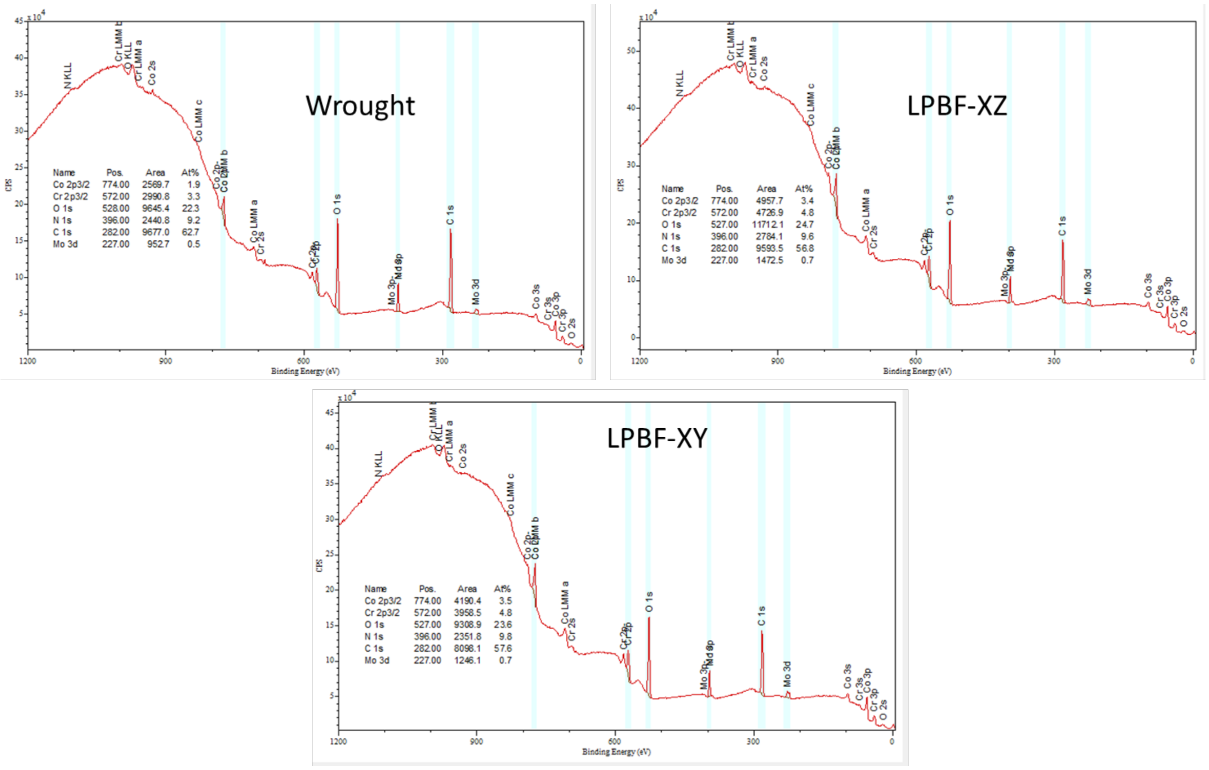

Name	Pos.	Area	At%
Co 2p3/2	774.00	2569.7	1.9
Cr 2p3/2	572.00	2990.8	3.3
O 1s	528.00	9645.4	22.3
N 1s	396.00	2440.8	9.2
C 1s	282.00	9677.0	62.7
Mo 3d	227.00	952.7	0.5

Name	Pos.	Area	At%
Co 2p3/2	774.00	4957.7	3.4
Cr 2p3/2	572.00	4726.9	4.8
O 1s	527.00	11712.1	24.7
N 1s	396.00	2784.1	9.6
C 1s	282.00	9593.5	56.8
Mo 3d	227.00	1472.5	0.7

Name	Pos.	Area	At%
Co 2p3/2	774.00	4190.4	3.5
Cr 2p3/2	572.00	3958.5	4.8
O 1s	527.00	9308.9	23.6
N 1s	396.00	2351.8	9.8
C 1s	282.00	8098.1	57.6
Mo 3d	227.00	1246.1	0.7

Figure S13. Wide spectra of wrought, LPBF-XZ, and LPF-XY CoCrMo outside of the wear track, after tribocorrosion exposure 1 h no sliding, followed by 1 h reciprocal linear sliding at 3 N load, followed by 0.5 h no sliding, at 37 °C and at pH 7.3, in NaCl+MES.

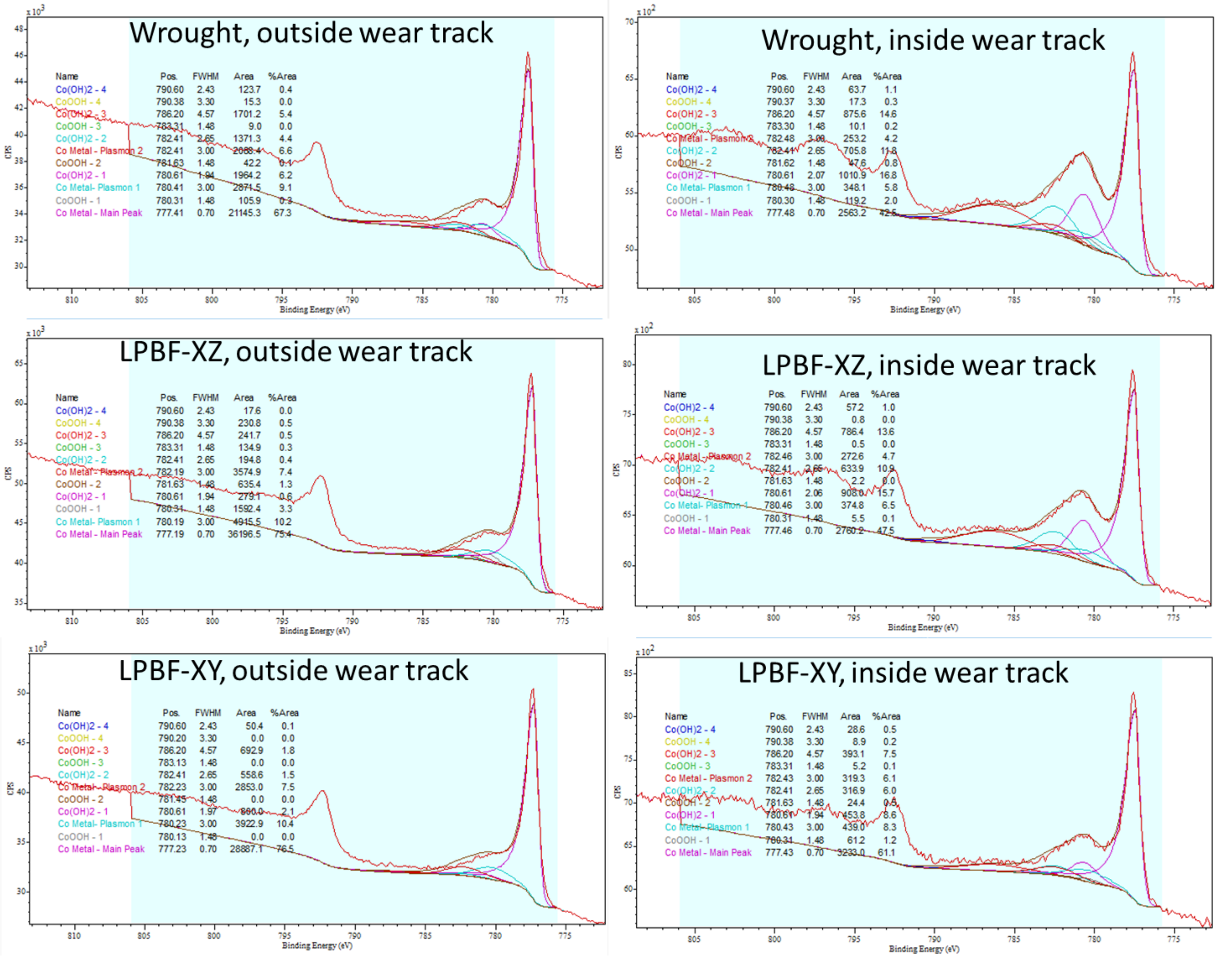

Wrought, outside wear track

Name	Pos.	FWHM	Area	%Area
Co(OH)2 - 4	790.60	2.43	123.7	0.4
CoOOH - 4	790.38	3.30	15.3	0.0
Co(OH)2 - 3	786.20	4.57	1701.2	5.4
CoOOH - 3	783.31	1.48	9.0	0.0
Co(OH)2 - 2	782.41	2.65	1371.3	4.4
Co Metal - Plasmon 2	782.41	3.00	2068.4	6.6
CoOOH - 2	781.63	1.48	42.2	0.1
Co(OH)2 - 1	780.61	1.94	1964.2	6.2
Co Metal- Plasmon 1	780.41	3.00	2871.5	9.1
CoOOH - 1	780.31	1.48	105.9	0.3
Co Metal - Main Peak	777.41	0.70	21145.3	67.3

Wrought, inside wear track

Name	Pos.	FWHM	Area	%Area
Co(OH)2 - 4	790.60	2.43	63.7	1.1
CoOOH - 4	790.37	3.30	17.3	0.3
Co(OH)2 - 3	786.20	4.57	875.6	14.6
CoOOH - 3	783.30	1.48	10.1	0.2
Co Metal - Plasmon 2	782.48	3.00	253.2	4.2
Co(OH)2 - 2	782.41	2.65	705.8	11.8
CoOOH - 2	781.62	1.48	47.6	0.8
Co(OH)2 - 1	780.61	2.07	1010.9	16.8
Co Metal- Plasmon 1	780.48	3.00	348.1	5.8
CoOOH - 1	780.30	1.48	119.2	2.0
Co Metal - Main Peak	777.48	0.70	2563.2	42.5

LPBF-XZ, outside wear track

Name	Pos.	FWHM	Area	%Area
Co(OH)2 - 4	790.60	2.43	17.6	0.0
CoOOH - 4	790.38	3.30	230.8	0.5
Co(OH)2 - 3	786.20	4.57	241.7	0.5
CoOOH - 3	783.31	1.48	134.9	0.3
Co(OH)2 - 2	782.41	2.65	194.8	0.4
Co Metal - Plasmon 2	782.19	3.00	3574.9	7.4
CoOOH - 2	781.63	1.48	635.4	1.3
Co(OH)2 - 1	780.61	1.94	279.1	0.6
CoOOH - 1	780.31	1.48	1592.4	3.3
Co Metal- Plasmon 1	780.19	3.00	4915.5	10.2
Co Metal - Main Peak	777.19	0.70	36196.5	75.4

LPBF-XZ, inside wear track

Name	Pos.	FWHM	Area	%Area
Co(OH)2 - 4	790.60	2.43	57.2	1.0
CoOOH - 4	790.38	3.30	0.8	0.0
Co(OH)2 - 3	786.20	4.57	786.4	13.6
CoOOH - 3	783.31	1.48	0.5	0.0
Co Metal - Plasmon 2	782.46	3.00	272.6	4.7
Co(OH)2 - 2	782.41	2.65	633.9	10.9
CoOOH - 2	781.63	1.48	2.2	0.0
Co(OH)2 - 1	780.61	2.06	908.0	15.7
Co Metal- Plasmon 1	780.46	3.00	374.8	6.5
CoOOH - 1	780.31	1.48	5.5	0.1
Co Metal - Main Peak	777.46	0.70	2760.2	47.5

LPBF-XY, outside wear track

Name	Pos.	FWHM	Area	%Area
Co(OH)2 - 4	790.60	2.43	50.4	0.1
CoOOH - 4	790.20	3.30	0.0	0.0
Co(OH)2 - 3	786.20	4.57	692.9	1.8
CoOOH - 3	783.13	1.48	0.0	0.0
Co(OH)2 - 2	782.41	2.65	558.6	1.5
Co Metal - Plasmon 2	782.23	3.00	2853.0	7.5
CoOOH - 2	781.45	1.48	0.0	0.0
Co(OH)2 - 1	780.61	1.97	800.0	2.1
Co Metal- Plasmon 1	780.23	3.00	3922.9	10.4
CoOOH - 1	780.13	1.48	0.0	0.0
Co Metal - Main Peak	777.23	0.70	28887.1	76.5

LPBF-XY, inside wear track

Name	Pos.	FWHM	Area	%Area
Co(OH)2 - 4	790.60	2.43	28.6	0.5
CoOOH - 4	790.38	3.30	8.9	0.2
Co(OH)2 - 3	786.20	4.57	393.1	7.5
CoOOH - 3	783.31	1.48	5.2	0.1
Co Metal - Plasmon 2	782.43	3.00	319.3	6.1
Co(OH)2 - 2	782.41	2.65	316.9	6.0
CoOOH - 2	781.63	1.48	24.4	0.5
Co(OH)2 - 1	780.61	1.94	453.8	8.6
Co Metal- Plasmon 1	780.43	3.00	439.0	8.3
CoOOH - 1	780.31	1.48	61.2	1.2
Co Metal - Main Peak	777.43	0.70	3233.0	61.1

Figure S14. Co 2p high-resolution spectra of wrought, LPBF-XZ, and LPF-XY CoCrMo outside (left) and inside (right) of the wear track, after tribocorrosion exposure 1 h no sliding, followed by 1 h reciprocal linear sliding at 3 N load, followed by 0.5 h no sliding, at 37 °C and at pH 7.3, in NaCl+MES.

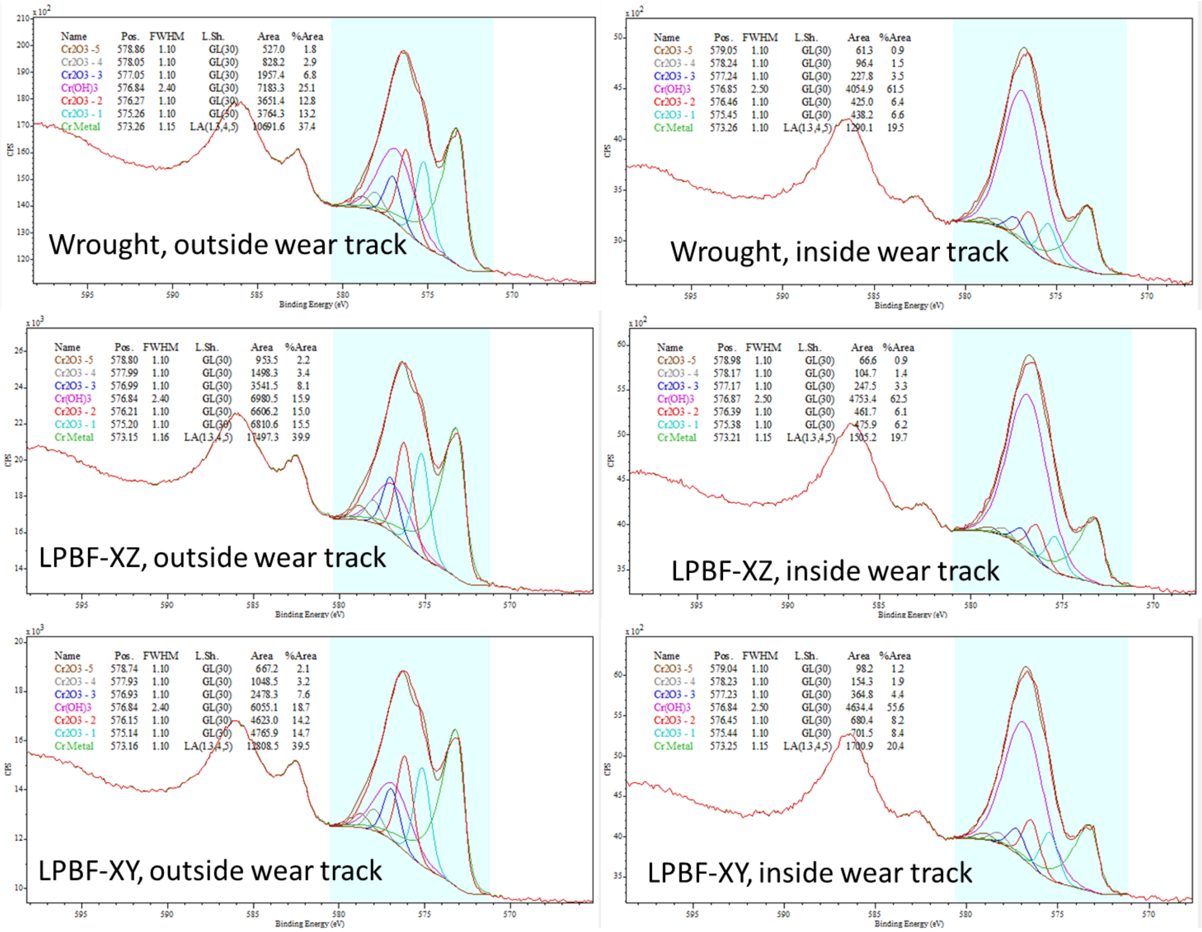

Wrought, outside wear track

Name	Pos.	FWHM	L.Sh.	Area	%Area
Cr2O3 -5	578.86	1.10	GL(30)	527.0	1.8
Cr2O3 - 4	578.05	1.10	GL(30)	828.2	2.9
Cr2O3 - 3	577.05	1.10	GL(30)	1957.4	6.8
Cr(OH)3	576.84	2.40	GL(30)	7183.3	25.1
Cr2O3 - 2	576.27	1.10	GL(30)	3651.4	12.8
Cr2O3 - 1	575.26	1.10	GL(30)	3764.3	13.2
Cr Metal	573.26	1.15	LA(1.3,4,5)	10691.6	37.4

Wrought, inside wear track

Name	Pos.	FWHM	L.Sh.	Area	%Area
Cr2O3 -5	579.05	1.10	GL(30)	61.3	0.9
Cr2O3 - 4	578.24	1.10	GL(30)	96.4	1.5
Cr2O3 - 3	577.24	1.10	GL(30)	227.8	3.5
Cr(OH)3	576.85	2.50	GL(30)	4054.9	61.5
Cr2O3 - 2	576.46	1.10	GL(30)	425.0	6.4
Cr2O3 - 1	575.45	1.10	GL(30)	438.2	6.6
Cr Metal	573.26	1.10	LA(1.3,4,5)	1290.1	19.5

LPBF-XZ, outside wear track

Name	Pos.	FWHM	L.Sh.	Area	%Area
Cr2O3 -5	578.80	1.10	GL(30)	953.5	2.2
Cr2O3 - 4	577.99	1.10	GL(30)	1498.3	3.4
Cr2O3 - 3	576.99	1.10	GL(30)	3541.5	8.1
Cr(OH)3	576.84	2.40	GL(30)	6980.5	15.9
Cr2O3 - 2	576.21	1.10	GL(30)	6606.2	15.0
Cr2O3 - 1	575.20	1.10	GL(30)	6810.6	15.5
Cr Metal	573.15	1.16	LA(1.3,4,5)	17497.3	39.9

LPBF-XZ, inside wear track

Name	Pos.	FWHM	L.Sh.	Area	%Area
Cr2O3 -5	578.98	1.10	GL(30)	66.6	0.9
Cr2O3 - 4	578.17	1.10	GL(30)	104.7	1.4
Cr2O3 - 3	577.17	1.10	GL(30)	247.5	3.3
Cr(OH)3	576.87	2.50	GL(30)	4753.4	62.5
Cr2O3 - 2	576.39	1.10	GL(30)	461.7	6.1
Cr2O3 - 1	575.38	1.10	GL(30)	475.9	6.2
Cr Metal	573.21	1.15	LA(1.3,4,5)	1505.2	19.7

LPBF-XY, outside wear track

Name	Pos.	FWHM	L.Sh.	Area	%Area
Cr2O3 -5	578.74	1.10	GL(30)	667.2	2.1
Cr2O3 - 4	577.93	1.10	GL(30)	1048.5	3.2
Cr2O3 - 3	576.93	1.10	GL(30)	2478.3	7.6
Cr(OH)3	576.84	2.40	GL(30)	6055.1	18.7
Cr2O3 - 2	576.15	1.10	GL(30)	4623.0	14.2
Cr2O3 - 1	575.14	1.10	GL(30)	4765.9	14.7
Cr Metal	573.16	1.10	LA(1.3,4,5)	12808.5	39.5

LPBF-XY, inside wear track

Name	Pos.	FWHM	L.Sh.	Area	%Area
Cr2O3 -5	579.04	1.10	GL(30)	98.2	1.2
Cr2O3 - 4	578.23	1.10	GL(30)	154.3	1.9
Cr2O3 - 3	577.23	1.10	GL(30)	364.8	4.4
Cr(OH)3	576.84	2.50	GL(30)	4634.4	55.6
Cr2O3 - 2	576.45	1.10	GL(30)	680.4	8.2
Cr2O3 - 1	575.44	1.10	GL(30)	701.5	8.4
Cr Metal	573.25	1.15	LA(1.3,4,5)	1700.9	20.4

Figure S15. Cr 2p high-resolution spectra of wrought, LPBF-XZ, and LPF-XY CoCrMo outside (left) and inside (right) of the wear track, after tribocorrosion exposure 1 h no sliding, followed by 1 h reciprocal linear sliding at 3 N load, followed by 0.5 h no sliding, at 37 °C and at pH 7.3, in NaCl+MES.

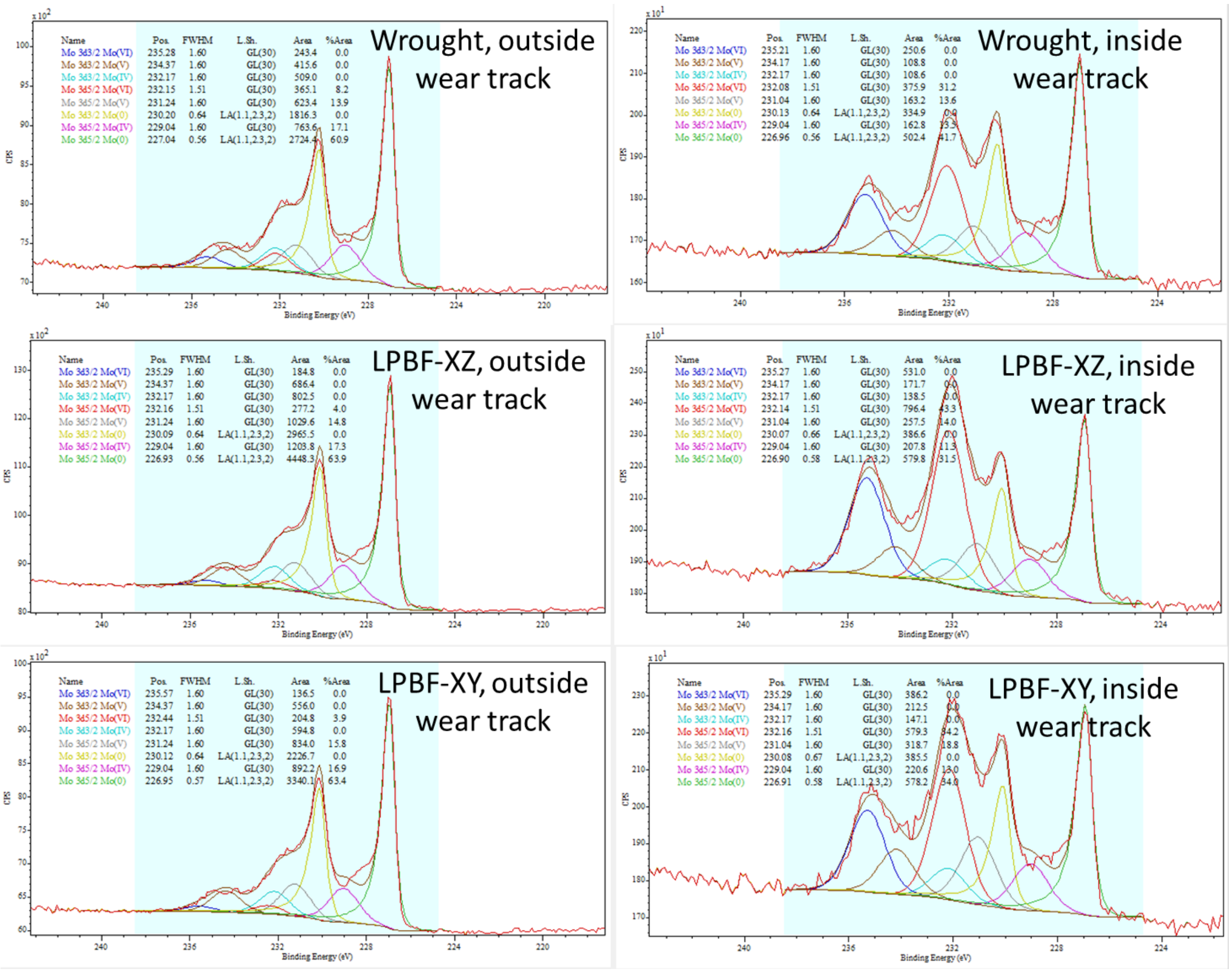

Wrought, outside wear track

Name	Pos.	FWHM	L.Sh.	Area	%Area
Mo 3d3/2 Mo(VI)	235.28	1.60	GL(30)	243.4	0.0
Mo 3d3/2 Mo(V)	234.37	1.60	GL(30)	415.6	0.0
Mo 3d3/2 Mo(IV)	232.17	1.60	GL(30)	509.0	0.0
Mo 3d5/2 Mo(VI)	232.15	1.51	GL(30)	365.1	8.2
Mo 3d5/2 Mo(V)	231.24	1.60	GL(30)	623.4	13.9
Mo 3d3/2 Mo(0)	230.20	0.64	LA(1.1,2.3,2)	1816.3	0.0
Mo 3d5/2 Mo(IV)	229.04	1.60	GL(30)	763.6	17.1
Mo 3d5/2 Mo(0)	227.04	0.56	LA(1.1,2.3,2)	2724.4	60.9

Wrought, inside wear track

Name	Pos.	FWHM	L.Sh.	Area	%Area
Mo 3d3/2 Mo(VI)	235.21	1.60	GL(30)	250.6	0.0
Mo 3d3/2 Mo(V)	234.17	1.60	GL(30)	108.8	0.0
Mo 3d3/2 Mo(IV)	232.17	1.60	GL(30)	108.6	0.0
Mo 3d5/2 Mo(VI)	232.08	1.51	GL(30)	375.9	31.2
Mo 3d5/2 Mo(V)	231.04	1.60	GL(30)	163.2	13.6
Mo 3d3/2 Mo(0)	230.13	0.64	LA(1.1,2.3,2)	334.9	0.0
Mo 3d5/2 Mo(IV)	229.04	1.60	GL(30)	162.8	13.5
Mo 3d5/2 Mo(0)	226.96	0.56	LA(1.1,2.3,2)	502.4	41.7

LPBF-XZ, outside wear track

Name	Pos.	FWHM	L.Sh.	Area	%Area
Mo 3d3/2 Mo(VI)	235.29	1.60	GL(30)	184.8	0.0
Mo 3d3/2 Mo(V)	234.37	1.60	GL(30)	686.4	0.0
Mo 3d3/2 Mo(IV)	232.17	1.60	GL(30)	802.5	0.0
Mo 3d5/2 Mo(VI)	232.16	1.51	GL(30)	277.2	4.0
Mo 3d5/2 Mo(V)	231.24	1.60	GL(30)	1029.6	14.8
Mo 3d3/2 Mo(0)	230.09	0.64	LA(1.1,2.3,2)	2965.5	0.0
Mo 3d5/2 Mo(IV)	229.04	1.60	GL(30)	1203.8	17.3
Mo 3d5/2 Mo(0)	226.93	0.56	LA(1.1,2.3,2)	4448.3	63.9

LPBF-XZ, inside wear track

Name	Pos.	FWHM	L.Sh.	Area	%Area
Mo 3d3/2 Mo(VI)	235.27	1.60	GL(30)	531.0	0.0
Mo 3d3/2 Mo(V)	234.17	1.60	GL(30)	171.7	0.0
Mo 3d3/2 Mo(IV)	232.17	1.60	GL(30)	138.5	0.0
Mo 3d5/2 Mo(VI)	232.14	1.51	GL(30)	796.4	43.3
Mo 3d5/2 Mo(V)	231.04	1.60	GL(30)	257.5	14.0
Mo 3d3/2 Mo(0)	230.07	0.66	LA(1.1,2.3,2)	386.6	0.0
Mo 3d5/2 Mo(IV)	229.04	1.60	GL(30)	207.8	11.3
Mo 3d5/2 Mo(0)	226.90	0.58	LA(1.1,2.3,2)	579.8	31.5

LPBF-XY, outside wear track

Name	Pos.	FWHM	L.Sh.	Area	%Area
Mo 3d3/2 Mo(VI)	235.57	1.60	GL(30)	136.5	0.0
Mo 3d3/2 Mo(V)	234.37	1.60	GL(30)	556.0	0.0
Mo 3d5/2 Mo(VI)	232.44	1.51	GL(30)	204.8	3.9
Mo 3d3/2 Mo(IV)	232.17	1.60	GL(30)	594.8	0.0
Mo 3d5/2 Mo(V)	231.24	1.60	GL(30)	834.0	15.8
Mo 3d3/2 Mo(0)	230.12	0.64	LA(1.1,2.3,2)	2226.7	0.0
Mo 3d5/2 Mo(IV)	229.04	1.60	GL(30)	892.2	16.9
Mo 3d5/2 Mo(0)	226.95	0.57	LA(1.1,2.3,2)	3340.1	63.4

LPBF-XY, inside wear track

Name	Pos.	FWHM	L.Sh.	Area	%Area
Mo 3d3/2 Mo(VI)	235.29	1.60	GL(30)	386.2	0.0
Mo 3d3/2 Mo(V)	234.17	1.60	GL(30)	212.5	0.0
Mo 3d3/2 Mo(IV)	232.17	1.60	GL(30)	147.1	0.0
Mo 3d5/2 Mo(VI)	232.16	1.51	GL(30)	579.3	34.2
Mo 3d5/2 Mo(V)	231.04	1.60	GL(30)	318.7	18.8
Mo 3d3/2 Mo(0)	230.08	0.67	LA(1.1,2.3,2)	385.5	0.0
Mo 3d5/2 Mo(IV)	229.04	1.60	GL(30)	220.6	13.0
Mo 3d5/2 Mo(0)	226.91	0.58	LA(1.1,2.3,2)	578.2	34.0

Figure S16. Mo 3d high-resolution spectra of wrought, LPBF-XZ, and LPF-XY CoCrMo outside (left) and inside (right) of the wear track, after tribocorrosion exposure 1 h no sliding, followed by 1 h reciprocal linear sliding at 3 N load, followed by 0.5 h no sliding, at 37 °C and at pH 7.3, in NaCl+MES.

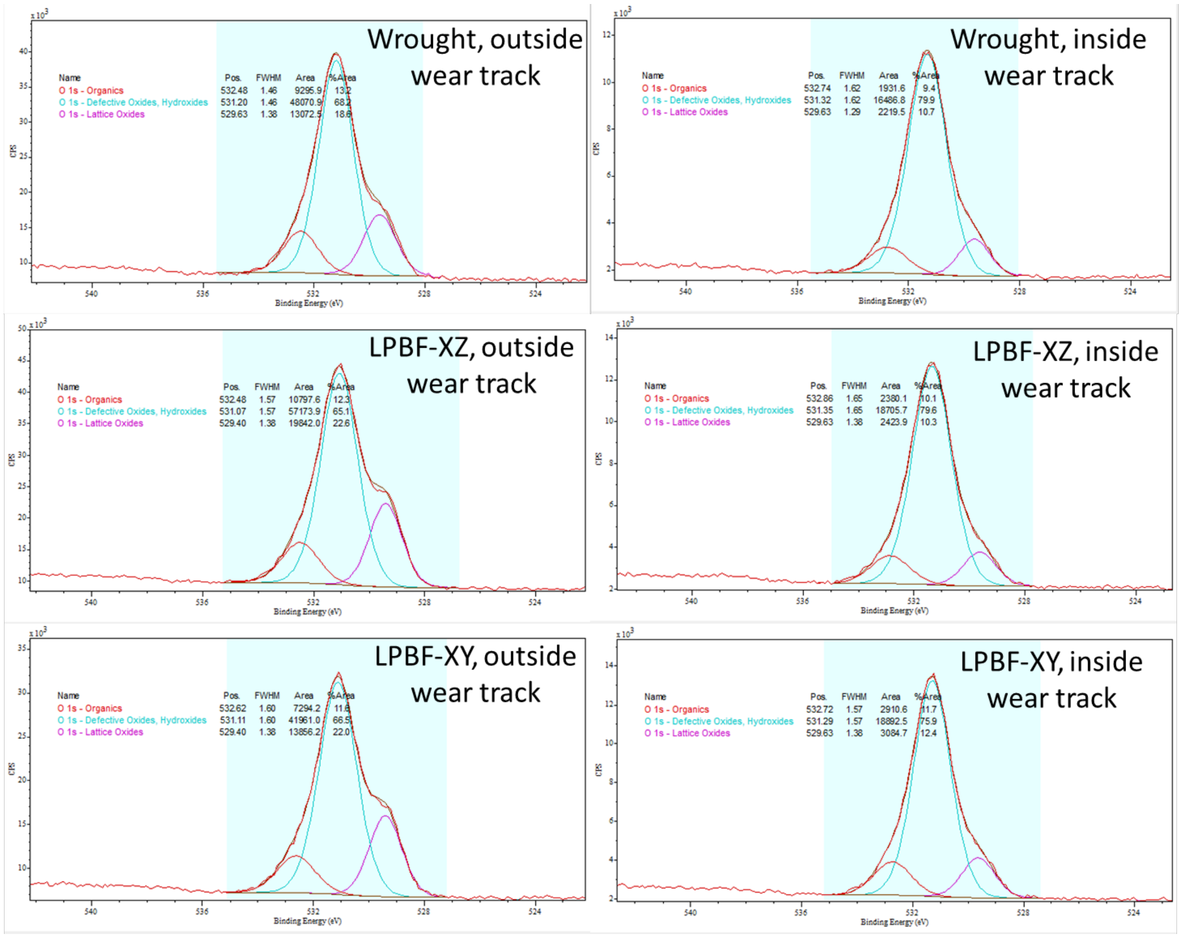

Name	Pos.	FWHM	Area	%Area
O 1s - Organics	532.48	1.46	9295.9	13.2
O 1s - Defective Oxides, Hydroxides	531.20	1.46	48070.9	68.2
O 1s - Lattice Oxides	529.63	1.38	13072.5	18.6

Name	Pos.	FWHM	Area	%Area
O 1s - Organics	532.74	1.62	1931.6	9.4
O 1s - Defective Oxides, Hydroxides	531.32	1.62	16486.8	79.9
O 1s - Lattice Oxides	529.63	1.29	2219.5	10.7

Name	Pos.	FWHM	Area	%Area
O 1s - Organics	532.48	1.57	10797.6	12.3
O 1s - Defective Oxides, Hydroxides	531.07	1.57	57173.9	65.1
O 1s - Lattice Oxides	529.40	1.38	19842.0	22.6

Name	Pos.	FWHM	Area	%Area
O 1s - Organics	532.86	1.65	2380.1	10.1
O 1s - Defective Oxides, Hydroxides	531.35	1.65	18705.7	79.6
O 1s - Lattice Oxides	529.63	1.38	2423.9	10.3

Name	Pos.	FWHM	Area	%Area
O 1s - Organics	532.62	1.60	7294.2	11.6
O 1s - Defective Oxides, Hydroxides	531.11	1.60	41961.0	66.5
O 1s - Lattice Oxides	529.40	1.38	13856.2	22.0

Name	Pos.	FWHM	Area	%Area
O 1s - Organics	532.72	1.57	2910.6	11.7
O 1s - Defective Oxides, Hydroxides	531.29	1.57	18892.5	75.9
O 1s - Lattice Oxides	529.63	1.38	3084.7	12.4

Figure S17. O 1s high-resolution spectra of wrought, LPBF-XZ, and LPF-XY CoCrMo outside (left) and inside (right) of the wear track, after tribocorrosion exposure 1 h no sliding, followed by 1 h reciprocal linear sliding at 3 N load, followed by 0.5 h no sliding, at 37 °C and at pH 7.3, in NaCl+MES.

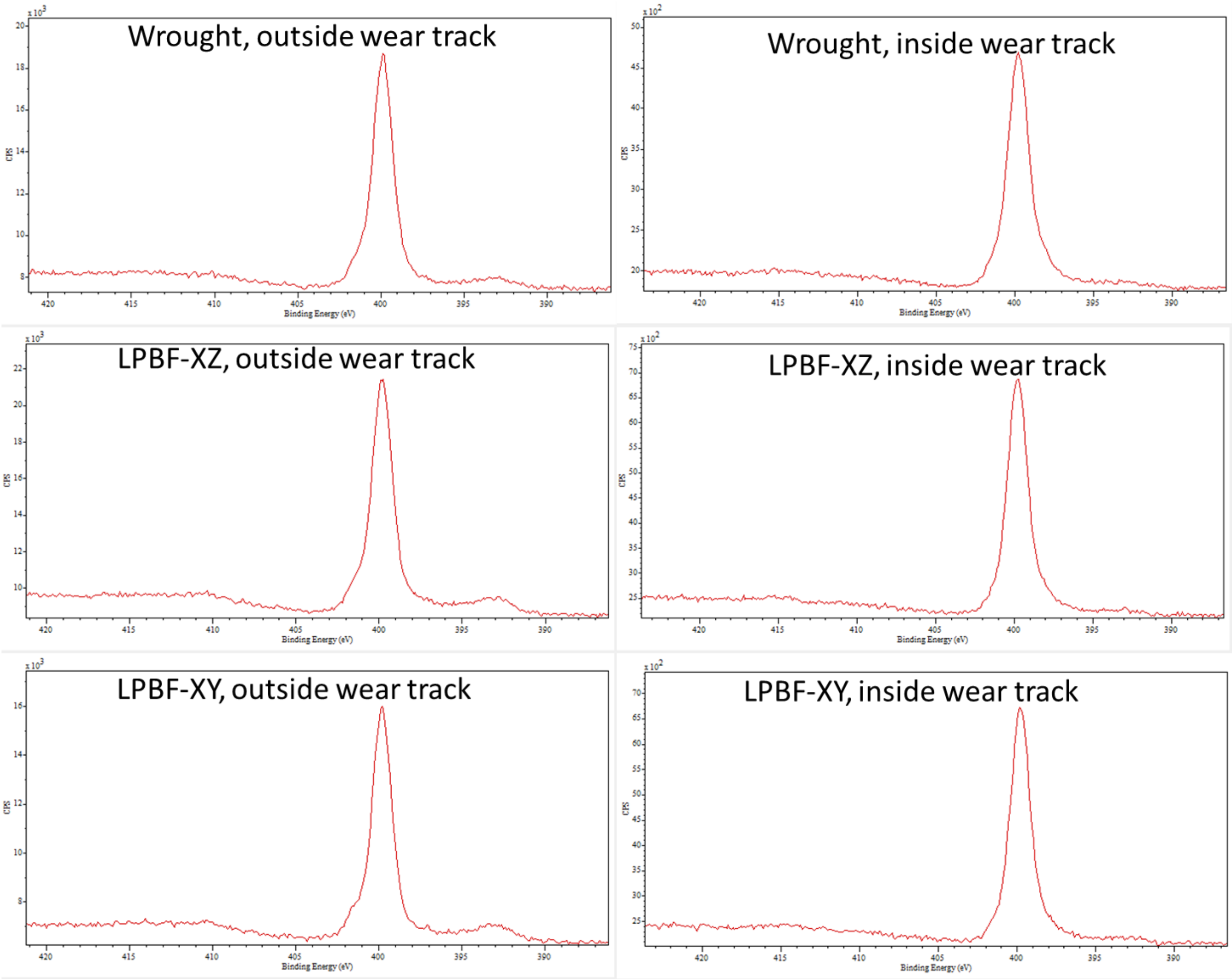

Figure S18. N 1s high-resolution spectra of wrought, LPBF-XZ, and LPF-XY CoCrMo outside (left) and inside (right) of the wear track, after tribocorrosion exposure 1 h no sliding, followed by 1 h reciprocal linear sliding at 3 N load, followed by 0.5 h no sliding, at 37 °C and at pH 7.3, in NaCl+MES.

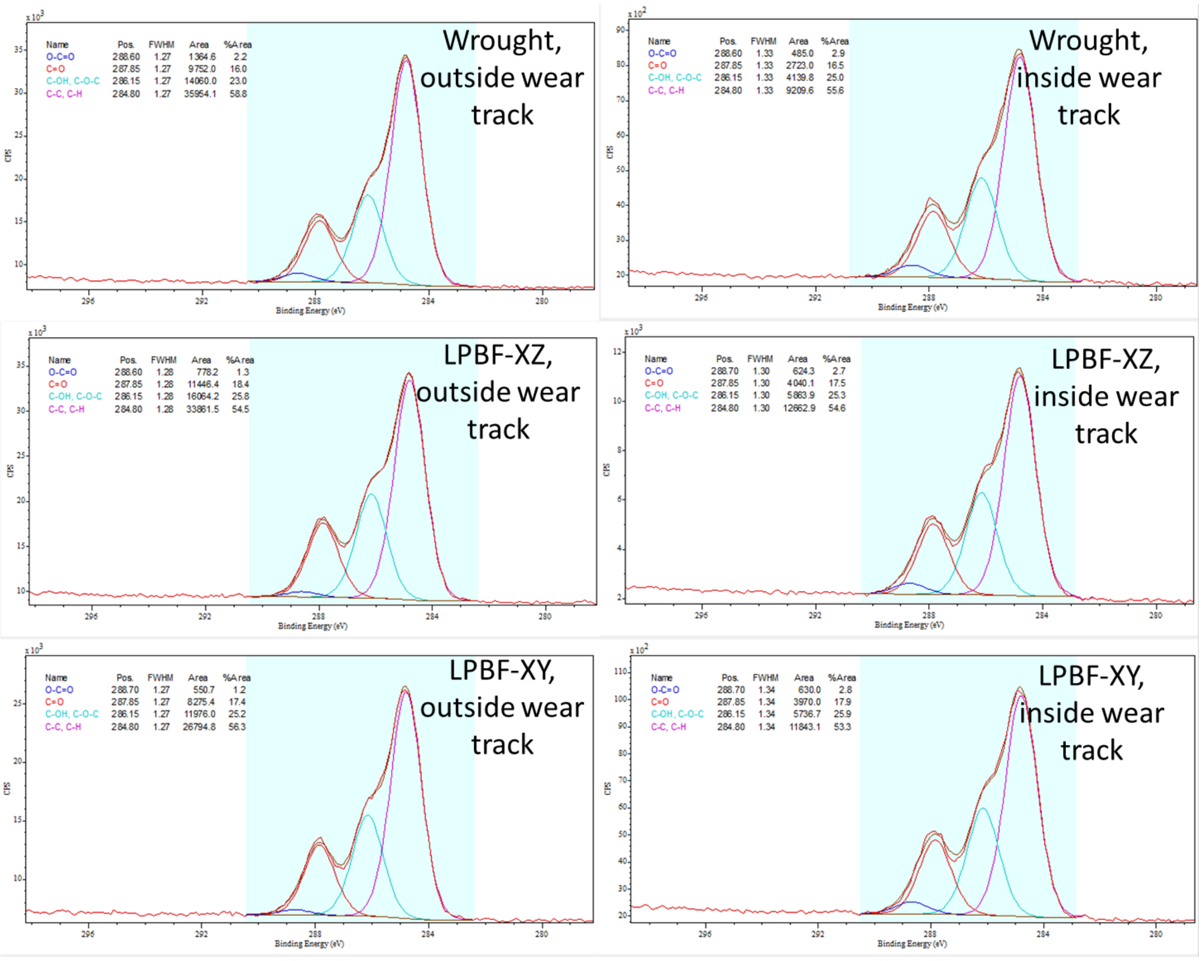

Wrought, outside wear track

Name	Pos.	FWHM	Area	%Area
O-C=O	288.60	1.27	1364.6	2.2
C=O	287.85	1.27	9752.0	16.0
C-OH, C-O-C	286.15	1.27	14060.0	23.0
C-C, C-H	284.80	1.27	35954.1	58.8

Wrought, inside wear track

Name	Pos.	FWHM	Area	%Area
O-C=O	288.60	1.33	485.0	2.9
C=O	287.85	1.33	2723.0	16.5
C-OH, C-O-C	286.15	1.33	4139.8	25.0
C-C, C-H	284.80	1.33	9209.6	55.6

LPBF-XZ, outside wear track

Name	Pos.	FWHM	Area	%Area
O-C=O	288.60	1.28	778.2	1.3
C=O	287.85	1.28	11446.4	18.4
C-OH, C-O-C	286.15	1.28	16064.2	25.8
C-C, C-H	284.80	1.28	33861.5	54.5

LPBF-XZ, inside wear track

Name	Pos.	FWHM	Area	%Area
O-C=O	288.70	1.30	624.3	2.7
C=O	287.85	1.30	4040.1	17.5
C-OH, C-O-C	286.15	1.30	5863.9	25.3
C-C, C-H	284.80	1.30	12662.9	54.6

LPBF-XY, outside wear track

Name	Pos.	FWHM	Area	%Area
O-C=O	288.70	1.27	550.7	1.2
C=O	287.85	1.27	8275.4	17.4
C-OH, C-O-C	286.15	1.27	11976.0	25.2
C-C, C-H	284.80	1.27	26794.8	56.3

LPBF-XY, inside wear track

Name	Pos.	FWHM	Area	%Area
O-C=O	288.70	1.34	630.0	2.8
C=O	287.85	1.34	3970.0	17.9
C-OH, C-O-C	286.15	1.34	5736.7	25.9
C-C, C-H	284.80	1.34	11843.1	53.3

Figure S19. C 1s high-resolution spectra of wrought, LPBF-XZ, and LPF-XY CoCrMo outside (left) and inside (right) of the wear track, after tribocorrosion exposure 1 h no sliding, followed by 1 h reciprocal linear sliding at 3 N load, followed by 0.5 h no sliding, at 37 °C and at pH 7.3, in NaCl+MES.

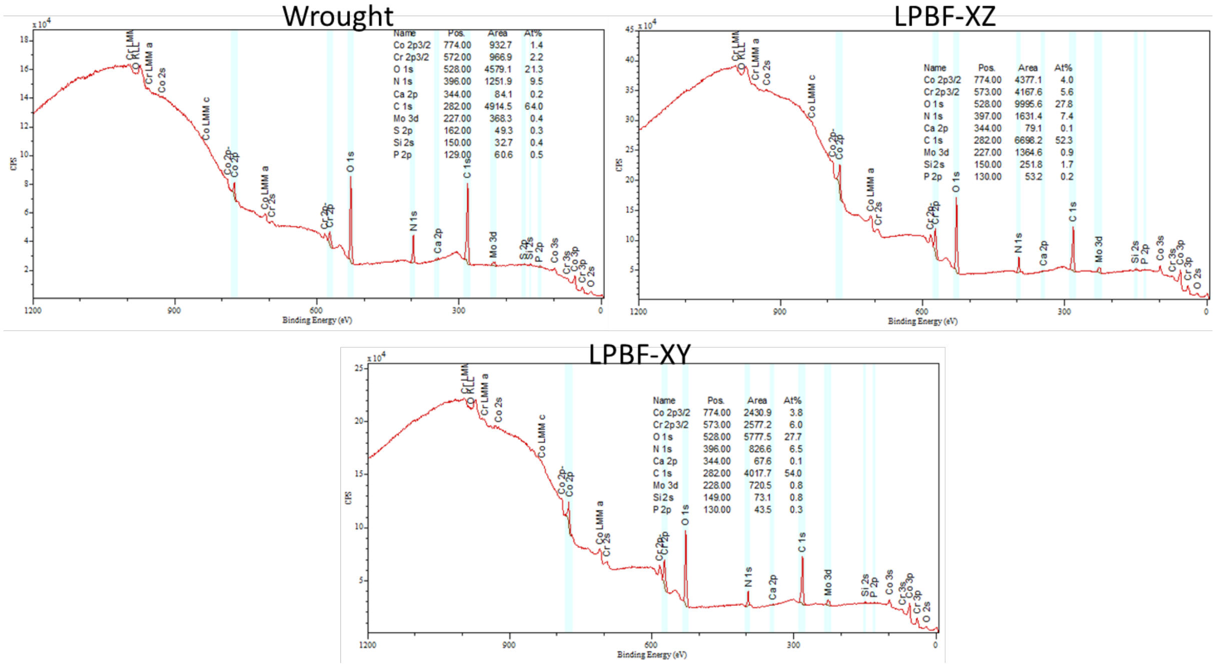

Wrought

Name	Pos.	Area	At%
Co 2p3/2	774.00	932.7	1.4
Cr 2p3/2	572.00	966.9	2.2
O 1s	528.00	4579.1	21.3
N 1s	396.00	1251.9	9.5
Ca 2p	344.00	84.1	0.2
C 1s	282.00	4914.5	64.0
Mo 3d	227.00	368.3	0.4
S 2p	162.00	49.3	0.3
Si 2s	150.00	32.7	0.4
P 2p	129.00	60.6	0.5

LPBF-XZ

Name	Pos.	Area	At%
Co 2p3/2	774.00	4377.1	4.0
Cr 2p3/2	573.00	4167.6	5.6
O 1s	528.00	9995.6	27.8
N 1s	397.00	1631.4	7.4
Ca 2p	344.00	79.1	0.1
C 1s	282.00	6698.2	52.3
Mo 3d	227.00	1364.6	0.9
Si 2s	150.00	251.8	1.7
P 2p	130.00	53.2	0.2

LPBF-XY

Name	Pos.	Area	At%
Co 2p3/2	774.00	2430.9	3.8
Cr 2p3/2	573.00	2577.2	6.0
O 1s	528.00	5777.5	27.7
N 1s	396.00	826.6	6.5
Ca 2p	344.00	67.6	0.1
C 1s	282.00	4017.7	54.0
Mo 3d	228.00	720.5	0.8
Si 2s	149.00	73.1	0.8
P 2p	130.00	43.5	0.3

Figure S20. Wide spectra of wrought, LPBF-XZ, and LPF-XY CoCrMo outside of the wear track, after tribocorrosion exposure 1 h no sliding, followed by 1 h reciprocal linear sliding at 3 N load, followed by 0.5 h no sliding, at 37 °C and at pH 7.3, in NaCl+MES+BSA.

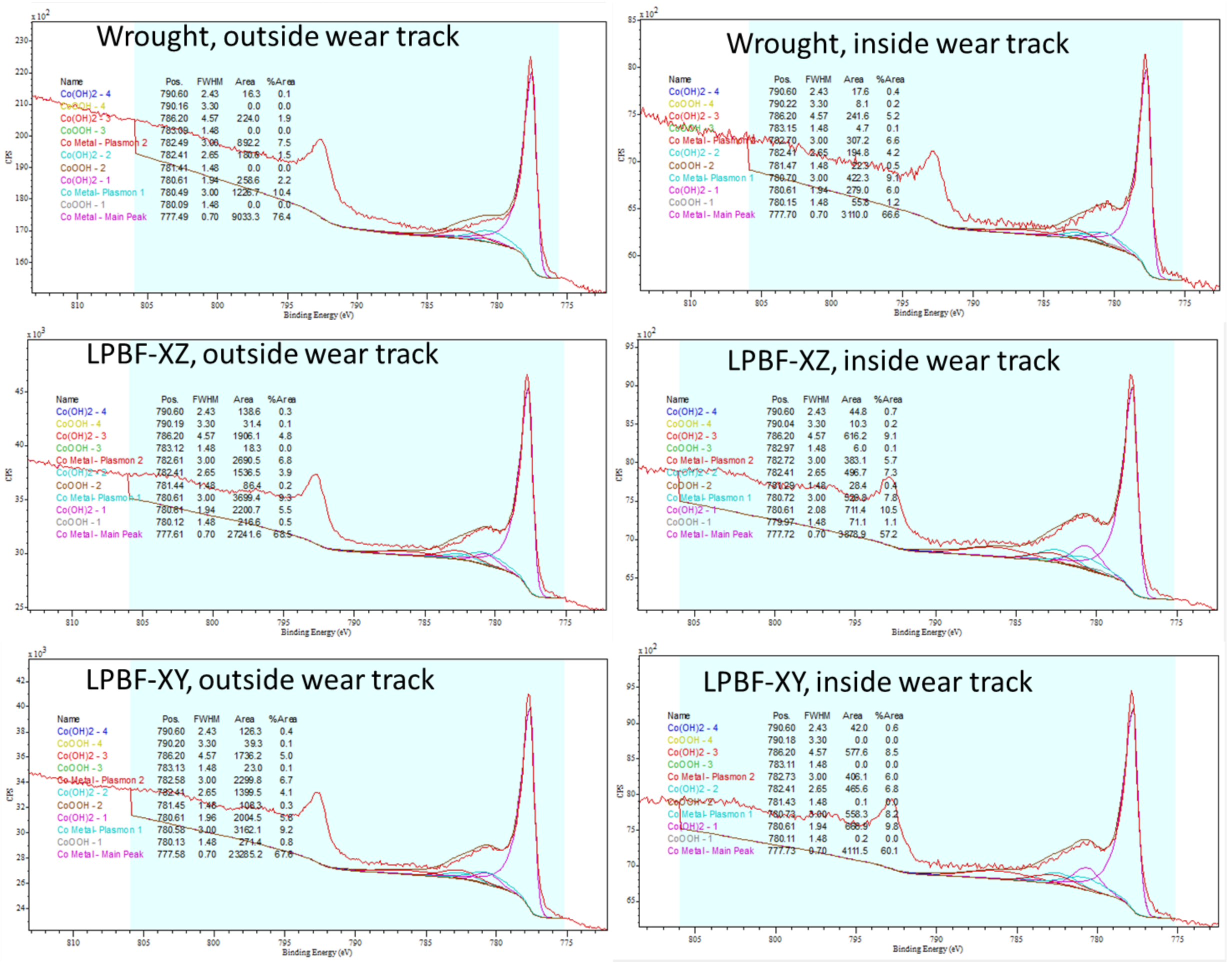

Wrought, outside wear track

Name	Pos.	FWHM	Area	%Area
Co(OH)2 - 4	790.60	2.43	16.3	0.1
CoOOH - 4	790.16	3.30	0.0	0.0
Co(OH)2 - 3	786.20	4.57	224.0	1.9
CoOOH - 3	783.09	1.48	0.0	0.0
Co Metal - Plasmon 2	782.49	3.00	892.2	7.5
Co(OH)2 - 2	782.41	2.65	180.6	1.5
CoOOH - 2	781.41	1.48	0.0	0.0
Co(OH)2 - 1	780.61	1.94	258.6	2.2
Co Metal- Plasmon 1	780.49	3.00	1226.7	10.4
CoOOH - 1	780.09	1.48	0.0	0.0
Co Metal - Main Peak	777.49	0.70	9033.3	76.4

Wrought, inside wear track

Name	Pos.	FWHM	Area	%Area
Co(OH)2 - 4	790.60	2.43	17.6	0.4
CoOOH - 4	790.22	3.30	8.1	0.2
Co(OH)2 - 3	786.20	4.57	241.6	5.2
CoOOH - 3	783.15	1.48	4.7	0.1
Co Metal - Plasmon 2	782.70	3.00	307.2	6.6
Co(OH)2 - 2	782.41	2.65	194.8	4.2
CoOOH - 2	781.47	1.48	22.3	0.5
Co Metal- Plasmon 1	780.70	3.00	422.3	9.1
Co(OH)2 - 1	780.61	1.94	279.0	6.0
CoOOH - 1	780.15	1.48	55.8	1.2
Co Metal - Main Peak	777.70	0.70	3110.0	66.6

LPBF-XZ, outside wear track

Name	Pos.	FWHM	Area	%Area
Co(OH)2 - 4	790.60	2.43	138.6	0.3
CoOOH - 4	790.19	3.30	31.4	0.1
Co(OH)2 - 3	786.20	4.57	1906.1	4.8
CoOOH - 3	783.12	1.48	18.3	0.0
Co Metal - Plasmon 2	782.61	3.00	2690.5	6.8
Co(OH)2 - 2	782.41	2.65	1536.5	3.9
CoOOH - 2	781.44	1.48	86.4	0.2
Co Metal- Plasmon 1	780.61	3.00	3699.4	9.3
Co(OH)2 - 1	780.61	1.94	2200.7	5.5
CoOOH - 1	780.12	1.48	216.6	0.5
Co Metal - Main Peak	777.61	0.70	27241.6	68.5

LPBF-XZ, inside wear track

Name	Pos.	FWHM	Area	%Area
Co(OH)2 - 4	790.60	2.43	44.8	0.7
CoOOH - 4	790.04	3.30	10.3	0.2
Co(OH)2 - 3	786.20	4.57	616.2	9.1
CoOOH - 3	782.97	1.48	6.0	0.1
Co Metal - Plasmon 2	782.72	3.00	383.1	5.7
Co(OH)2 - 2	782.41	2.65	496.7	7.3
CoOOH - 2	781.29	1.48	28.4	0.4
Co Metal- Plasmon 1	780.72	3.00	528.8	7.8
Co(OH)2 - 1	780.61	2.08	711.4	10.5
CoOOH - 1	779.97	1.48	71.1	1.1
Co Metal - Main Peak	777.72	0.70	3878.9	57.2

LPBF-XY, outside wear track

Name	Pos.	FWHM	Area	%Area
Co(OH)2 - 4	790.60	2.43	126.3	0.4
CoOOH - 4	790.20	3.30	39.3	0.1
Co(OH)2 - 3	786.20	4.57	1736.2	5.0
CoOOH - 3	783.13	1.48	23.0	0.1
Co Metal - Plasmon 2	782.58	3.00	2299.8	6.7
Co(OH)2 - 2	782.41	2.65	1399.5	4.1
CoOOH - 2	781.45	1.48	108.3	0.3
Co(OH)2 - 1	780.61	1.96	2004.5	5.8
Co Metal- Plasmon 1	780.58	3.00	3162.1	9.2
CoOOH - 1	780.13	1.48	271.4	0.8
Co Metal - Main Peak	777.58	0.70	23285.2	67.8

LPBF-XY, inside wear track

Name	Pos.	FWHM	Area	%Area
Co(OH)2 - 4	790.60	2.43	42.0	0.6
CoOOH - 4	790.18	3.30	0.0	0.0
Co(OH)2 - 3	786.20	4.57	577.6	8.5
CoOOH - 3	783.11	1.48	0.0	0.0
Co Metal - Plasmon 2	782.73	3.00	406.1	6.0
Co(OH)2 - 2	782.41	2.65	465.6	6.8
CoOOH - 2	781.43	1.48	0.1	0.0
Co Metal- Plasmon 1	780.73	3.00	558.3	8.2
Co(OH)2 - 1	780.61	1.94	668.9	9.8
CoOOH - 1	780.11	1.48	0.2	0.0
Co Metal - Main Peak	777.73	0.70	4111.5	60.1

Figure S21. Co 2p high-resolution spectra of wrought, LPBF-XZ, and LPF-XY CoCrMo outside (left) and inside (right) of the wear track, after tribocorrosion exposure 1 h no sliding, followed by 1 h reciprocal linear sliding at 3 N load, followed by 0.5 h no sliding, at 37 °C and at pH 7.3, in NaCl+MES+BSA.

Green open access version of https://pubs.acs.org/doi/10.1021/acsbiomaterials.3c01165

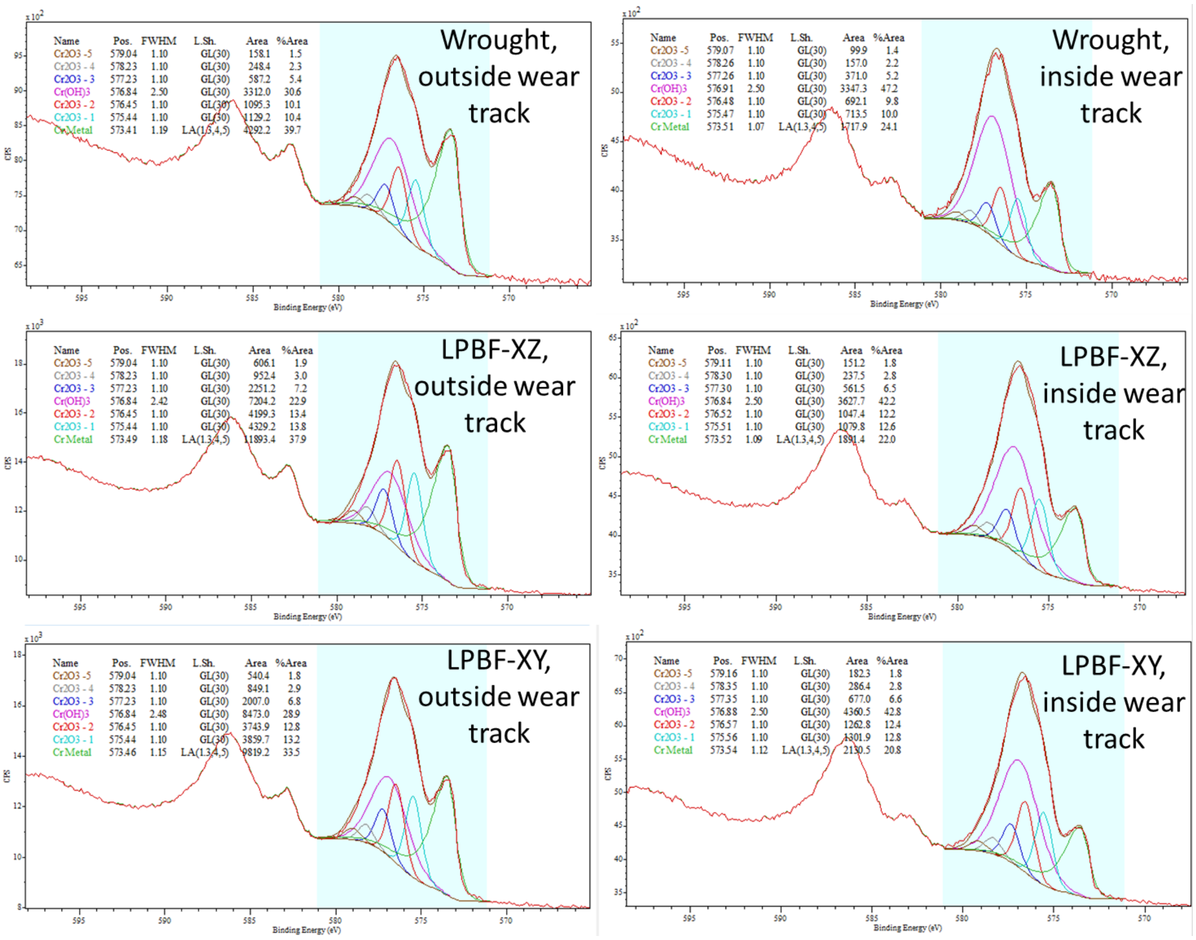

Name	Pos.	FWHM	L.Sh.	Area	%Area
Cr2O3 -5	579.04	1.10	GL(30)	158.1	1.5
Cr2O3 - 4	578.23	1.10	GL(30)	248.4	2.3
Cr2O3 - 3	577.23	1.10	GL(30)	587.2	5.4
Cr(OH)3	576.84	2.50	GL(30)	3312.0	30.6
Cr2O3 - 2	576.45	1.10	GL(30)	1095.3	10.1
Cr2O3 - 1	575.44	1.10	GL(30)	1129.2	10.4
Cr Metal	573.41	1.19	LA(1.3,4,5)	4292.2	39.7

Name	Pos.	FWHM	L.Sh.	Area	%Area
Cr2O3 -5	579.07	1.10	GL(30)	99.9	1.4
Cr2O3 - 4	578.26	1.10	GL(30)	157.0	2.2
Cr2O3 - 3	577.26	1.10	GL(30)	371.0	5.2
Cr(OH)3	576.91	2.50	GL(30)	3347.3	47.2
Cr2O3 - 2	576.48	1.10	GL(30)	692.1	9.8
Cr2O3 - 1	575.47	1.10	GL(30)	713.5	10.0
Cr Metal	573.51	1.07	LA(1.3,4,5)	1717.9	24.1

Name	Pos.	FWHM	L.Sh.	Area	%Area
Cr2O3 -5	579.04	1.10	GL(30)	606.1	1.9
Cr2O3 - 4	578.23	1.10	GL(30)	952.4	3.0
Cr2O3 - 3	577.23	1.10	GL(30)	2251.2	7.2
Cr(OH)3	576.84	2.42	GL(30)	7204.2	22.9
Cr2O3 - 2	576.45	1.10	GL(30)	4199.3	13.4
Cr2O3 - 1	575.44	1.10	GL(30)	4329.2	13.8
Cr Metal	573.49	1.18	LA(1.3,4,5)	11893.4	37.9

Name	Pos.	FWHM	L.Sh.	Area	%Area
Cr2O3 -5	579.11	1.10	GL(30)	151.2	1.8
Cr2O3 - 4	578.30	1.10	GL(30)	237.5	2.8
Cr2O3 - 3	577.30	1.10	GL(30)	561.5	6.5
Cr(OH)3	576.84	2.50	GL(30)	3627.7	42.2
Cr2O3 - 2	576.52	1.10	GL(30)	1047.4	12.2
Cr2O3 - 1	575.51	1.10	GL(30)	1079.8	12.6
Cr Metal	573.52	1.09	LA(1.3,4,5)	1891.4	22.0

Name	Pos.	FWHM	L.Sh.	Area	%Area
Cr2O3 -5	579.04	1.10	GL(30)	540.4	1.8
Cr2O3 - 4	578.23	1.10	GL(30)	849.1	2.9
Cr2O3 - 3	577.23	1.10	GL(30)	2007.0	6.8
Cr(OH)3	576.84	2.48	GL(30)	8473.0	28.9
Cr2O3 - 2	576.45	1.10	GL(30)	3743.9	12.8
Cr2O3 - 1	575.44	1.10	GL(30)	3859.7	13.2
Cr Metal	573.46	1.15	LA(1.3,4,5)	9819.2	33.5

Name	Pos.	FWHM	L.Sh.	Area	%Area
Cr2O3 -5	579.16	1.10	GL(30)	182.3	1.8
Cr2O3 - 4	578.35	1.10	GL(30)	286.4	2.8
Cr2O3 - 3	577.35	1.10	GL(30)	677.0	6.6
Cr(OH)3	576.88	2.50	GL(30)	4360.5	42.8
Cr2O3 - 2	576.57	1.10	GL(30)	1262.8	12.4
Cr2O3 - 1	575.56	1.10	GL(30)	1301.9	12.8
Cr Metal	573.54	1.12	LA(1.3,4,5)	2130.5	20.8

Figure S22. Cr 2p high-resolution spectra of wrought, LPBF-XZ, and LPF-XY CoCrMo outside (left) and inside (right) of the wear track, after tribocorrosion exposure 1 h no sliding, followed by 1 h reciprocal linear sliding at 3 N load, followed by 0.5 h no sliding, at 37 °C and at pH 7.3, in NaCl+MES+BSA.

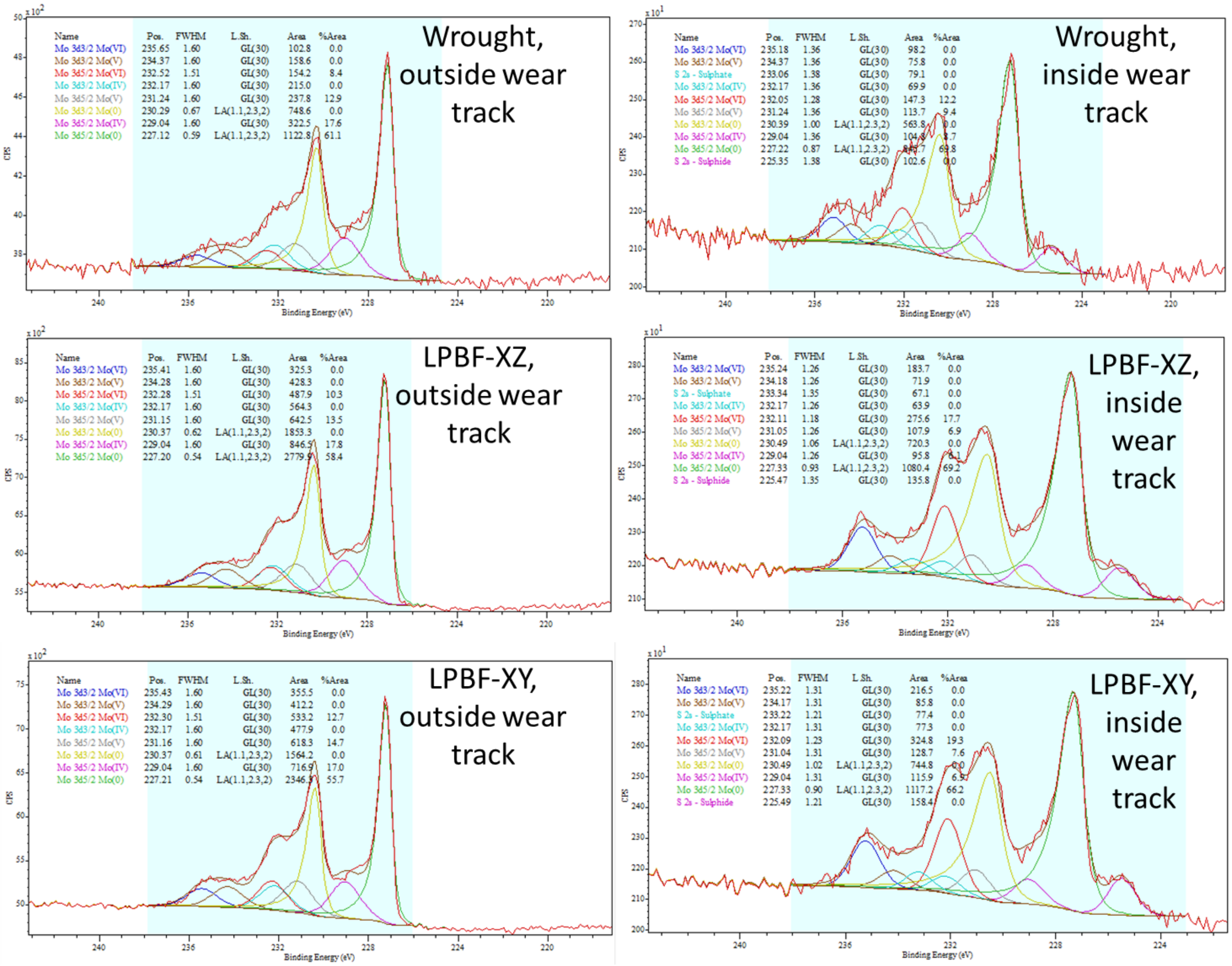

Figure S23. Mo 3d high-resolution spectra of wrought, LPBF-XZ, and LPF-XY CoCrMo outside (left) and inside (right) of the wear track, after tribocorrosion exposure 1 h no sliding, followed by 1 h reciprocal linear sliding at 3 N load, followed by 0.5 h no sliding, at 37 °C and at pH 7.3, in NaCl+MES+BSA. The overlap of 3d and S 2s (only inside wear track) is accounted for.

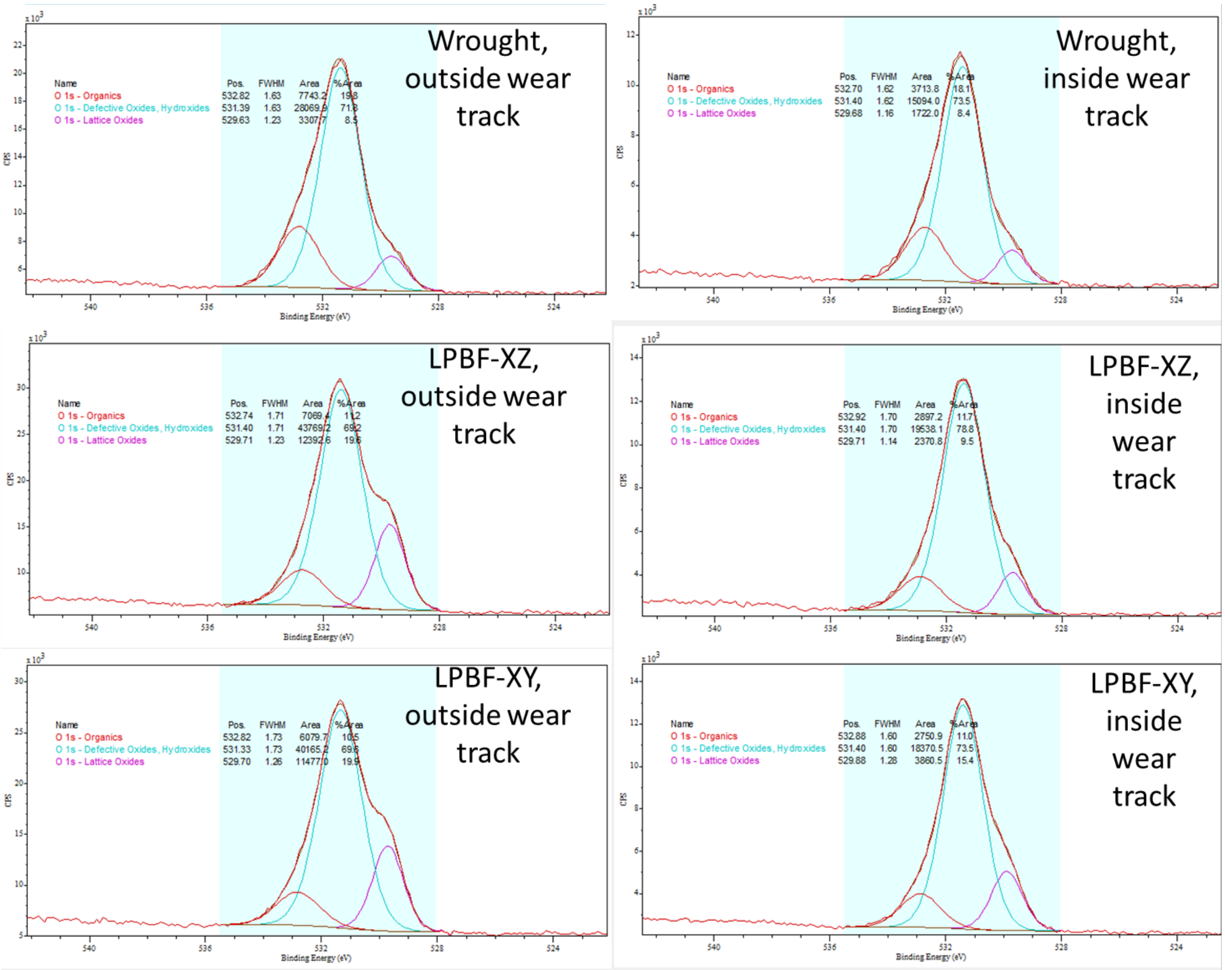

Wrought, outside wear track

Name	Pos.	FWHM	Area	%Area
O 1s - Organics	532.82	1.63	7743.2	19.8
O 1s - Defective Oxides, Hydroxides	531.39	1.63	28069.9	71.8
O 1s - Lattice Oxides	529.63	1.23	3307.7	8.5

Wrought, inside wear track

Name	Pos.	FWHM	Area	%Area
O 1s - Organics	532.70	1.62	3713.8	18.1
O 1s - Defective Oxides, Hydroxides	531.40	1.62	15094.0	73.5
O 1s - Lattice Oxides	529.68	1.16	1722.0	8.4

LPBF-XZ, outside wear track

Name	Pos.	FWHM	Area	%Area
O 1s - Organics	532.74	1.71	7069.4	11.2
O 1s - Defective Oxides, Hydroxides	531.40	1.71	43769.2	69.2
O 1s - Lattice Oxides	529.71	1.23	12392.6	19.6

LPBF-XZ, inside wear track

Name	Pos.	FWHM	Area	%Area
O 1s - Organics	532.92	1.70	2897.2	11.7
O 1s - Defective Oxides, Hydroxides	531.40	1.70	19538.1	78.8
O 1s - Lattice Oxides	529.71	1.14	2370.8	9.5

LPBF-XY, outside wear track

Name	Pos.	FWHM	Area	%Area
O 1s - Organics	532.82	1.73	6079.7	10.5
O 1s - Defective Oxides, Hydroxides	531.33	1.73	40165.2	69.6
O 1s - Lattice Oxides	529.70	1.26	11477.0	19.9

LPBF-XY, inside wear track

Name	Pos.	FWHM	Area	%Area
O 1s - Organics	532.88	1.60	2750.9	11.0
O 1s - Defective Oxides, Hydroxides	531.40	1.60	18370.5	73.5
O 1s - Lattice Oxides	529.88	1.28	3860.5	15.4

Figure S24. O 1s high-resolution spectra of wrought, LPBF-XZ, and LPF-XY CoCrMo outside (left) and inside (right) of the wear track, after tribocorrosion exposure 1 h no sliding, followed by 1 h reciprocal linear sliding at 3 N load, followed by 0.5 h no sliding, at 37 °C and at pH 7.3, in NaCl+MES+BSA.

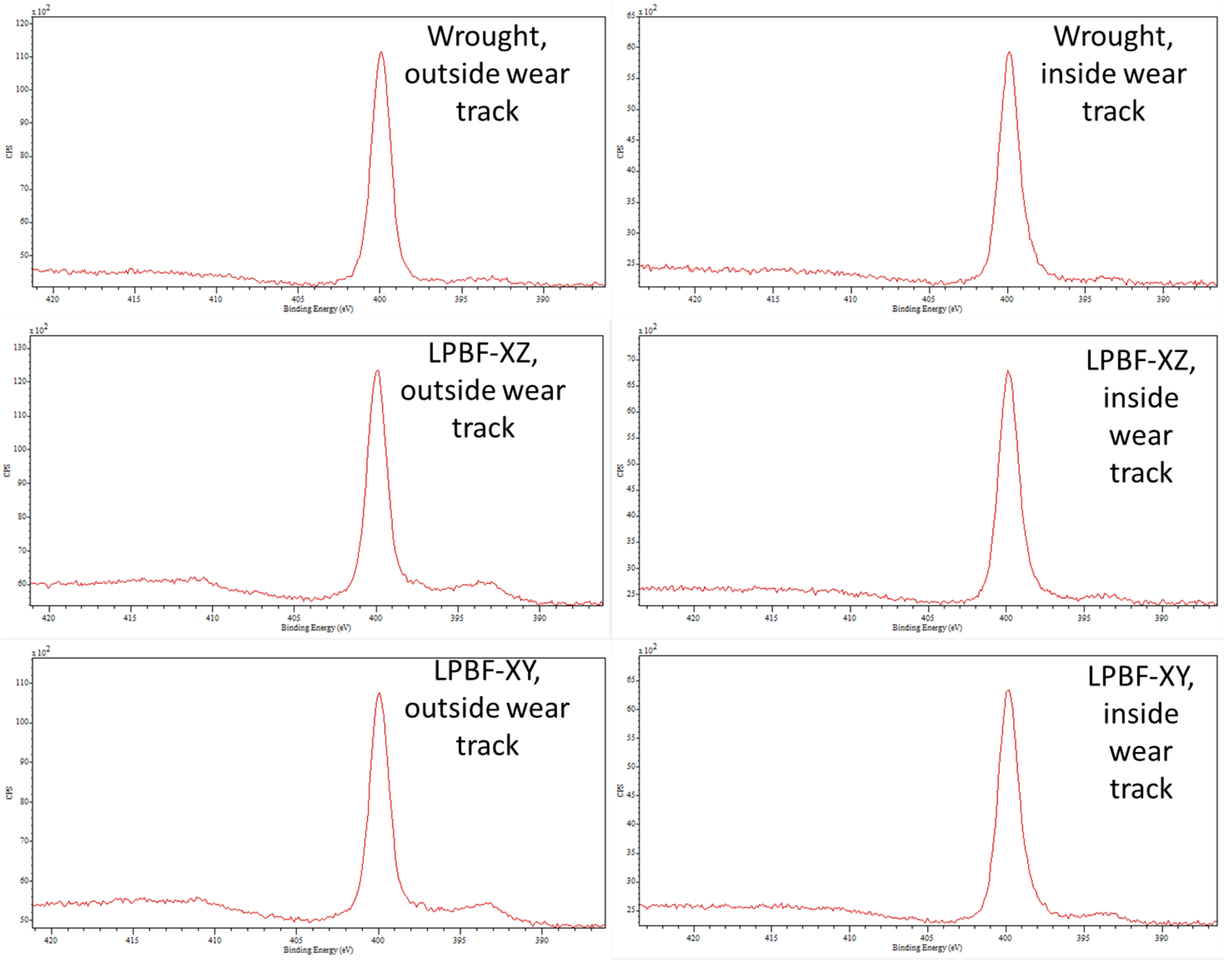

Figure S25. N 1s high-resolution spectra of wrought, LPBF-XZ, and LPF-XY CoCrMo outside (left) and inside (right) of the wear track, after tribocorrosion exposure 1 h no sliding, followed by 1 h reciprocal linear sliding at 3 N load, followed by 0.5 h no sliding, at 37 °C and at pH 7.3, in NaCl+MES+BSA.

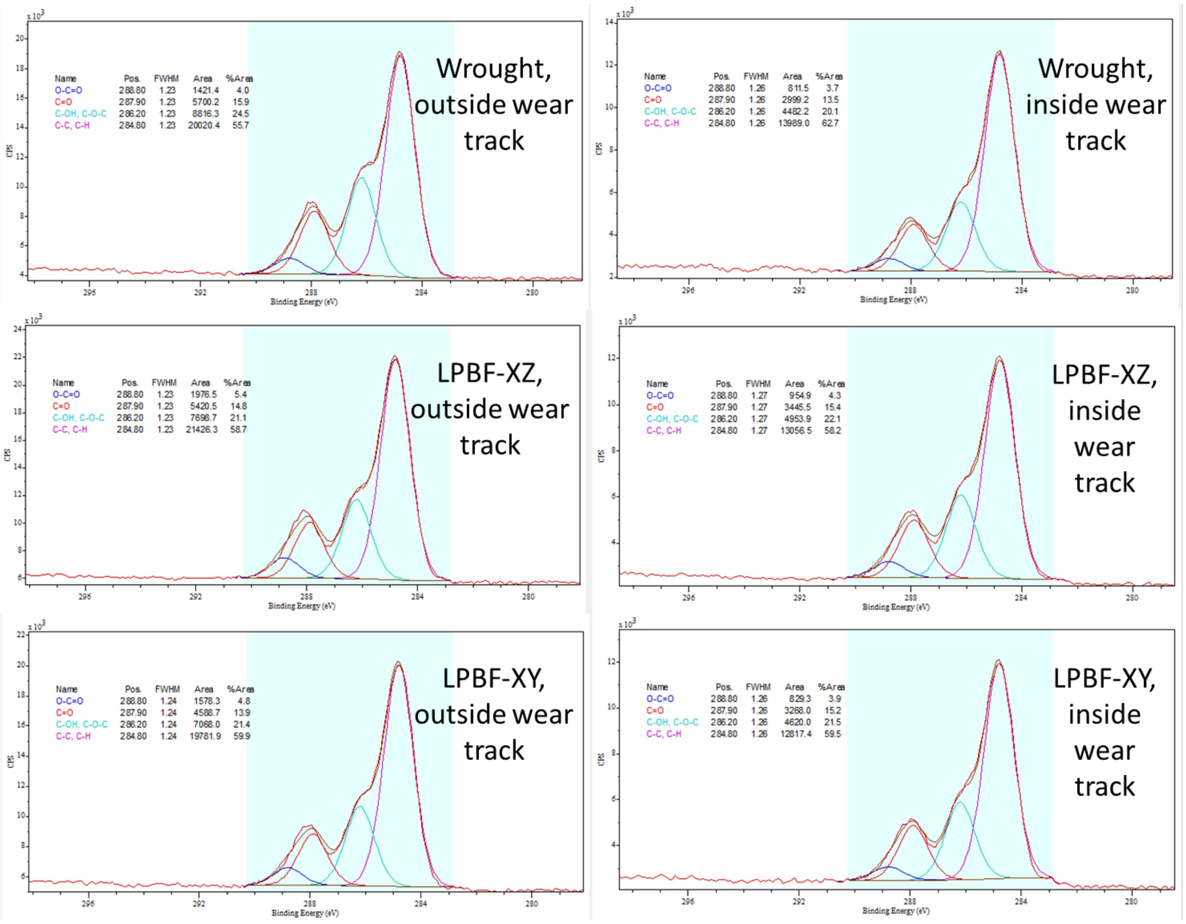

Name	Pos.	FWHM	Area	%Area
O-C=O	288.80	1.23	1421.4	4.0
C=O	287.90	1.23	5700.2	15.9
C-OH, C-O-C	286.20	1.23	8816.3	24.5
C-C, C-H	284.80	1.23	20020.4	55.7

Name	Pos.	FWHM	Area	%Area
O-C=O	288.80	1.26	811.5	3.7
C=O	287.90	1.26	2999.2	13.5
C-OH, C-O-C	286.20	1.26	4482.2	20.1
C-C, C-H	284.80	1.26	13989.0	62.7

Name	Pos.	FWHM	Area	%Area
O-C=O	288.80	1.23	1976.5	5.4
C=O	287.90	1.23	5420.5	14.8
C-OH, C-O-C	286.20	1.23	7698.7	21.1
C-C, C-H	284.80	1.23	21426.3	58.7

Name	Pos.	FWHM	Area	%Area
O-C=O	288.80	1.27	954.9	4.3
C=O	287.90	1.27	3445.5	15.4
C-OH, C-O-C	286.20	1.27	4953.9	22.1
C-C, C-H	284.80	1.27	13056.5	58.2

Name	Pos.	FWHM	Area	%Area
O-C=O	288.80	1.24	1578.3	4.8
C=O	287.90	1.24	4588.7	13.9
C-OH, C-O-C	286.20	1.24	7068.0	21.4
C-C, C-H	284.80	1.24	19781.9	59.9

Name	Pos.	FWHM	Area	%Area
O-C=O	288.80	1.26	829.3	3.9
C=O	287.90	1.26	3268.0	15.2
C-OH, C-O-C	286.20	1.26	4620.0	21.5
C-C, C-H	284.80	1.26	12817.4	59.5

Figure S26. C 1s high-resolution spectra of wrought, LPBF-XZ, and LPF-XY CoCrMo outside (left) and inside (right) of the wear track, after tribocorrosion exposure 1 h no sliding, followed by 1 h reciprocal linear sliding at 3 N load, followed by 0.5 h no sliding, at 37 °C and at pH 7.3, in NaCl+MES+BSA.

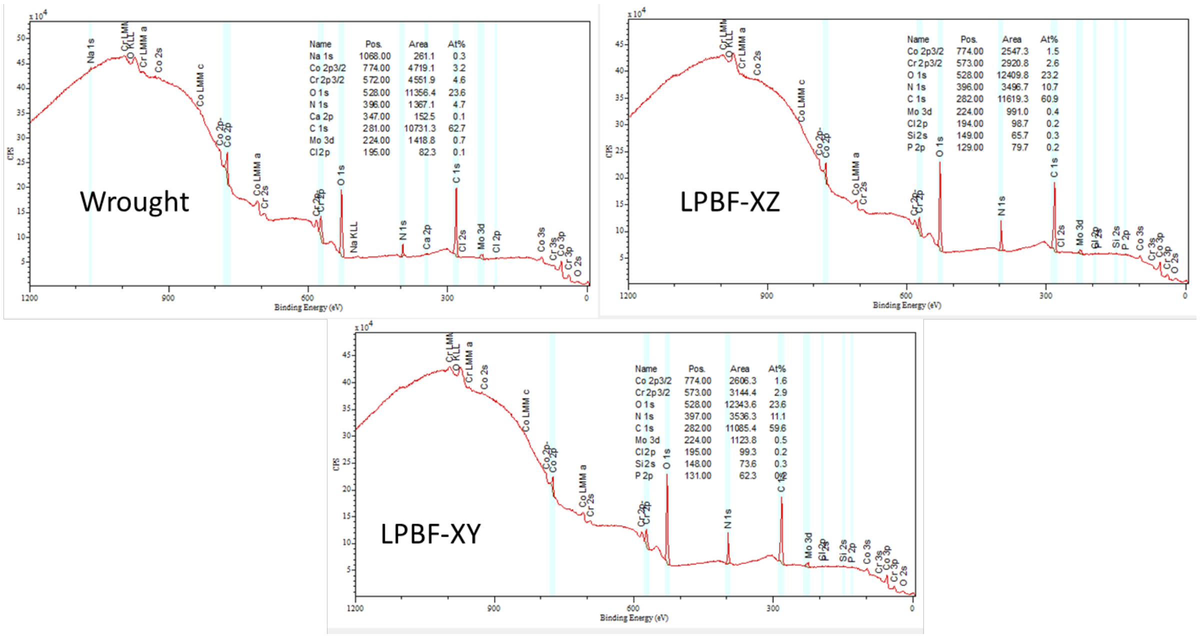

Name	Pos.	Area	At%
Na 1s	1068.00	261.1	0.3
Co 2p3/2	774.00	4719.1	3.2
Cr 2p3/2	572.00	4551.9	4.6
O 1s	528.00	11356.4	23.6
N 1s	396.00	1367.1	4.7
Ca 2p	347.00	152.5	0.1
C 1s	281.00	10731.3	62.7
Mo 3d	224.00	1418.8	0.7
Cl 2p	195.00	82.3	0.1

Name	Pos.	Area	At%
Co 2p3/2	774.00	2547.3	1.5
Cr 2p3/2	573.00	2920.8	2.6
O 1s	528.00	12409.8	23.2
N 1s	396.00	3496.7	10.7
C 1s	282.00	11619.3	60.9
Mo 3d	224.00	991.0	0.4
Cl 2p	194.00	98.7	0.2
Si 2s	149.00	65.7	0.3
P 2p	129.00	79.7	0.2

Name	Pos.	Area	At%
Co 2p3/2	774.00	2606.3	1.6
Cr 2p3/2	573.00	3144.4	2.9
O 1s	528.00	12343.6	23.6
N 1s	397.00	3536.3	11.1
C 1s	282.00	11085.4	59.6
Mo 3d	224.00	1123.8	0.5
Cl 2p	195.00	99.3	0.2
Si 2s	148.00	73.6	0.3
P 2p	131.00	62.3	0.2

Figure S27. Wide spectra of wrought, LPBF-XZ, and LPF-XY CoCrMo outside of the wear track, after tribocorrosion exposure 1 h no sliding, followed by 1 h reciprocal linear sliding at 3 N load, followed by 0.5 h no sliding, at 37 °C and at pH 7.3, in NaCl+MES+BSA+Fbn.

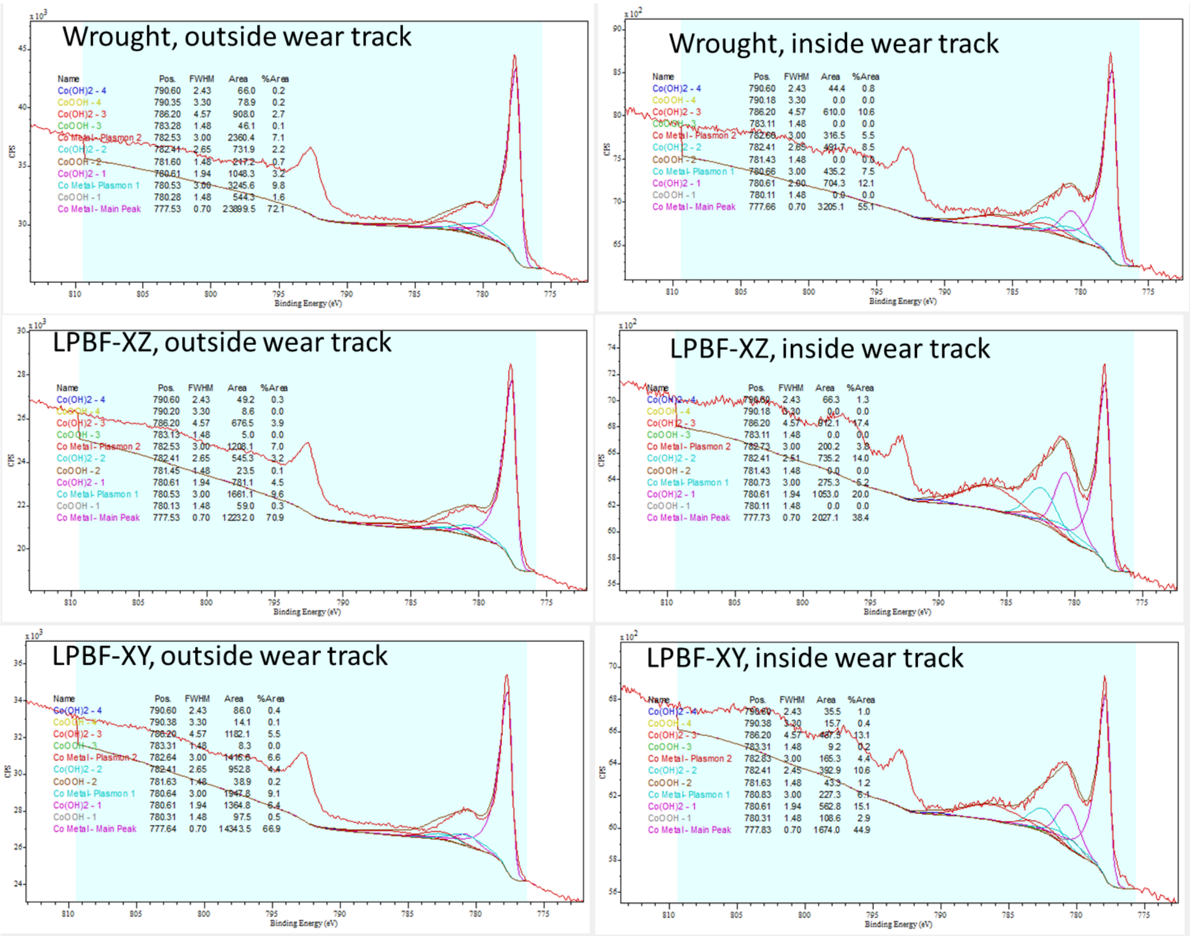

Wrought, outside wear track

Name	Pos.	FWHM	Area	%Area
Co(OH)2 - 4	790.60	2.43	66.0	0.2
CoOOH - 4	790.35	3.30	78.9	0.2
Co(OH)2 - 3	786.20	4.57	908.0	2.7
CoOOH - 3	783.28	1.48	46.1	0.1
Co Metal - Plasmon 2	782.53	3.00	2360.4	7.1
Co(OH)2 - 2	782.41	2.65	731.9	2.2
CoOOH - 2	781.60	1.48	217.2	0.7
Co(OH)2 - 1	780.61	1.94	1048.3	3.2
Co Metal - Plasmon 1	780.53	3.00	3245.6	9.8
CoOOH - 1	780.28	1.48	544.3	1.6
Co Metal - Main Peak	777.53	0.70	23899.5	72.1

Wrought, inside wear track

Name	Pos.	FWHM	Area	%Area
Co(OH)2 - 4	790.60	2.43	44.4	0.8
CoOOH - 4	790.18	3.30	0.0	0.0
Co(OH)2 - 3	786.20	4.57	610.0	10.6
CoOOH - 3	783.11	1.48	0.0	0.0
Co Metal - Plasmon 2	782.66	3.00	316.5	5.5
Co(OH)2 - 2	782.41	2.65	491.7	8.5
CoOOH - 2	781.43	1.48	0.0	0.0
Co Metal - Plasmon 1	780.66	3.00	435.2	7.5
Co(OH)2 - 1	780.61	2.00	704.3	12.1
CoOOH - 1	780.11	1.48	0.0	0.0
Co Metal - Main Peak	777.66	0.70	3205.1	55.1

LPBF-XZ, outside wear track

Name	Pos.	FWHM	Area	%Area
Co(OH)2 - 4	790.60	2.43	49.2	0.3
CoOOH - 4	790.20	3.30	8.6	0.0
Co(OH)2 - 3	786.20	4.57	676.5	3.9
CoOOH - 3	783.13	1.48	5.0	0.0
Co Metal - Plasmon 2	782.53	3.00	1208.1	7.0
Co(OH)2 - 2	782.41	2.65	545.3	3.2
CoOOH - 2	781.45	1.48	23.5	0.1
Co(OH)2 - 1	780.61	1.94	781.1	4.5
Co Metal - Plasmon 1	780.53	3.00	1661.1	9.6
CoOOH - 1	780.13	1.48	59.0	0.3
Co Metal - Main Peak	777.53	0.70	12232.0	70.9

LPBF-XZ, inside wear track

Name	Pos.	FWHM	Area	%Area
Co(OH)2 - 4	790.60	2.43	66.3	1.3
CoOOH - 4	790.18	3.30	0.0	0.0
Co(OH)2 - 3	786.20	4.57	912.1	17.4
CoOOH - 3	783.11	1.48	0.0	0.0
Co Metal - Plasmon 2	782.73	3.00	200.2	3.8
Co(OH)2 - 2	782.41	2.51	735.2	14.0
CoOOH - 2	781.43	1.48	0.0	0.0
Co Metal - Plasmon 1	780.73	3.00	275.3	5.2
Co(OH)2 - 1	780.61	1.94	1053.0	20.0
CoOOH - 1	780.11	1.48	0.0	0.0
Co Metal - Main Peak	777.73	0.70	2027.1	38.4

LPBF-XY, outside wear track

Name	Pos.	FWHM	Area	%Area
Co(OH)2 - 4	790.60	2.43	86.0	0.4
CoOOH - 4	790.38	3.30	14.1	0.1
Co(OH)2 - 3	786.20	4.57	1182.1	5.5
CoOOH - 3	783.31	1.48	8.3	0.0
Co Metal - Plasmon 2	782.64	3.00	1416.6	6.6
Co(OH)2 - 2	782.41	2.65	952.8	4.4
CoOOH - 2	781.63	1.48	38.9	0.2
Co Metal - Plasmon 1	780.64	3.00	1947.8	9.1
Co(OH)2 - 1	780.61	1.94	1364.8	6.4
CoOOH - 1	780.31	1.48	97.5	0.5
Co Metal - Main Peak	777.64	0.70	14343.5	66.9

LPBF-XY, inside wear track

Name	Pos.	FWHM	Area	%Area
Co(OH)2 - 4	790.60	2.43	35.5	1.0
CoOOH - 4	790.38	3.30	15.7	0.4
Co(OH)2 - 3	786.20	4.57	487.5	13.1
CoOOH - 3	783.31	1.48	9.2	0.2
Co Metal - Plasmon 2	782.83	3.00	165.3	4.4
Co(OH)2 - 2	782.41	2.45	392.9	10.6
CoOOH - 2	781.63	1.48	43.3	1.2
Co Metal - Plasmon 1	780.83	3.00	227.3	6.1
Co(OH)2 - 1	780.61	1.94	562.8	15.1
CoOOH - 1	780.31	1.48	108.6	2.9
Co Metal - Main Peak	777.83	0.70	1674.0	44.9

Figure S28. Co 2p high-resolution spectra of wrought, LPBF-XZ, and LPF-XY CoCrMo outside (left) and inside (right) of the wear track, after tribocorrosion exposure 1 h no sliding, followed by 1 h reciprocal linear sliding at 3 N load, followed by 0.5 h no sliding, at 37 °C and at pH 7.3, in NaCl+MES+BSA+Fbn.

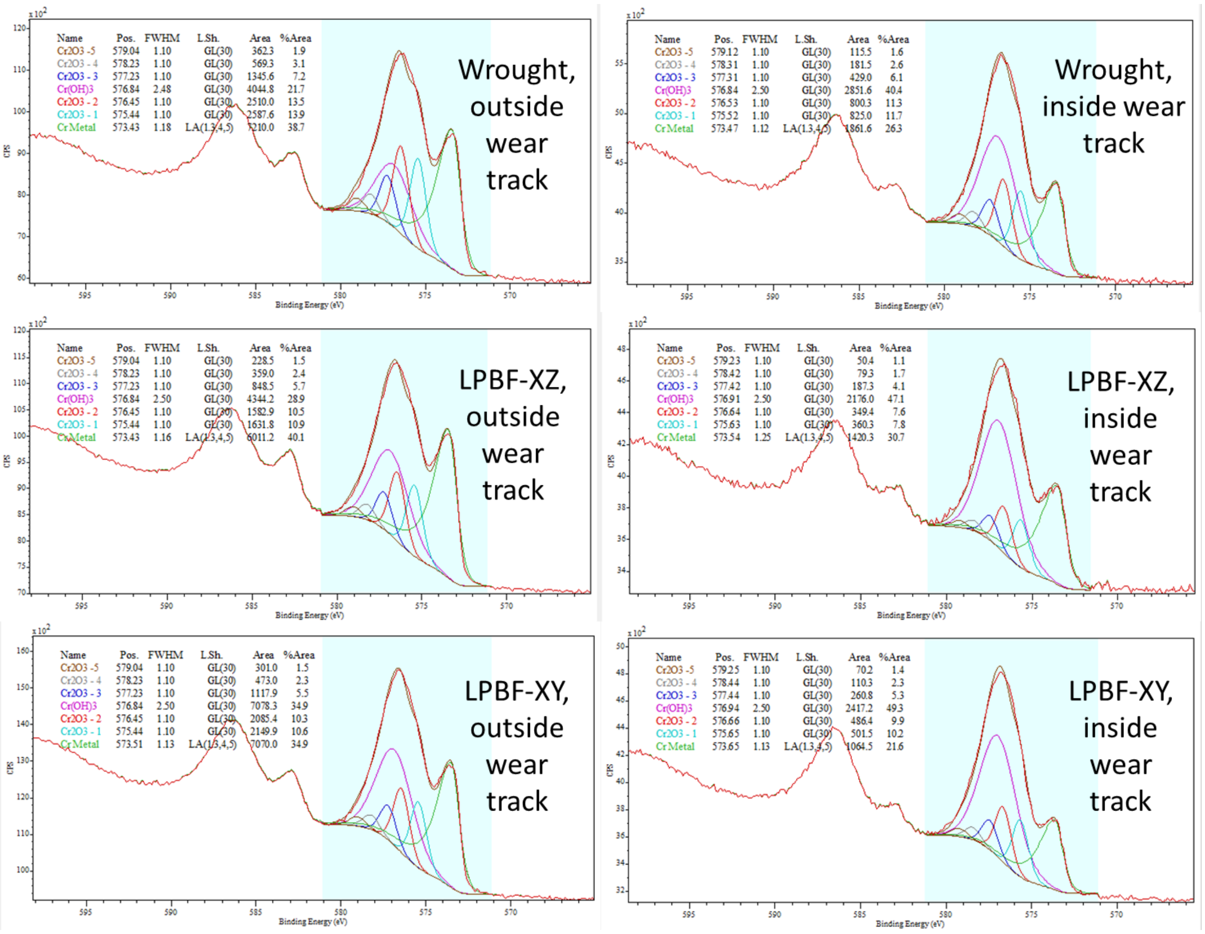

Name	Pos.	FWHM	L.Sh.	Area	%Area
Cr2O3 -5	579.04	1.10	GL(30)	362.3	1.9
Cr2O3 - 4	578.23	1.10	GL(30)	569.3	3.1
Cr2O3 - 3	577.23	1.10	GL(30)	1345.6	7.2
Cr(OH)3	576.84	2.48	GL(30)	4044.8	21.7
Cr2O3 - 2	576.45	1.10	GL(30)	2510.0	13.5
Cr2O3 - 1	575.44	1.10	GL(30)	2587.6	13.9
Cr Metal	573.43	1.18	LA(1.3,4,5)	7210.0	38.7

Name	Pos.	FWHM	L.Sh.	Area	%Area
Cr2O3 -5	579.12	1.10	GL(30)	115.5	1.6
Cr2O3 - 4	578.31	1.10	GL(30)	181.5	2.6
Cr2O3 - 3	577.31	1.10	GL(30)	429.0	6.1
Cr(OH)3	576.84	2.50	GL(30)	2851.6	40.4
Cr2O3 - 2	576.53	1.10	GL(30)	800.3	11.3
Cr2O3 - 1	575.52	1.10	GL(30)	825.0	11.7
Cr Metal	573.47	1.12	LA(1.3,4,5)	1861.6	26.3

Name	Pos.	FWHM	L.Sh.	Area	%Area
Cr2O3 -5	579.04	1.10	GL(30)	228.5	1.5
Cr2O3 - 4	578.23	1.10	GL(30)	359.0	2.4
Cr2O3 - 3	577.23	1.10	GL(30)	848.5	5.7
Cr(OH)3	576.84	2.50	GL(30)	4344.2	28.9
Cr2O3 - 2	576.45	1.10	GL(30)	1582.9	10.5
Cr2O3 - 1	575.44	1.10	GL(30)	1631.8	10.9
Cr Metal	573.43	1.16	LA(1.3,4,5)	6011.2	40.1

Name	Pos.	FWHM	L.Sh.	Area	%Area
Cr2O3 -5	579.23	1.10	GL(30)	50.4	1.1
Cr2O3 - 4	578.42	1.10	GL(30)	79.3	1.7
Cr2O3 - 3	577.42	1.10	GL(30)	187.3	4.1
Cr(OH)3	576.91	2.50	GL(30)	2176.0	47.1
Cr2O3 - 2	576.64	1.10	GL(30)	349.4	7.6
Cr2O3 - 1	575.63	1.10	GL(30)	360.3	7.8
Cr Metal	573.54	1.25	LA(1.3,4,5)	1420.3	30.7

Name	Pos.	FWHM	L.Sh.	Area	%Area
Cr2O3 -5	579.04	1.10	GL(30)	301.0	1.5
Cr2O3 - 4	578.23	1.10	GL(30)	473.0	2.3
Cr2O3 - 3	577.23	1.10	GL(30)	1117.9	5.5
Cr(OH)3	576.84	2.50	GL(30)	7078.3	34.9
Cr2O3 - 2	576.45	1.10	GL(30)	2085.4	10.3
Cr2O3 - 1	575.44	1.10	GL(30)	2149.9	10.6
Cr Metal	573.51	1.13	LA(1.3,4,5)	7070.0	34.9

Name	Pos.	FWHM	L.Sh.	Area	%Area
Cr2O3 -5	579.25	1.10	GL(30)	70.2	1.4
Cr2O3 - 4	578.44	1.10	GL(30)	110.3	2.3
Cr2O3 - 3	577.44	1.10	GL(30)	260.8	5.3
Cr(OH)3	576.94	2.50	GL(30)	2417.2	49.3
Cr2O3 - 2	576.66	1.10	GL(30)	486.4	9.9
Cr2O3 - 1	575.65	1.10	GL(30)	501.5	10.2
Cr Metal	573.65	1.13	LA(1.3,4,5)	1064.5	21.6

Figure S29. Cr 2p high-resolution spectra of wrought, LPBF-XZ, and LPF-XY CoCrMo outside (left) and inside (right) of the wear track, after tribocorrosion exposure 1 h no sliding, followed by 1 h reciprocal linear sliding at 3 N load, followed by 0.5 h no sliding, at 37 °C and at pH 7.3, in NaCl+MES+BSA+Fbn.

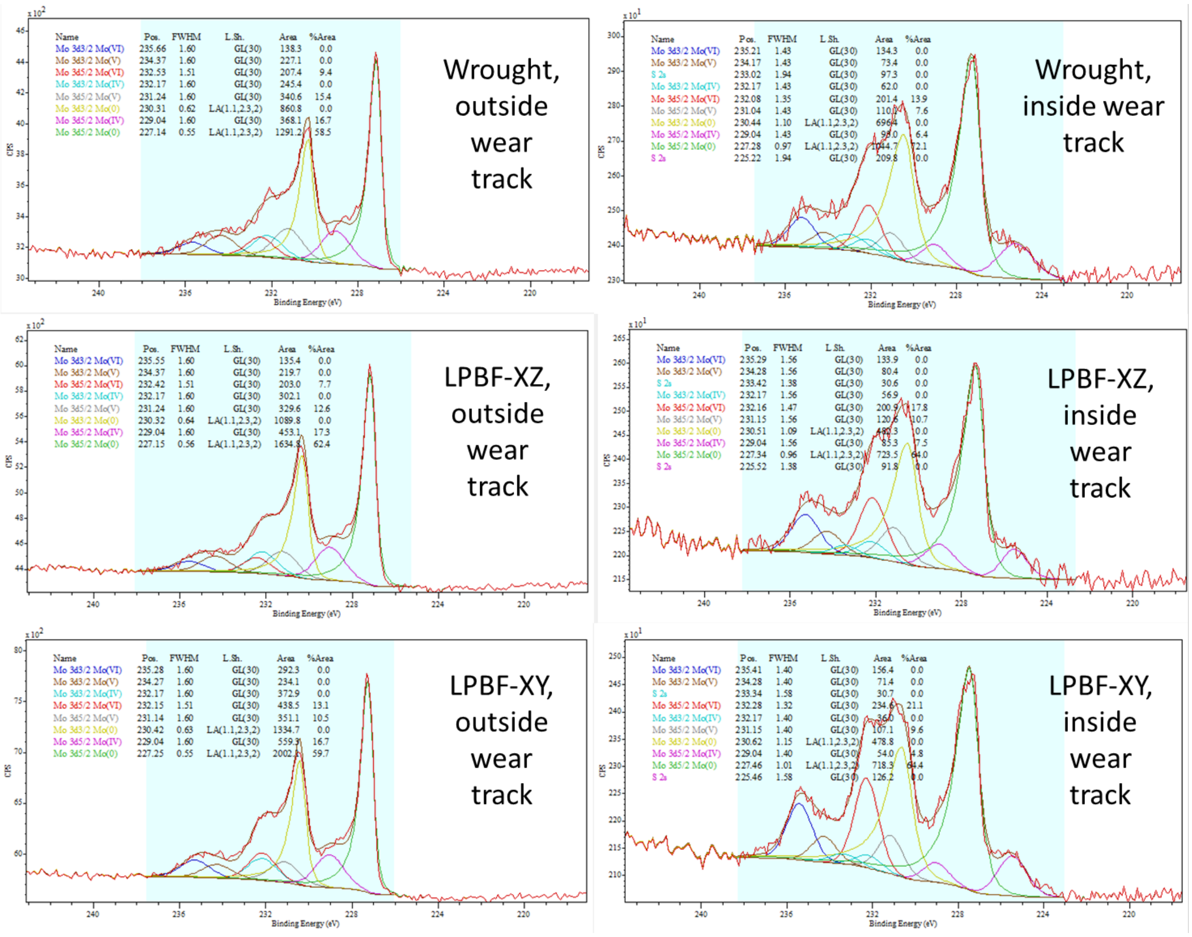

Wrought, outside wear track

Name	Pos.	FWHM	L.Sh.	Area	%Area
Mo 3d3/2 Mo(VI)	235.66	1.60	GL(30)	138.3	0.0
Mo 3d3/2 Mo(V)	234.37	1.60	GL(30)	227.1	0.0
Mo 3d5/2 Mo(VI)	232.53	1.51	GL(30)	207.4	9.4
Mo 3d3/2 Mo(IV)	232.17	1.60	GL(30)	245.4	0.0
Mo 3d5/2 Mo(V)	231.24	1.60	GL(30)	340.6	15.4
Mo 3d3/2 Mo(0)	230.31	0.62	LA(1.1,2.3,2)	860.8	0.0
Mo 3d5/2 Mo(IV)	229.04	1.60	GL(30)	368.1	16.7
Mo 3d5/2 Mo(0)	227.14	0.55	LA(1.1,2.3,2)	1291.2	58.5

Wrought, inside wear track

Name	Pos.	FWHM	L.Sh.	Area	%Area
Mo 3d3/2 Mo(VI)	235.21	1.43	GL(30)	134.3	0.0
Mo 3d3/2 Mo(V)	234.17	1.43	GL(30)	73.4	0.0
S 2s	233.02	1.94	GL(30)	97.3	0.0
Mo 3d3/2 Mo(IV)	232.17	1.43	GL(30)	62.0	0.0
Mo 3d5/2 Mo(VI)	232.08	1.35	GL(30)	201.4	13.9
Mo 3d5/2 Mo(V)	231.04	1.43	GL(30)	110.1	7.6
Mo 3d3/2 Mo(0)	230.44	1.10	LA(1.1,2.3,2)	696.4	0.0
Mo 3d5/2 Mo(IV)	229.04	1.43	GL(30)	93.0	6.4
Mo 3d5/2 Mo(0)	227.28	0.97	LA(1.1,2.3,2)	1044.7	72.1
S 2s	225.22	1.94	GL(30)	209.8	0.0

LPBF-XZ, outside wear track

Name	Pos.	FWHM	L.Sh.	Area	%Area
Mo 3d3/2 Mo(VI)	235.55	1.60	GL(30)	135.4	0.0
Mo 3d3/2 Mo(V)	234.37	1.60	GL(30)	219.7	0.0
Mo 3d5/2 Mo(VI)	232.42	1.51	GL(30)	203.0	7.7
Mo 3d3/2 Mo(IV)	232.17	1.60	GL(30)	302.1	0.0
Mo 3d5/2 Mo(V)	231.24	1.60	GL(30)	329.6	12.6
Mo 3d3/2 Mo(0)	230.32	0.64	LA(1.1,2.3,2)	1089.8	0.0
Mo 3d5/2 Mo(IV)	229.04	1.60	GL(30)	453.1	17.3
Mo 3d5/2 Mo(0)	227.15	0.56	LA(1.1,2.3,2)	1634.8	62.4

LPBF-XZ, inside wear track

Name	Pos.	FWHM	L.Sh.	Area	%Area
Mo 3d3/2 Mo(VI)	235.29	1.56	GL(30)	133.9	0.0
Mo 3d3/2 Mo(V)	234.28	1.56	GL(30)	80.4	0.0
S 2s	233.42	1.38	GL(30)	30.6	0.0
Mo 3d3/2 Mo(IV)	232.17	1.56	GL(30)	56.9	0.0
Mo 3d5/2 Mo(VI)	232.16	1.47	GL(30)	200.9	17.8
Mo 3d5/2 Mo(V)	231.15	1.56	GL(30)	120.6	10.7
Mo 3d3/2 Mo(0)	230.51	1.09	LA(1.1,2.3,2)	482.3	0.0
Mo 3d5/2 Mo(IV)	229.04	1.56	GL(30)	85.3	7.5
Mo 3d5/2 Mo(0)	227.34	0.96	LA(1.1,2.3,2)	723.5	64.0
S 2s	225.52	1.38	GL(30)	91.8	0.0

LPBF-XY, outside wear track

Name	Pos.	FWHM	L.Sh.	Area	%Area
Mo 3d3/2 Mo(VI)	235.28	1.60	GL(30)	292.3	0.0
Mo 3d3/2 Mo(V)	234.27	1.60	GL(30)	234.1	0.0
Mo 3d3/2 Mo(IV)	232.17	1.60	GL(30)	372.9	0.0
Mo 3d5/2 Mo(VI)	232.15	1.51	GL(30)	438.5	13.1
Mo 3d5/2 Mo(V)	231.14	1.60	GL(30)	351.1	10.5
Mo 3d3/2 Mo(0)	230.42	0.63	LA(1.1,2.3,2)	1334.7	0.0
Mo 3d5/2 Mo(IV)	229.04	1.60	GL(30)	559.3	16.7
Mo 3d5/2 Mo(0)	227.25	0.55	LA(1.1,2.3,2)	2002.1	59.7

LPBF-XY, inside wear track

Name	Pos.	FWHM	L.Sh.	Area	%Area
Mo 3d3/2 Mo(VI)	235.41	1.40	GL(30)	156.4	0.0
Mo 3d3/2 Mo(V)	234.28	1.40	GL(30)	71.4	0.0
S 2s	233.34	1.58	GL(30)	30.7	0.0
Mo 3d5/2 Mo(VI)	232.28	1.32	GL(30)	234.6	21.1
Mo 3d3/2 Mo(IV)	232.17	1.40	GL(30)	36.0	0.0
Mo 3d5/2 Mo(V)	231.15	1.40	GL(30)	107.1	9.6
Mo 3d3/2 Mo(0)	230.62	1.15	LA(1.1,2.3,2)	478.8	0.0
Mo 3d5/2 Mo(IV)	229.04	1.40	GL(30)	54.0	4.8
Mo 3d5/2 Mo(0)	227.46	1.01	LA(1.1,2.3,2)	718.3	64.4
S 2s	225.46	1.58	GL(30)	126.2	0.0

Figure S30. Mo 3d high-resolution spectra of wrought, LPBF-XZ, and LPF-XY CoCrMo outside (left) and inside (right) of the wear track, after tribocorrosion exposure 1 h no sliding, followed by 1 h reciprocal linear sliding at 3 N load, followed by 0.5 h no sliding, at 37 °C and at pH 7.3, in NaCl+MES+BSA+Fbn. The overlap of Mo 3d and S 2s (inside wear track only) was accounted for.

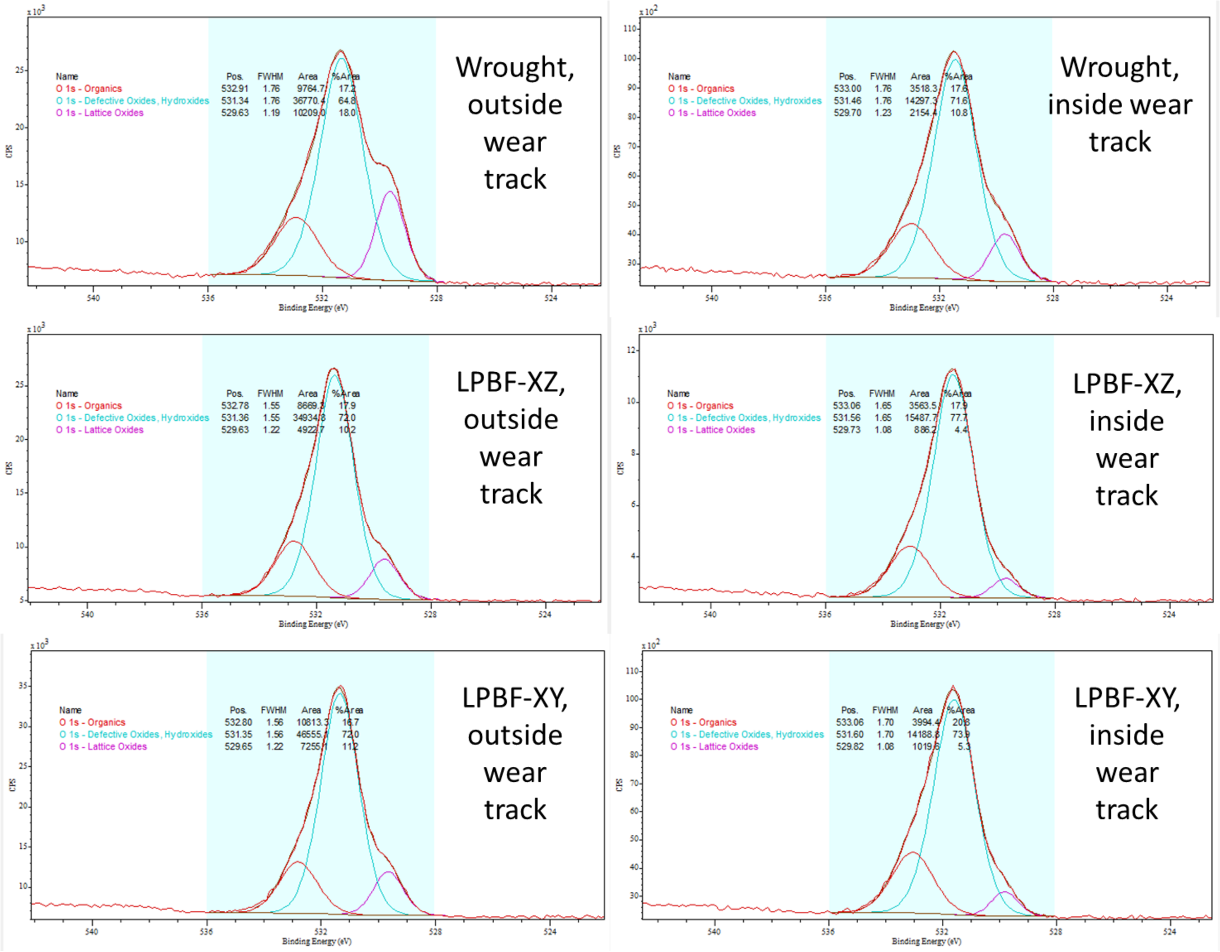

Figure S31. O 1s high-resolution spectra of wrought, LPBF-XZ, and LPF-XY CoCrMo outside (left) and inside (right) of the wear track, after tribocorrosion exposure 1 h no sliding, followed by 1 h reciprocal linear sliding at 3 N load, followed by 0.5 h no sliding, at 37 °C and at pH 7.3, in NaCl+MES+BSA+Fbn.

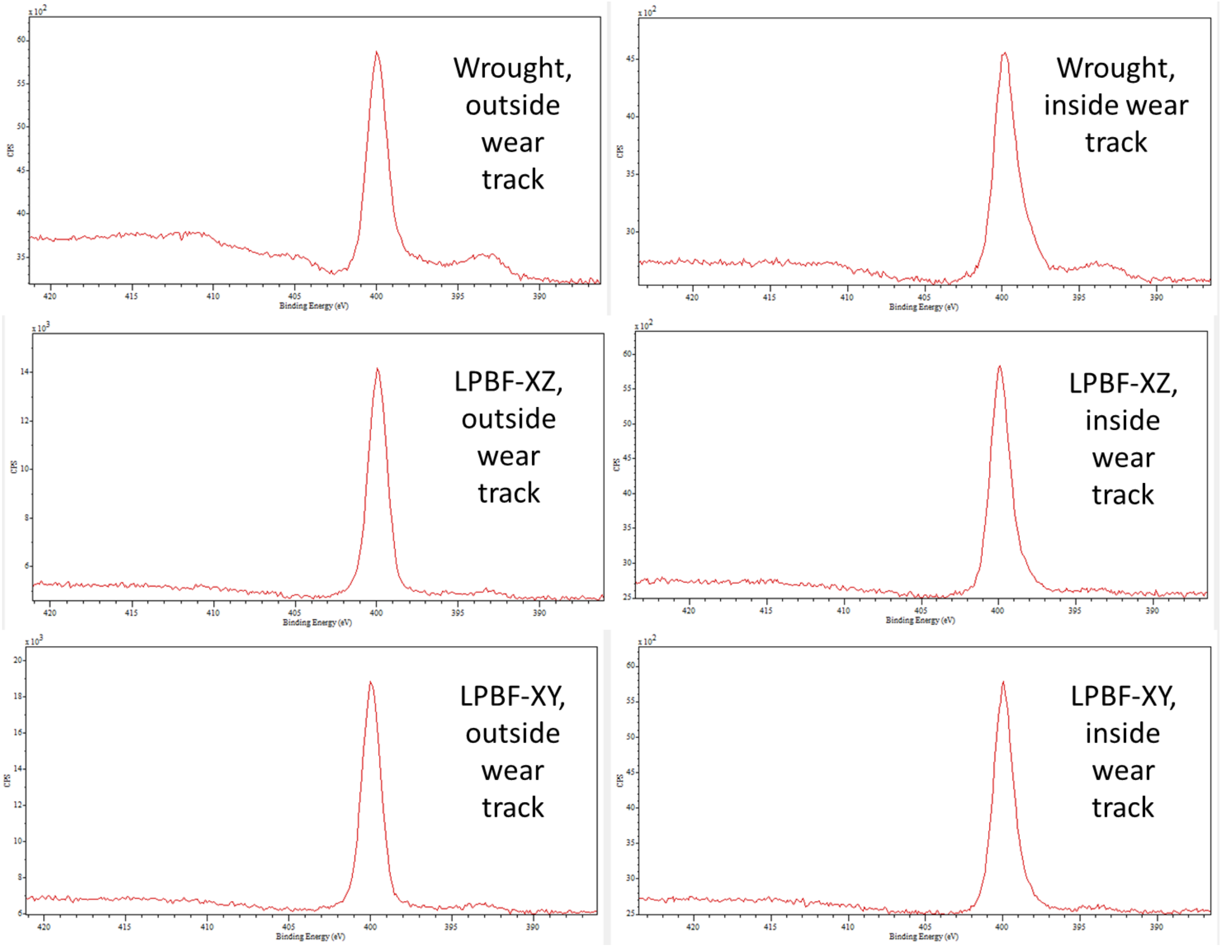

Figure S32. N 1s high-resolution spectra of wrought, LPBF-XZ, and LPF-XY CoCrMo outside (left) and inside (right) of the wear track, after tribocorrosion exposure 1 h no sliding, followed by 1 h reciprocal linear sliding at 3 N load, followed by 0.5 h no sliding, at 37 °C and at pH 7.3, in NaCl+MES+BSA+Fbn.

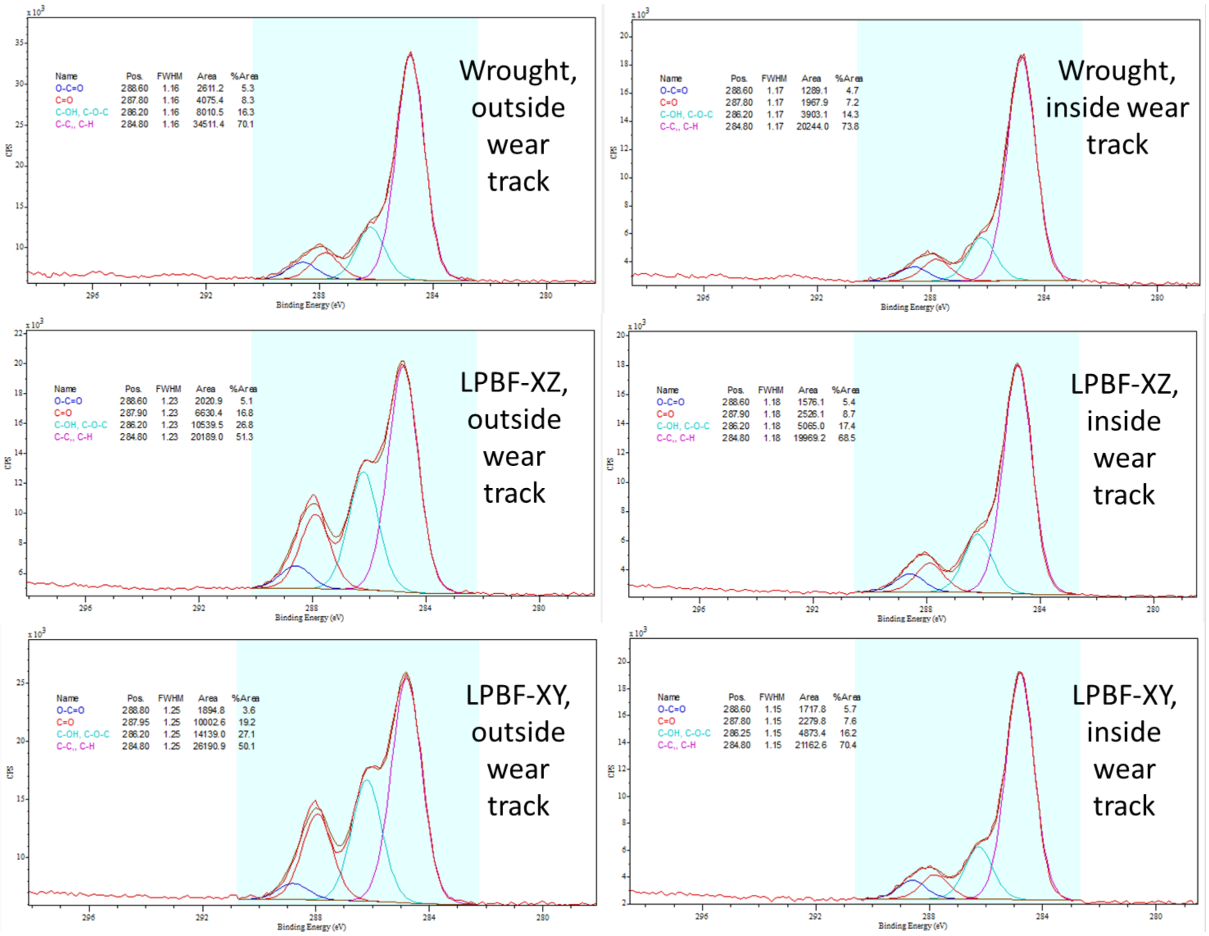

Name	Pos.	FWHM	Area	%Area
O-C=O	288.60	1.16	2611.2	5.3
C=O	287.80	1.16	4075.4	8.3
C-OH, C-O-C	286.20	1.16	8010.5	16.3
C-C,, C-H	284.80	1.16	34511.4	70.1

Name	Pos.	FWHM	Area	%Area
O-C=O	288.60	1.17	1289.1	4.7
C=O	287.80	1.17	1967.9	7.2
C-OH, C-O-C	286.20	1.17	3903.1	14.3
C-C,, C-H	284.80	1.17	20244.0	73.8

Name	Pos.	FWHM	Area	%Area
O-C=O	288.60	1.23	2020.9	5.1
C=O	287.90	1.23	6630.4	16.8
C-OH, C-O-C	286.20	1.23	10539.5	26.8
C-C,, C-H	284.80	1.23	20189.0	51.3

Name	Pos.	FWHM	Area	%Area
O-C=O	288.60	1.18	1576.1	5.4
C=O	287.90	1.18	2526.1	8.7
C-OH, C-O-C	286.20	1.18	5065.0	17.4
C-C,, C-H	284.80	1.18	19969.2	68.5

Name	Pos.	FWHM	Area	%Area
O-C=O	288.80	1.25	1894.8	3.6
C=O	287.95	1.25	10002.6	19.2
C-OH, C-O-C	286.20	1.25	14139.0	27.1
C-C,, C-H	284.80	1.25	26190.9	50.1

Name	Pos.	FWHM	Area	%Area
O-C=O	288.60	1.15	1717.8	5.7
C=O	287.80	1.15	2279.8	7.6
C-OH, C-O-C	286.25	1.15	4873.4	16.2
C-C,, C-H	284.80	1.15	21162.6	70.4

Figure S33. C 1s high-resolution spectra of wrought, LPBF-XZ, and LPF-XY CoCrMo outside (left) and inside (right) of the wear track, after tribocorrosion exposure 1 h no sliding, followed by 1 h reciprocal linear sliding at 3 N load, followed by 0.5 h no sliding, at 37 °C and at pH 7.3, in NaCl+MES+BSA+Fbn.

Supplemental References

1. de Castro Girão, D.; Béreš, M.; Jardini, A. L.; Filho, R. M.; Silva, C. C.; de Siervo, A.; Gomes de Abreu, H. F.; Araújo, W. S., An assessment of biomedical CoCrMo alloy fabricated by direct metal laser sintering technique for implant applications. *Mater. Sci. Eng. C* **2020,** *107*, 110305, 10.1016/j.msec.2019.110305.
2. Muñoz, A. I.; Mischler, S., Interactive effects of albumin and phosphate ions on the corrosion of CoCrMo implant alloy. *J. Electrochem. Soc.* **2007,** *154* (10), C562-C570,
3. Wang, Z.; Yan, Y.; Qiao, L., Effect of deformed subsurface on the corrosion resistance of biomedical CoCrMo alloy in simulated physiological solution. *J. Mater. Sci.* **2020,** *55* (27), 13351-13362, 10.1007/s10853-020-04920-z.
4. Hedberg, Y.; Karlsson, M.-E.; Wei, Z.; Žnidaršič, M.; Odnevall Wallinder, I.; Hedberg, J., Interaction of albumin and fibrinogen with stainless steel - influence of sequential exposure and protein aggregation on metal release and corrosion resistance. *Corrosion* **2017,** *73* (12), 1423-1436, 10.5006/2504.